

2020-01-01

Structure-Property-Performance Evaluation Of Refractory Metal Incorporated Gallium Oxide Thin Films For Extreme Environment Applications

Anil Krishna Battu
University of Texas at El Paso

Follow this and additional works at: https://scholarworks.utep.edu/open_etd



Part of the [Mechanical Engineering Commons](#)

Recommended Citation

Battu, Anil Krishna, "Structure-Property-Performance Evaluation Of Refractory Metal Incorporated Gallium Oxide Thin Films For Extreme Environment Applications" (2020). *Open Access Theses & Dissertations*. 2931.

https://scholarworks.utep.edu/open_etd/2931

This is brought to you for free and open access by ScholarWorks@UTEP. It has been accepted for inclusion in Open Access Theses & Dissertations by an authorized administrator of ScholarWorks@UTEP. For more information, please contact lweber@utep.edu.

STRUCTURE-PROPERTY-PERFORMANCE EVALUATION OF REFRACTORY METAL
INCORPORATED GALLIUM OXIDE THIN FILMS FOR EXTREME ENVIRONMENT
APPLICATIONS

ANIL KRISHNA BATTU

Doctoral Program in Mechanical Engineering

APPROVED:

Ramana V. Chintalapalle, Ph.D., Chair

Vinod Kumar, Ph.D.

David A. Roberson, Ph.D.

Jose F. Espiritu, Ph.D.

Stephen L. Crites, Jr., Ph.D.
Dean of the Graduate School

Copyright ©

by

Anil Krishna Battu

2020

Dedicated to my parents

STRUCTURE-PROPERTY-PERFORMANCE EVALUATION OF REFRACTORY METAL
INCORPORATED GALLIUM OXIDE THIN FILMS FOR EXTREME ENVIRONMENT
APPLICATIONS

by

ANIL KRISHNA BATTU, M.S.

DISSERTATION

Presented to the Faculty of the Graduate School of

The University of Texas at El Paso

in Partial Fulfillment

of the Requirements

for the Degree of

DOCTOR OF PHILOSOPHY

Department of Mechanical Engineering

THE UNIVERSITY OF TEXAS AT EL PASO

May 2020

Acknowledgements

I would like to thank my mentor, Dr. Ramana Chintalapalle, for his guidance, financial support, and his overall help throughout my academic years, especially during this doctoral research. He pushed me toward becoming a better scholar, researcher, and person. I am very thankful for all his lessons and support that allowed me to complete this research.

I would like to thank Dr. Vinod Kumar (Mechanical Engineering), Dr. Jose F. Espiritu (Industrial, Manufacturing and Systems Engineering), and Dr. David A. Roberson (Metallurgical, Materials and Biomedical Engineering), who agreed to be part of my doctoral committee and were willing to spend their valuable time to evaluate my dissertation research. Also, I am highly indebted to all of them for the feedback given from time to time.

I would like to thank my past and present team members at UTEP: Dr. Sandeep Manandhar, Dr. Gustavo Martinez, Mr. Swadipta Roy, Mr. Vishal Zade, Mr. Cristian Orozco, Mr. Nanthakishore Makeswaran, and all others who helped me in this endeavor and became part of a family. I would like to dedicate this to my parents, Mr. Nageswara Rao Battu and Mrs. Sridevi Battu, who always pushed me to accomplish my goals and for their continual support. I would like to thank my family, Mr. Krishna Battu, Mrs. Sai Anusha Battu, Ms. Harshini Battu, and Mr. Krishna Pratap Battu, for always supporting my goals.

I wish to express my sincere thanks to the Department of Energy (DoE) and the National Science Foundation (NSF) for financial support through research grants. Part of the research presented in this dissertation was supported by the DoE; however, the views and opinions expressed by the author(s) herein do not necessarily state or reflect those of the United States government or funding agency thereof.

Abstract

An approach is presented to design refractory-metal (RM) incorporated Ga₂O₃-based materials with controlled structural, mechanical, and optical properties. A model system based on molybdenum (Mo) doped Ga₂O₃ (GMO) has been considered to elucidate the combined effect of RM-doping and processing parameters on the properties and oxygen sensor performance of GWO nanomaterials. The molybdenum (Mo) content in Ga₂O₃ was varied from 0 to 11 at% in the sputter-deposited Ga-Mo-O films. Molybdenum was found to significantly affect the structure and optical properties. While low Mo content (≤ 4 at%) results in the formation of single-phase (β -Ga₂O₃), higher Mo content results in amorphization. Chemically induced bandgap variability ($E_g \sim 1$ eV) coupled with structure modification indicates the electronic structure changes in Ga-Mo-O. The linear relationship between chemical composition and optical properties suggests that tailoring the optical quality and performance of Ga-Mo-O films is possible by tuning the Mo content.

The present approach of Mo-doping also allows designing Ga₂O₃-based nanomaterials with tunable mechanical properties. In GMO, where Mo content (x) was varied up to ~ 11 at%, Mo-incorporation induced effects were reflected in mechanical characterization, where the hardness of the Ga-Mo-O nanocrystalline films increases for Mo ≤ 10 at%, at which point hardness decreases due to Mo-induced structural transformation. However, the elastic modulus of G-Mo-O decreases continuously with Mo incorporation. The Ga-Mo-O exhibits maximum H (~ 36 GPa) for 10 at% Mo, where Mo incorporation induces enhancement in hardness as well as in the plasticity index parameter. Based on the results, a structure-composition-mechanical property correlation in Ga-Mo-O films is established. Finally, performance evaluation made using laboratory based measurements indicate enhanced sensor performance of GMO. Incorporating Mo into Ga₂O₃ reduces response time of the oxygen sensor by several orders of magnitude.

Table of Contents

Acknowledgements.....	v
Abstract.....	vi
Table of Contents.....	vii
List of Tables.....	x
List of Figures.....	xi
Chapter 1: Motivation.....	1
Chapter 2: Introduction.....	5
2.1 Significance of the Research and Objectives.....	6
2.1.1. Fabrication of GMO Thin Films for High-Temperature Oxygen Sensors.....	8
2.1.2. Optimizing the Deposition Conditions.....	8
2.1.3. Establishing a Structure-Property Correlation.....	8
2.1.4. Evaluate GMO Based Thin Films for Oxygen Sensing at High Temperatures.....	9
Chapter 3: Literature Review.....	11
3.1. Gallium Oxide.....	11
3.2. Polymorphism.....	12
3.2.1. α -Ga ₂ O ₃	13
3.2.2. β -Ga ₂ O ₃	14
3.2.3. γ -Ga ₂ O ₃	15
3.2.4. δ -Ga ₂ O ₃	16
3.2.5. ε -Ga ₂ O ₃	17
3.3. Metal Oxide (MO) Semiconductor Properties.....	18
3.4. Metal Oxide Gas Sensors Applications.....	20
Chapter 4: Materials and Experimental Methods.....	25
4.1. Materials.....	25
4.2. Substrate Cleaning.....	26
4.3. Thin Films Synthesis - Sputtering Deposition System.....	26
4.4. Analytical Methods.....	30

4.4.1.	Grazing Incidence X-Ray Diffraction (GIXRD)	30
4.4.2.	X-ray Photoelectron Spectroscopy (XPS)	32
4.4.3.	Rutherford Backscattering Spectroscopy (RBS)	33
4.4.4.	Spectroscopic Ellipsometry	34
4.4.5.	UV-Vis Spectroscopy	35
4.4.6.	Scanning Electron Microscopy (SEM)	37
4.4.7.	Nano-Indentation Testing	38
4.4.8.	Nano-Scratch Testing.....	40
4.4.9.	Electrical Analysis	40
4.4.10.	High-Temperature Oxygen Sensor Performance.....	41
 Chapter 5: Structural and Mechanical Properties of Intrinsic Gallium Oxide - Nanocrystalline and Amorphous Gallium Oxide Thin Films		
		44
5.1.	Crystal Structure	45
5.2.	Surface Morphology	48
5.3.	Mechanical Properties.....	50
5.3.1.	Indentation Load (L) – Penetration Depth (d) Characteristics.....	50
5.3.2.	Effect of indentation Load (L) on Hardness (H) and Reduced Elastic Modulus (E_r)	52
5.3.3.	H and E_r at Critical Load	54
5.3.4.	Significance of H/E_r and H^3/E_r^2	56
5.3.5.	Strain-Rate Experiments at Specific Indentation Load.....	59
5.3.6.	Adhesion and Interfacial Bonding – Scratch Testing	61
 Chapter 6: Molybdenum Incorporated Ga_2O_3 Nanocrystalline Thin Films – Structure, Morphology and Chemical Analysis		
		64
6.1.	Structural Analysis-Crystal Structure Properties (XRD).....	64
6.2.	Morphology Analysis - Scanning Electron Microscopy (SEM).....	65
6.3.	Chemical Analysis - X-Ray Photoelectron Spectroscopy (XPS)	69
6.4.	Chemical Analysis - Rutherford Backscattering Spectrometry (RBS).....	74
 Chapter 7: Molybdenum Incorporation Ga_2O_3 Nanocrystalline Thin Films – Mechanical Properties		
		76
7.1	Nano-Mechanical Analysis - Nanoindentation.....	76
7.1.1.	Indentation Load (L) - Penetration Depth (d) Characteristics	76

7.1.2.	Effect of Indentation Load (L) on Hardness (H) and Reduced Elastic Modulus (E_r)	77
7.1.3.	H and E_r at Critical Load	79
7.1.4.	Significance of H/E_r	80
7.2.	Nano-Mechanical Analysis - Nanoscratch.....	81
Chapter 8: Molybdenum Incorporated Ga_2O_3 Nanocrystalline Thin Films – Optical Properties..		84
8.1.	Optical Analysis-Ellipsometry	84
8.2.	Optical Analysis-Spectrophotometry.....	91
Chapter 9: Molybdenum Incorporated Ga_2O_3 Nanocrystalline Thin Films – Oxygen Sensor Performance Evaluation.....		96
9.1.	Electrical Analysis - Hall Effect Measurements	96
9.2.	Gas Sensing Analysis - High-Temperature Sensor Performance	98
Chapter 10: Summary and Conclusions.....		105
Chapter 11: Future Work		107
References.....		108

Vita 119

List of Tables

Table 3.1: Summarizing the gallium-based sensors and dopants.	23
Table 4.1: List of the samples and conditions of deposition.....	29

List of Figures

Figure 1.1: The US carbon dioxide emissions from energy consumption between 1950 and 2018, by end-use sector (in million metric tons of carbon dioxide)	1
Figure 1.2: US electricity generation by major energy source, 1950-2018	2
Figure 2.1: Schematic representation of properties need to consider while designing the sensors for extreme environment conditions.	7
Figure 2.2: Schematic representation of performance evaluation of GMO thin films using various characterization techniques to understand the different properties.....	10
Figure 3.1: (Top) Dependence of crystalline phases of Ga ₂ O ₃ deposited on sapphire (0001), sapphire (1120), or Si (100) substrates with O ₂ (Ga ₂ O ₃) or H ₂ O gas. (Bottom) Summary of the synthesis and interconversion of the polymorphs of Ga ₂ O ₃ (PPT=precipitate, DEA= diethanolamine and MEA= monoethanolamine) (Recreated from ⁵⁵).....	13
Figure 3.2: Crystal structure of α-Ga ₂ O ₃	14
Figure 3.3: Crystal structure of β-Ga ₂ O ₃	15
Figure 3.4: Crystal Structure of γ- Ga ₂ O ₃ (Represented by MgAl ₂ O ₄ structure).....	16
Figure 3.5: Crystal Structure of δ- Ga ₂ O ₃ (represented by In ₂ O ₃ structure).....	17
Figure 3.6: Crystal Structure of ε-Ga ₂ O ₃ (represented by AlFeO ₃ structure ⁷¹)	18
Figure 4.1: Sputtering Targets	25
Figure 4.2: Schematic Representation of Sputtering Process	27
Figure 4.3: The schematic layout of the sputtering system employed for the fabrication of thin film depositions.....	29
Figure 4.4: Schematic representation of X-rays and Bragg’s Law	30
Figure 4.5: Bruker D8 Advance X-ray Diffractometer to characterize the Ga ₂ O ₃ and GMO films	31
Figure 4.6: Schematic representation of RBS working principle	33
Figure 4.7: Cary 5000 UV-Vis-NIR double-beam spectrophotometer.....	35
Figure 4.8: Schematic representation of UV spectrophotometry working principle	36
Figure 4.9: Hitachi S-4800 SEM	37
Figure 4.10: Hysitron 750 Nano-indentation System	38
Figure 4.11: a) Schematic illustration of indentation load-displacement data and b) Schematic illustration of the unloading process showing parameters characterizing the contact geometry..	39
Figure 4.12: Schematic representation of the oxygen sensor setup	43
Figure 4.13: Schematic representation a) sample mounting b) sensor sample	43
Figure 5.1: X-ray diffraction patterns of Ga ₂ O ₃ films	47
Figure 5.2: SEM images of Ga ₂ O ₃ thin films as a function of T _s	49
Figure 5.3: (a) Effect of indentation load on the Ga ₂ O ₃ films in terms of indentation depth (b) Load-displacement curves of Ga ₂ O ₃ films obtained at 2000 μN indentation load.	52
Figure 5.4: (a) Effect of indentation load on H; (b) Effect of indentation load on E _r	54
Figure 5.5: Hardness and elastic modulus of Ga ₂ O ₃ films.....	56
Figure 5.6: The effect of T _s on: (a) H/E _r and (b) H ³ /Er ² values. (c) Linear relationship between H ³ /Er ² and H as noted in Ga ₂ O ₃ films.....	59
Figure 5.7: Variation of hardness with equivalent strain rates at a constant load of 350 μN.....	61
Figure 5.8: Scratch testing profiles of Ga ₂ O ₃ thin films. Depth profiles for Ga ₂ O ₃ thin films deposited at various T _s are shown.....	62
Figure 5.9: Scratch testing data of Ga ₂ O ₃ films. Surface images after scratch test are shown.	63

Figure 6.1: GIXRD patterns of GMO samples. The structural evolution as a function of Mo content is evident.	65
Figure 6.2: SEM images of GMO films. The effect of Mo on the morphology evolution of GMO films is evident.	67
Figure 6.3: SEM cross-section data of GMO films.	68
Figure 6.4: XPS survey scan for GMO films.	70
Figure 6.5: High-resolution XPS data of Ga, O, and Mo core level peaks in GMO films deposited at variable Mo concentration. a) Ga 3d high-resolution XPS spectra. b) O 1s high-resolution XPS spectra. c) Mo 3d core-level XPS spectra.	73
Figure 6.6: concentration of Mo as a function of Mo target sputtering power.	74
Figure 6.7: RBS data for GMO films, deposited under variable Mo concentration (experimental curves (circles) and SIMRA simulated curves (lines)).	75
Figure 7.1: Effect of indentation load on the GMO films in terms of indentation depth.	77
Figure 7.2: (a) Effect of indentation load on H; (b) Effect of indentation load on E_r	78
Figure 7.3: Hardness and reduced elastic modulus of GMO films.	80
Figure 7.4: Effect of Mo-target sputtering power on H/E_r and H^3/E_r^2 values.	81
Figure 7.5: Scratch test performance on Ga-Mo films.	83
Figure 7.6: Scratch testing profiles of GMO thin films. Depth profiles for GMO thin films deposited at various Mo at% are shown.	83
Figure 8.1: Spectral dependence of Ψ and Δ for GMO films. The experimental and modelling curves are shown.	85
Figure 8.2: a) Refractive index (n) and b) Extinction Coefficient (k) dispersion profiles of GMO samples.	87
Figure 8.3: Thickness of Mo doped Ga_2O_3 thin films at a different sputtering power.	88
Figure 8.4: Variation of 'n' values of GMO samples at different two wavelengths.	89
Figure 8.5: Relative density.	90
Figure 8.6: Spectral transmission characteristics of GMO films. The Mo-induced shift is evident from the inset, where the expanded region of the absorption region is shown.	92
Figure 8.7: $(\alpha h\nu)^2$ vs. $h\nu$ plots of GMO. The linear region is extrapolated to zero absorption to obtain the E_g value. The absorption edge shift towards lower energy is evident.	93
Figure 8.8: Variation in bandgap as a function of Mo sputtering power. A significant reduction in E_g with Mo is evident.	95
Figure 9.1: Electrical characteristics of GMO films at various Mo concentration.	97
Figure 9.2: Electrical data of GMO films. Arrhenius plots are shown for samples with variable Mo content.	99
Figure 9.3: Activation energy of GMO films. The continuous decrease in EA values with Mo incorporation into Ga_2O_3 can be noted.	100
Figure 9.4: Gas sensing performance test for GMO films.	102
Figure 9.5: Oxygen sensor performance of characteristic values of GMO films. (a) m value (b) Response time determined from functional electrical characteristics of GMO.	104

Chapter 1: Motivation

Energy is one of the most important and basic requirements for comfortable living. Figure 1.1 represents the US carbon dioxide emissions, by sector, from 1950 to 2018. In the year 2018, about 1.9 billion metric tons of CO₂ emissions were generated from energy consumption in the US transportation sector. In the 20th century, there was a rapid growth in population and energy utilization, which was the main source to generate this 1.9 billion metric tons¹⁻⁵. This phenomenon is continuing to now (21st century); as a result, industrial growth was increased to satisfy the needs, especially in the electric power and transportation sectors.

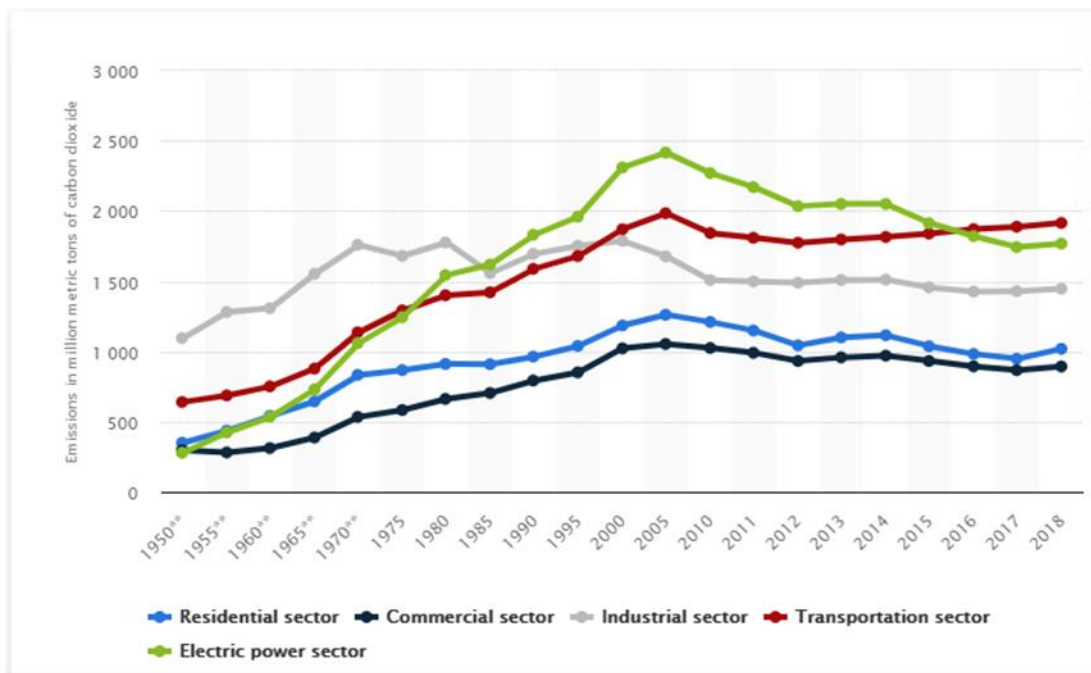


Figure 1.1: The US carbon dioxide emissions from energy consumption between 1950 and 2018, by end-use sector (in million metric tons of carbon dioxide)

This energy demand is supplied primarily by thermal power plants, which produce about 85% of the energy in the US⁶. Figure 1.2 represents the electricity generation using various sources. Thermal power plants use coal and other fossil fuels, including petroleum-based solid fuels, and liquid fuels such as gasoline and natural gas. As a result, hazardous substances (arsenic, selenium,

mercury and lead), greenhouse gases (CO₂ and CH₄), and toxic gases (CO and NO_x) are generated. In other words, industrialization is the main reason for the increase in environmental pollution. In most developed or developing countries, the pollution level exceeded due to the effect of industrialization, and air and/or water pollution is taking a heavy toll on lives. Therefore, there is a need for research in monitoring air pollution. Interest in monitoring the gases and determining their composition has increased continuously in the last decade or so. In this context, monitoring refers to the determination of the presence of gases in the air that may pollute the air. Among the various monitoring techniques, gas detection sensors place a major role.

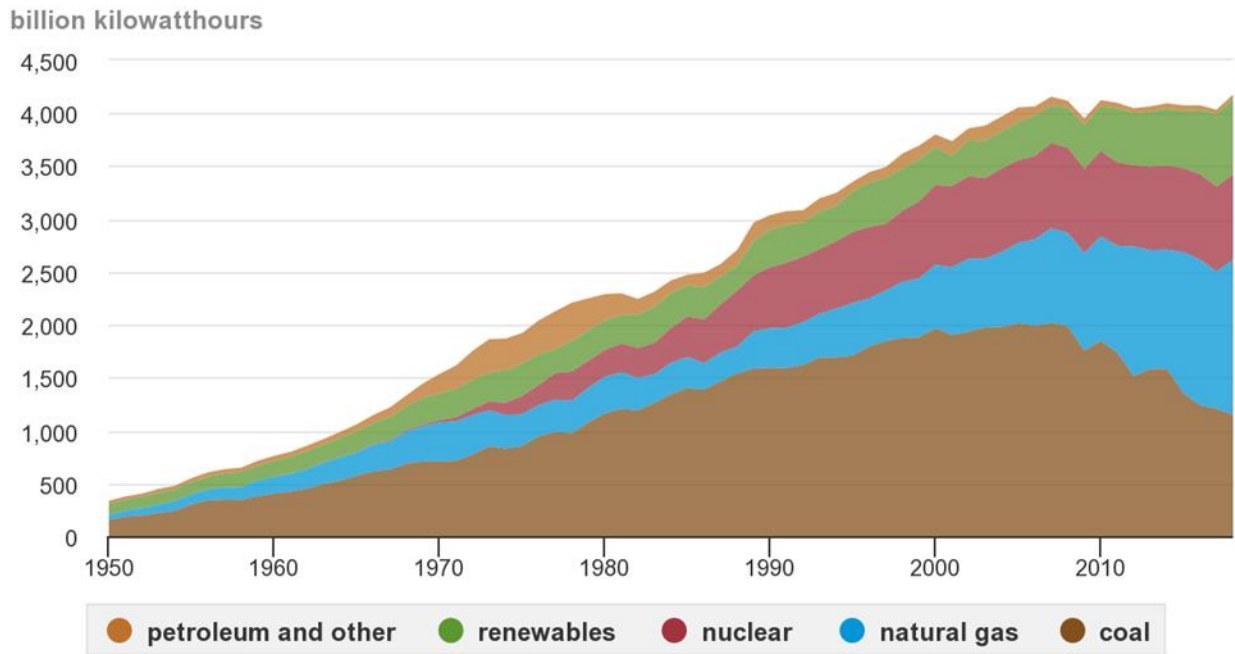


Figure 1.2: US electricity generation by major energy source, 1950-2018

The system-based gas sensors play a vital role in energy efficiency and emission control in industrial and combustion process. There is a continuous need for developing fast, reliable, and at the same time low-cost sensors which can perform well even in the extreme and harsh environments where high temperature and pressure act, such as automotive, aerospace, power plants, etc. As per the study conducted by US DOE, sensors are predicted to save 0.25 quadrillion

BTU per year of energy across all the energy-consuming industries⁶. In the current world, most engines will rely on a different type of sensors to regulate and perform monitoring purposes, such as of emissions, engine performance, and other important functions.

Therefore, sensors must give accurate results to reduce the emissions and at the same time to increase the performance; oxygen sensors are one of them. Despite large industries, measuring the small gas concentrations became highly important, such as measuring unburnt and CO emissions from the vehicle exhaust. To detect in such situations, metal oxide semiconductor gas sensors are one of the most widely used sensors. Emissions-monitoring sensors for these applications include oxygen (O_2)^{3, 7}, nitrogen dioxide (NO_2)⁵, nitrous oxide (NO)⁸, carbon monoxide (CO)⁹, hydrocarbons (HCs)¹⁰, carbon dioxide (CO_2)¹¹ and volatile organic compounds (VOCs).

From the considerations mentioned above, there is enormous interest in research, development and optimization of the combustion processes for energy harvesting. Also, it is clear that, by improving the coal-based firing/combustion processes in the power plants, savings expected are enormous. However, in order for this savings and efficiency improvements to happen, sensors and controls capable of withstanding extreme environments such as high temperatures, highly corrosive atmospheres, and high pressures needed. Controlled combustion can eliminate, in addition to generating economic gains and prosperity, the pollutant emissions that are critically affecting our environment, health and energy resources. Optimization of the combustion processes in power generation systems can be achieved by sensing, monitoring and control of oxygen, which is a measure of the completeness of the process, and can lead to enhanced efficiency and reduced greenhouse gas emissions. However, despite the fact that there exists a very high demand for advanced oxygen sensors for combustion monitoring and control in power generation systems and

automobiles, the existing technologies suffer from poor ‘response and recovery times’ and ‘long-term stability.’

Inspired by aforementioned challenges, it is proposed to undertake a detailed study where the central theme of the proposed research is to gain an insightful understanding of the structure-property-processing relationship, which can help in understanding the role of refractory metal dopants on micro- and nanostructure, which can help establish strategies to optimize the sensor performance of Ga_2O_3 . While the science, engineering and technological importance of Ga_2O_3 -based materials for sensors are discussed in the subsequent chapters, the specific objectives of the research work are the following:

- (1) Understand the effect of molybdenum incorporation coupled with advantages of “nanoscale” to enhance surface area and reactivity, shorter diffusion paths, and rapid grain boundary diffusion that are unique to the sensors, to enhance the sensitivity with a much faster response time.
- (2) Quantify the micro- or ultra-microstructure.
- (3) Establish the structure-property relationship and conditions to enhance the sensor performance.
- (4) Establish strategies to enhance the oxygen sensor performance of Mo-doped Ga_2O_3 materials.
- (5) Understand the role of dopants (such as Mo in this case) to enhance the rapid response time while still elevating the extreme environment functionality of Ga_2O_3 materials.

Chapter 2: Introduction

Metal oxide semiconductor gas sensors are becoming most promising and widely used in today's real-time applications^{2, 4, 12-14}. Thin-film based metal oxide sensors are playing a crucial role in gas sensing applications because of their low power consumption, small dimensions, and high efficiency^{12, 15-16}. These sensors provide high compatibility, on-line operation with ease of integration into nanotechnology, microelectronic processing, and portable device technology. Metal oxides such as ZrO_2 , SnO_2 , TiO_2 ,¹⁷⁻¹⁸ WO_3 , MoO_3 ,¹⁹⁻²⁰ Fe_2O_3 ²¹⁻²² and many others have been studied well for sensing, and due to their high mobility and transparency these are well suited for photocatalyst and photovoltaic applications^{1, 23-25}. In general, all these metal oxide gas sensors will operate at high temperatures, which is more than 150 °C. At these temperatures, the materials' characterizations will change, which results in changes to the electronic structure. As a result, their electron mobility and resistivity properties will change. Therefore, the choice of material used for sensing is very important, especially to detect oxygen. For example, at higher temperatures, oxygen will induce different electrical responses, because gas sensors require highly stable electrical properties.

The very first commercial lambda probes were based on a potentiometric cell of ZrO_2 , which generates a voltage output to O_2 partial pressure (exhaust gases and atmospheric gases). On the other hand, the lack of oxygen sensitivity reaction is one of the major limitations of ZrO_2 sensors. This is due to the ZrO_2 alloys preoccupy with O_2 , and as a result deliver much lower sensitivity than original output. To avoid this drawback, ZrO_2 sensors always have to be preheated to 650 °C²⁶. In addition to this drawback for O_2 , these ZrO_2 sensors are not well suitable to other gases such as carbon monoxide, hydrogen, and other hydrocarbons. Furthermore, commonly used

sensors have disadvantages such as slow response time, morphological disorders, long-term instability and poisoning by the chemical substances that need to be detected.

Gallium Oxide (Ga_2O_3) is recognized as one of the predominant metal oxide for design and development of gas sensors because of its exceptional thermal and chemical stability and also because of its excellent electronic properties. In this dissertation, we report on the effect of refractory metal, Molybdenum (Mo) incorporation on the structure, and optical and electrical properties of Ga_2O_3 , where the results demonstrate that the tailor-made materials with tunable properties for high-temperature sensors and photo-catalytic applications are readily possible.

2.1 Significance of the Research and Objectives

Using advanced sensors can provide the energy and aerospace industries with increased operational efficiency, reduced emissions, and lower operating costs. In addition, scientific and research advancements in rapid, robust sensors and controls can accelerate the time to full-scale commercialization and implementation of next-generation, zero-carbon power generation technologies. In this context, currently, there is enormous recent interest in research, development and optimization of the combustion processes for efficient energy harvesting and emission control. Monitoring of oxygen content is the primary method of optimization of the combustion process, which requires rapidly responding reliable sensors near the combustion zone. However, the extreme harsh conditions, importantly high temperatures (600-1200 °C), elevated pressures (~500 psi), corrosive environments coupled with mechanical extremes, prevalent in the power generation systems create barriers and challenges to design such oxygen sensors and combustion monitoring and control.

Sensors based on metal oxide semiconductors (MOS) are most promising for power generation systems due to their small dimensions, low cost, low power consumption, on-line

operation, high compatibility with microelectronic processing, and ease of integration into nanotechnology and portable device technology. Therefore, in recent years, extensive studies have been directed towards the fundamental understanding, research, and development of oxygen sensors based on metal oxides. However, despite the fact that there exists a very high demand for advanced oxygen sensors for combustion, the existing technologies suffer from poor response and recovery times and long-term stability. The Figure 2.1. shows the schematic representation of properties need to consider in designing the most effective sensor for extreme environment conditions.

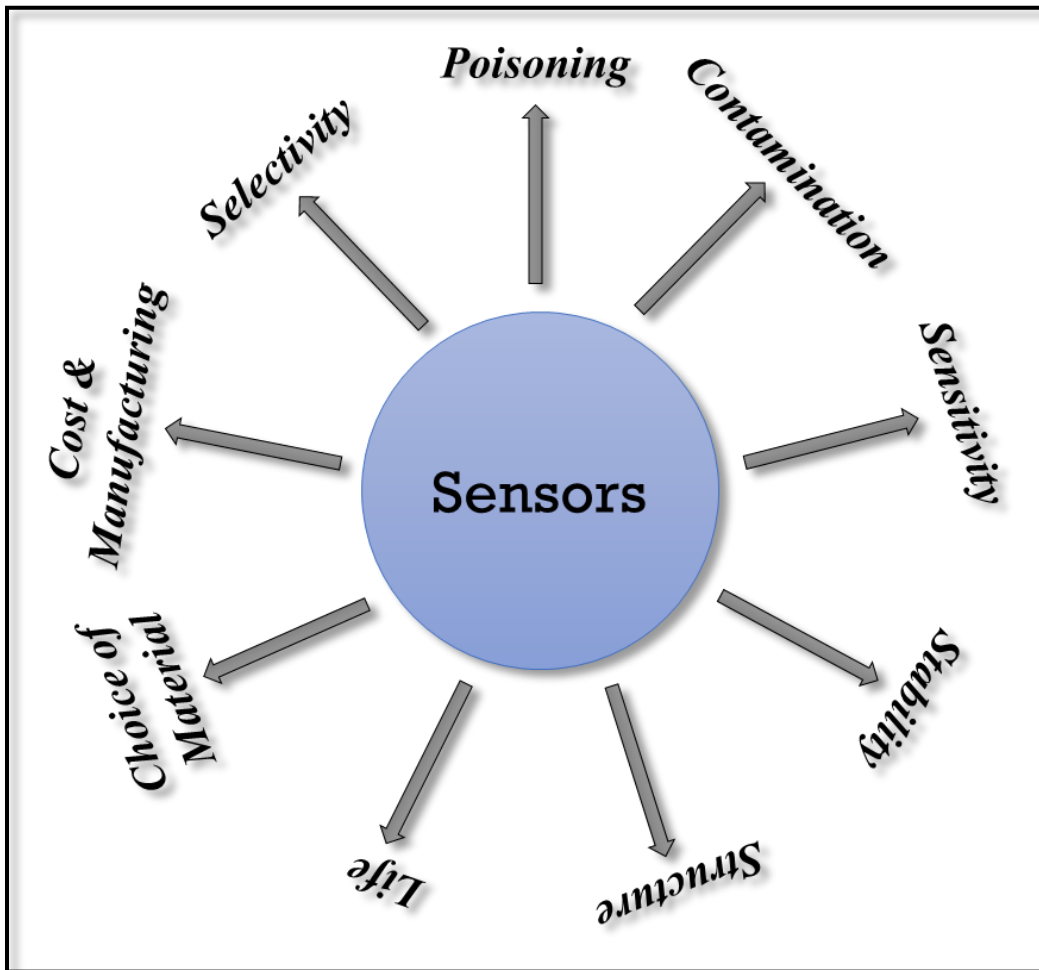


Figure 2.1: Schematic representation of properties need to consider while designing the sensors for extreme environment conditions.

The recent approaches to improve the response time, selectivity and prevent sulfur poisoning have not met with the desired success. Further research and development is needed to realize oxygen sensors that combine rapid response time, selectivity and long-term stability. The most important reason for the technological barriers in designing such oxygen sensors for power generation systems is the lack of control over structure of the sensor materials, particularly over the random polycrystalline nature at the extreme environments. Furthermore, a method to select a specific material to detect certain chemicals has not been identified yet; the selections are made on the basis of experimental data without aid of a general model. In this context, we propose to investigate the Mo-doped Ga_2O_3 nanomaterials to design oxygen sensors that combine a rapid response, reliability, and robustness at extreme environments.

The following are specific research tasks and objectives.

2.1.1. Fabrication of GMO Thin Films for High-Temperature Oxygen Sensors.

The first objective is to fabricate high-quality GMO thin films by RF magnetron sputtering. The goal is to improve the sensor response.

2.1.2. Optimizing the Deposition Conditions

Deposition conditions are tuned to achieve the best structural, morphological and electrical conditions to improve sensor performance. The effect of processing conditions such as sputtering pressure, surface temperature and partial pressure of reactive gases on the crystal structure, grain size, bandgap, resistivity, and other related parameters will be studied in detail. The aim is to optimize the conditions to fabricate thin films to achieve high structural quality.

2.1.3. Establishing a Structure-Property Correlation

In order to gain a deeper understanding of structure and property relationship for GMO thin films for sensor applications, a structure-property correlation will be established. This will

have a focus on the response time, determined by the chemical reaction kinetics between the material surface and the oxygen molecules and, consequently, by the diffusion process and surface reactions. For that reason, an understanding of the deficient chemistry of doped Ga-oxide is required.

2.1.4. Evaluate GMO Based Thin Films for Oxygen Sensing at High Temperatures

Evaluating the sensor performance is crucial for utilization in sensor technology. Intrinsic Ga₂O₃ based films will be exposed to test gas(es) under a temperature of 500 °C for oxygen detection. The samples will be introduced into a vacuum chamber and their variation in electrical conductivity under the presence of oxygen will be calculated. Sensitivity, time response, and selectivity will be determined. Furthermore, the GMO-based sensors' detection range was evaluated, by varying the partial pressure of oxygen introduced, in order to see the range of detection at the already mentioned temperatures.

Summarizing the above-mentioned considerations, when the materials size reduced to nanometer range, the material exhibits peculiar and interesting properties either physically and/or chemically and/or electrically etc. Therefore, need to perform various characterization techniques to better understand these properties. Hence, interconnecting each property along with gas sensing properties. This comparison gives us to design a performance-based components for various applications, such as can be design a component with mechanical reliability as well as for electronic device performance.

Structural Analysis

X-Ray Diffraction (XRD)

Morphological Analysis

Scanning Electron Microscopy (SEM)

Chemical Analysis

X-ray Photoelectron Spectroscopy (XPS)

Rutherford Backscattering Spectroscopy (RBS)

Optical Analysis

UV-Vis Spectroscopy

Ellipsometry

Nano-Mechanical Analysis

Nano-Indentation

Nano-Scratch

Electrical Analysis

Hall Effect Measurement



Gas Sensing

Figure 2.2: Schematic representation of performance evaluation of GMO thin films using various characterization techniques to understand the different properties

Chapter 3: Literature Review

There are some wide bandgap semiconductor materials and systems, including the high Al-content AlGaN alloys, SiC, BN, ZnSe, diamond, and ZnMgO, which are potentially suitable for electronic device applications. However, many of these materials come with certain limitations. To indicate in brief, these limitations are the persistent photoconductivity in AlGaN, the indirect gap of SiC, the environmental sensitivity and cost of ZnO, lack of high-quality films/substrates, availability, and lack of controlled doping technology for some other materials²⁷. Therefore, due to these constraints, the research and development activities were focused towards Ga₂O₃ expecting that it can overcome many of those limitations in device technology development.

3.1. Gallium Oxide

Gallium oxide (Ga₂O₃) has been receiving considerable attention from the scientific and research community in recent years²⁸⁻²⁹. Ga₂O₃ finds a wide range of technological applications, which include transparent electrode material in electronics and photonics³⁰⁻³¹, high-temperature chemical sensing³²⁻³³, deep ultraviolet (UV) photodetection³⁴⁻³⁵, and spintronics³⁶⁻³⁷. Excellent, deep transparency in the UV region of the electromagnetic spectrum coupled with a wide bandgap (~5 eV)³⁸⁻³⁹ makes it a perfect candidate for a transparent electrode in UV-based photovoltaics⁴⁰, optoelectronics³⁹⁻⁴³, and luminescence displays⁴². Additionally, Ga₂O₃ materials are attractive for the design and development of high-power Schottky diodes and high-voltage field-effect transistors^{30, 44}.

On the other hand, exploring the electrical characteristics and utilization of the wide bandgap semiconductor properties of Ga₂O₃ is still in early stages³⁰. In this regard, Yao et al. reported that the formation of ohmic contacts to Ga₂O₃ is not determined by any one dominant factor, such as metal work function, and that limited interfacial reactions play an important role in

both the morphology and electrical behavior³⁰. It has been argued that further work is needed to utilize the electronic properties of Ga₂O₃ in advanced device application⁴⁵. Also, while evolving new functionalities and emerging applications involving Ga₂O₃ nanomaterials or hybrid structures are promising, surface/interface chemistry and control over the phase and composition is the key to tailoring the materials' performance to meet the requirements of a given application or to search for new technological applications. Especially for optoelectronics, sensors and photovoltaic applications, understanding the interplay between nano/micro-structure, composition and optical/electronic properties are quite important⁴⁶⁻⁴⁹.

3.2. Polymorphism

Intrinsic Ga₂O₃ exhibits polymorphism; it can crystalize in five different crystal structures, namely α , β , γ , δ , and ϵ phases⁵⁰⁻⁵⁴. Pearton et al. reported different crystalline phases of Ga₂O₃ thin films fabricated on sapphire and Si (100) substrates in the presence of O₂ and H₂O⁵⁵. The stable polymorphism depends on the choice of the substrates and oxygen source gases, which consists of different space groups with a different coordination number of Ga ions.

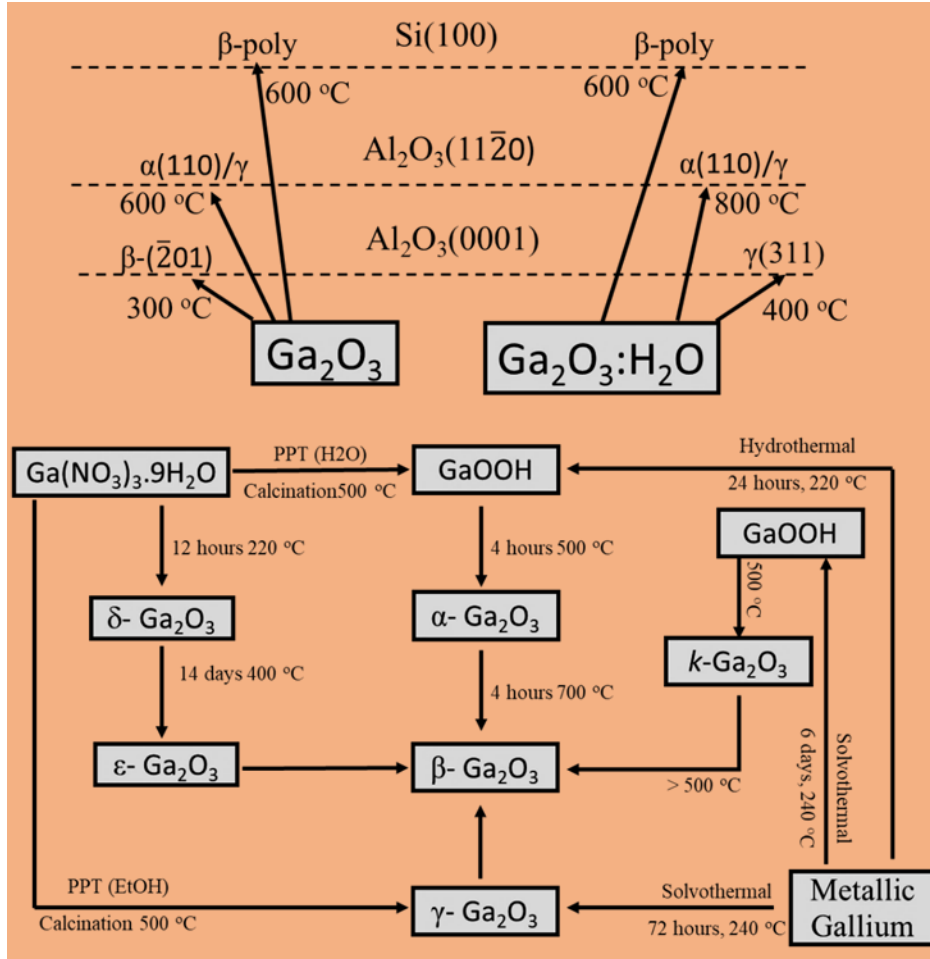


Figure 3.1: (Top) Dependence of crystalline phases of Ga₂O₃ deposited on sapphire (0001), sapphire (11 $\bar{2}$ 0), or Si (100) substrates with O₂ (Ga₂O₃) or H₂O gas. (Bottom) Summary of the synthesis and interconversion of the polymorphs of Ga₂O₃ (PPT=precipitate, DEA= diethanolamine and MEA= monoethanolamine) (Recreated from⁵⁵)

3.2.1. α -Ga₂O₃

α -Ga₂O₃ is the first polymorph and has a rhombohedral structure (analogous to corundum), as shown in Figure 3.2. The space group is $R\bar{3}c$, and it has the same crystal structure as Al₂O₃⁵⁶. The distance between Ga³⁺ ions is considerably shorter in the corundum structure in comparison with monoclinic β -phase. The oxygen ions are hexagonal close-packed and gallium ions occupy two-thirds of the octahedral sites. Marezio et al. experimentally calculated the lattice parameters to be $a=4.9825$ Å and $c=13.433$ Å⁵⁷. Yoshioka et al. reported the calculated lattice parameters are

$a=5.059 \text{ \AA}$ and $c=13.618 \text{ \AA}$ ⁵⁸. Stepanov et al. reported that $\alpha\text{-Ga}_2\text{O}_3$ can be synthesized by heating $\text{GaO}(\text{OH})$ in the air between $450 \text{ }^\circ\text{C}$ and $550 \text{ }^\circ\text{C}$ ⁵⁹. $\alpha\text{-Ga}_2\text{O}_3$ will be a metastable phase at ambient conditions, with 110 meV binding energy and a direct bandgap of 5.61 to 6.44 eV , which is the highest for that of all the polymorphs. Due to the large bandgap, the $\alpha\text{-Ga}_2\text{O}_3$ films are attractive for photocatalytic applications⁶⁰. On the other hand, these values were in good agreement with the theory proposed by Becke. Stepanov et al. and He et al. reported a refractive index for $\alpha\text{-Ga}_2\text{O}_3$ of 1.74 to 1.95 and that it has an optical dielectric constant of 3.03 to 3.80 ^{59, 61}.

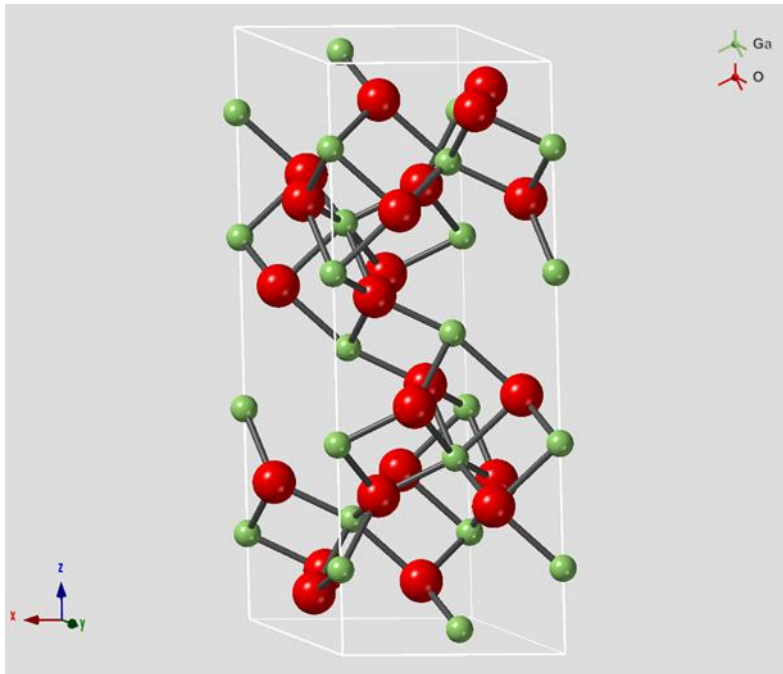


Figure 3.2: Crystal structure of $\alpha\text{-Ga}_2\text{O}_3$

3.2.2. $\beta\text{-Ga}_2\text{O}_3$

Among all the Ga_2O_3 polymorphs, $\beta\text{-Ga}_2\text{O}_3$ is a thermodynamically favorable and well-studied polymorph. $\beta\text{-Ga}_2\text{O}_3$ has a monoclinic structure (represented in Figure 3.3) and belongs to the $C2/m$ space group. $\beta\text{-Ga}_2\text{O}_3$ is the most stable with a melting point of $\sim 1900 \text{ }^\circ\text{C}$, bandgap of $\sim 5 \text{ eV}$, and high breakdown field of 8 MV cm^{-1} ⁶². Kohn et al., He et al., and Ahman et al. reported the lattice parameters of $\beta\text{-Ga}_2\text{O}_3$ are as follows: $a=12.214 - 12.27 \text{ \AA}$, $b=3.0371 - 3.04 \text{ \AA}$,

$c=5.7981 - 5.80 \text{ \AA}$, and $\beta=103.7^\circ$ ^{61, 63}. Yan-Mei et al. reported that the structural transition from $\beta\text{-Ga}_2\text{O}_3$ to $\alpha\text{-Ga}_2\text{O}_3$ was found to be irreversible⁶⁴. $\beta\text{-Ga}_2\text{O}_3$ is the only polymorph which is in a stable form until it melts, whereas all the other polymorphs of Ga_2O_3 are metastable and by thermal treatment (above 750 to 900 °C) can transform into $\beta\text{-Ga}_2\text{O}_3$. On the other hand, $\beta\text{-Ga}_2\text{O}_3$ exhibits n-type conductivity, which is related to donor centers involving oxygen vacancies and/or impurities^{59, 65}. Furthermore, the high-temperature stability coupled with deep-ultraviolet transparency make Ga_2O_3 -based materials potential candidates for chemical sensors in extreme environments and transparent electrodes in UV optoelectronics, photonics, and thin-film transistors⁵⁰.

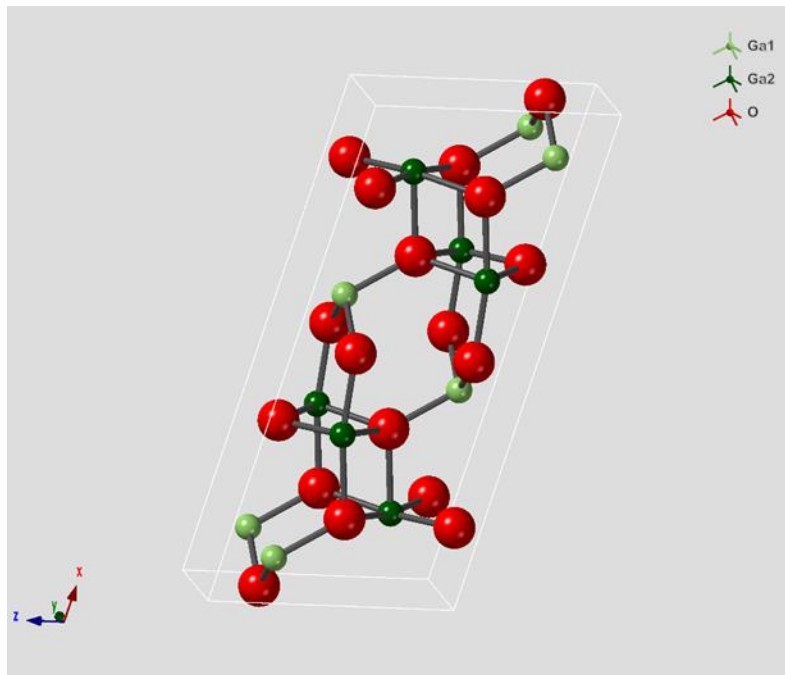


Figure 3.3: Crystal structure of $\beta\text{-Ga}_2\text{O}_3$

3.2.3. $\gamma\text{-Ga}_2\text{O}_3$

Published literature on $\gamma\text{-Ga}_2\text{O}_3$ is almost nonexistent, and even less is known about $\gamma\text{-Ga}_2\text{O}_3$ due to its poor crystalline nature. $\gamma\text{-Ga}_2\text{O}_3$ has a defective spinel, cubic type structure, which

is the same as MgAl_2O_4 type or simply AB_2O_4 with $Fd\bar{3}m$ space group, as shown in Figure 3.4. Zinkevich et al. and Arian et al. reported the experimental lattice parameter values of $\gamma\text{-Ga}_2\text{O}_3$ as $a=8.238$ to 8.30 ± 0.005 Å⁶⁶⁻⁶⁷.

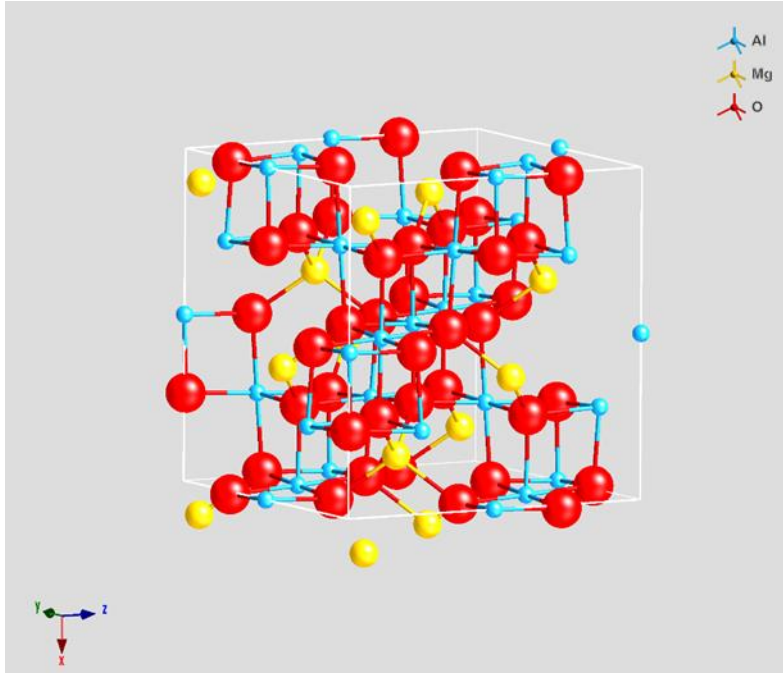


Figure 3.4: Crystal Structure of $\gamma\text{-Ga}_2\text{O}_3$ (Represented by MgAl_2O_4 structure)

3.2.4. $\delta\text{-Ga}_2\text{O}_3$

$\delta\text{-Ga}_2\text{O}_3$ is the fourth polymorph (represented in Figure 3.5), first synthesized by Roy et al. in 1952⁶⁸. From basic studies, Roy et al. reported that $\delta\text{-Ga}_2\text{O}_3$ has C-type rare-earth structure analogous to Mn_2O_3 and In_2O_3 . In contrast, Playford et al. investigated and contradicted the original assumption as $\delta\text{-Ga}_2\text{O}_3$ is merely a nanocrystalline form of $\varepsilon\text{-Al}_2\text{O}_3$ and not a definite polymorph⁶⁹. Roy et al. reported the lattice parameter ‘a’ value as 10.00 Å, whereas Yoshikoa et al. calculated and reported $a=9.401$ Å. The crystal structure is body-centered cubic and $Ia\bar{3}$ space group, shown in Figure 2.5⁷⁰.

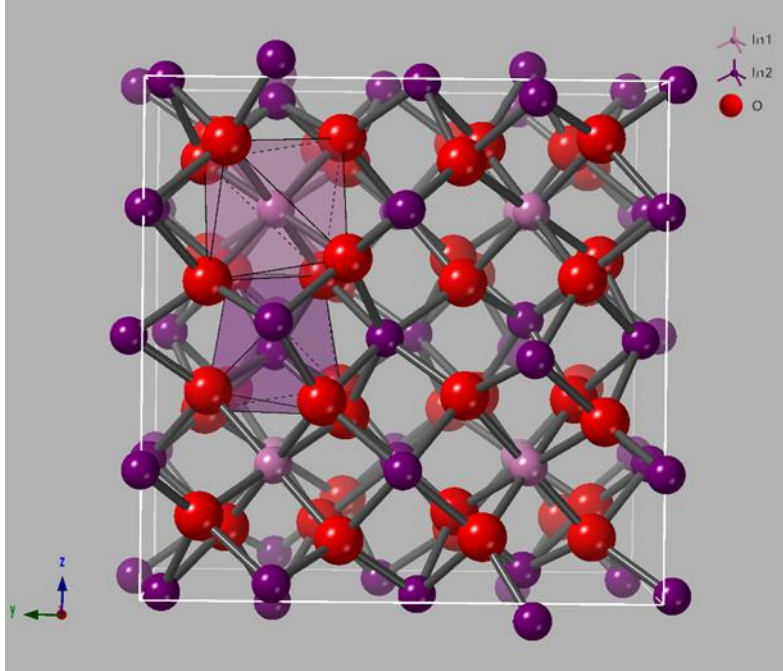


Figure 3.5: Crystal Structure of δ - Ga_2O_3 (represented by In_2O_3 structure)

3.2.5. ε - Ga_2O_3

The ε - Ga_2O_3 crystal structure is the fifth polymorph of Ga_2O_3 , which is the second most stable form after ε - Ga_2O_3 , represented in Figure 3.6. This phase is compatible with common hexagonal wide bandgap semiconductors such as GaN and SiC. Yoshioka et al. and Kroll et al. reported that ε - Ga_2O_3 had orthorhombic crystal structure with a space group of $Pna2_1$, which was simulated by density functional theory, the same as for ε - Fe_2O_3 and κ - Al_2O_3 . The calculated lattice parameters are $a=5.120 \text{ \AA}$, $b=8.792 \text{ \AA}$, and $c=9.410 \text{ \AA}$. The refractive index is 1.6 with a bandgap of $\sim 4.9 \text{ eV}^{59}$. ε - Ga_2O_3 has a large spontaneous polarization due to which it could produce high-density 2D electron gases. These gases act as conducting channels in heterostructures field effect transistors.

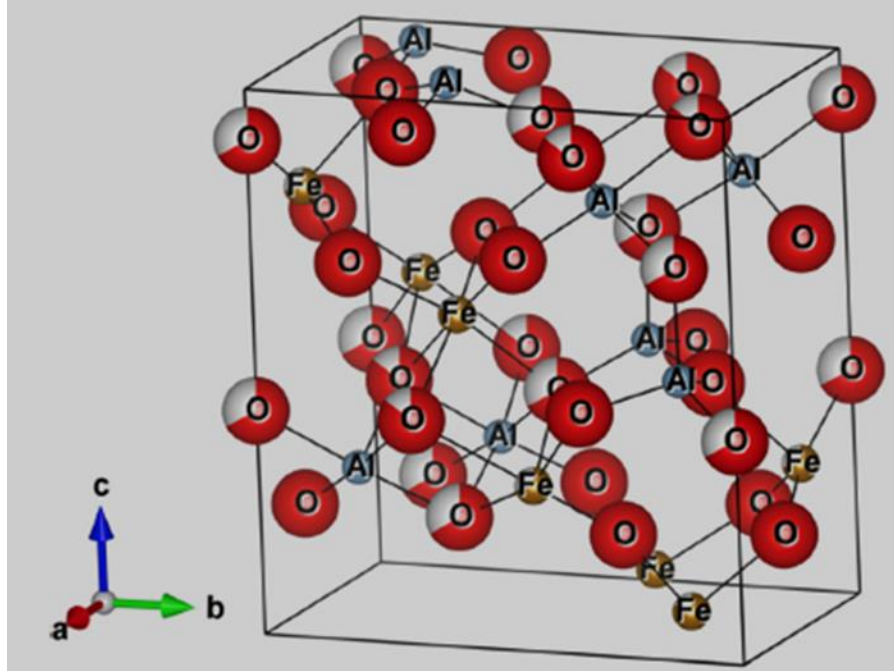


Figure 3.6: Crystal Structure of ϵ -Ga₂O₃ (represented by AlFeO₃ structure ⁷¹)

3.3. Metal Oxide (MO) Semiconductor Properties

In this section, we mainly focus on the fundamental properties of Ga₂O₃ and the effect of dopants into Ga₂O₃ thin films.

Over the past 30 years, a good deal of research effort has been directed towards the development of oxide semiconductor devices for practical applications in several industries²⁸⁻²⁹. Generally, the promising advantages of wide-bandgap oxides have attracted the scientific and engineering research community to utilize them in electronics, photonics, catalysis, electro-optics, integrated sensors, magneto-electronics, photovoltaics, and other energy-related applications^{47-48, 72-74}. In order to further improve the performance of Ga₂O₃, doping using either isovalent and/or multivalent ions(s) has been considered in the literature. For instance, doping of β -Ga₂O₃ with Sn⁷⁵, Cr⁴², Ti³¹, Zn⁷⁶, or W⁴³ induces changes in the properties. Li et al. reported that Pr doping in β -Ga₂O₃ affected the morphological and optical properties, i.e., it will decrease the average grain size from 26 to 19 nm and bandgap also decreased continuously from 4.97 to 4.8 eV with increasing Pr mol% from 0 to 1.5%⁷⁷. On the other hand, Takakura et al. fabricated the Ga₂O₃

films at room temperature and performed annealing between 400 to 900 °C, which changes the bandgap from 4.9 to 5.2 eV after adding Si or Ge impurities to the film⁷⁸. Kudou et al. reported, Sn doping results in phase transformation from β to γ and annealing at 900 °C improved the crystallinity⁷⁹. Multiple chemical valence states of W in β -Ga₂O₃ thin film causes amorphization, reported by Rubio et al⁴³. Kumar et al. reported that Ga₂O₃ films deposited at 25 °C exhibit excess oxygen in comparison with stoichiometric films deposited over 300 °C, while the bandgap is increased from 4.66 (25 °C) to 5.17 eV (800 °C)⁵⁰. Stepanov et al. reported that β -Ga₂O₃ can exhibit up to three different emissions, namely UV (3.2 to 3.6 eV), blue (2.8 to 3.0 eV), and green (2.4 eV)²⁹. Considering that the β -Ga₂O₃ bandgap is ~5 eV, it seems highly unlikely that UV luminescence derives from band-edge recombination. Instead, the UV band can be associated with recombination of free electrons and self-trapped hole. In β -Ga₂O₃ crystals, a correlation will be observed between the blue band intensity and its resistivity. In other words, the oxygen vacancies are responsible for the n-type conductivity in β -Ga₂O₃, which also play a major role in the blue emission process²⁹. Harwig et al. described how blue emission derives from the recombination of an electron on a donor (V_o and Ga_i) and a hole on an acceptor (V_{Ga} and/or V_o-V_{Ga})⁸⁰. Lastly, green emission was obtained only after doping with specific metal elements. Green emission was obtained by doping Be, Ge, and Sn⁸⁰. Villora et al. suggested that Fe and Cu both acted as an obstacle to blue emission⁸¹. The green luminescence was proposed to be associated with self-trapped or bound excitons. Sun et al. described how fabrication of Ga₂O₃ films at 500 °C under Ar and N₂ environments alters the film surface and optical properties, i.e., crystallinity is increased and at the same time the bandgap is decreased⁸². Marie et al. reported that performing the annealing at temperatures of 1000 °C in an N₂ atmosphere will affect the electrical properties of Ga₂O₃ thin films, i.e., sheet resistance was decreased with increasing substrate temperatures⁸³. Marie et al. also mentioned that the refractive index remained almost constant with increasing substrate temperatures⁸³. Dong et al. described that annealing at 1000 °C in an N₂ environment will affect the chemical, structural, and optical properties of Ga₂O₃ thin films, i.e., films displayed lowest oxygen vacancies, highest film crystallinity and highest bandgap of 4.87 eV, respectively⁸⁴.

Ramana et al. reported the electrical properties of Ga₂O₃ thin films, noting that as the electrical resistivity is decreased and index of refraction is increased with increasing the substrate temperature⁸⁵. Fortunato et al. described that crystallinity, mobility, and concentration were calculated and found the linear dependency between mobility and crystallite size for gallium doped zinc oxide thin films⁸⁶. Manandhar et al. suggested doping of Ti into β-Ga₂O₃ to alter the structural and optical properties. Ti content beyond 1.5 at% results in the composite phase of Ga₂O₃-TiO₂ and as a result, reduction in bandgap from 5.40 to 4.47 eV³¹. Sun et al. reported that varying film thickness of Ga₂O₃ films deposited at 500 °C under Ar and N₂ atmosphere can affect the structural and optical properties, i.e., crystallinity increased and the transmittance was more than 80% in the visible region⁸⁷. Battu et al. described Ti content beyond 2 at% to result in an improvement in nanomechanical properties of β-Ga₂O₃ films, i.e., hardness increased from 25 to 30 GPa and elastic modulus reduced from 280 to 310 GPa⁸⁸. Stepanov et al. reported that β-Ga₂O₃ is a poor thermal conductor, smaller than that of GaN and half of the sapphire. The Ga₂O₃ material had crystalline anisotropy, which means different thermal conductivity in different crystal directions²⁹. Stepanov et al. and Guo et al. reported that the thermal conductivity is highest along [010] plane and lowest along [100] plane directions, i.e., 27.0±2.0 W/mK and 10.9±1.0 W/mK, respectively⁸⁹. These values were calculated at room temperature using the time domain thermoreflectance method.

3.4. Metal Oxide Gas Sensors Applications

Thin film gas sensors are becoming most promising and popular in today's real-time applications²⁸. In general, the basic properties of gas sensors must be the high sensitivity to the gases, repeatability with high efficiency, and mainly low-cost fabrication consisting of simple design^{33,90}. Though different techniques are available for gas sensing, metal oxide semiconductor devices are the most promising and well established, offering a wide range of materials and sensitivities for various gasses in various environments. Metal oxide semiconductor gas devices have to be reliable and capable of inorganic and organic gas detection in indoor as well as outdoor environments.

In more recent years, the attention and development activities have been shifted towards other promising materials such as gallium oxide²⁸. Ga₂O₃ is the most promising metal oxide semiconductor due to its high thermal stability, which means these materials can perform well in harsh environmental conditions where high temperatures and pressures are common, and can operate over a long period of time²⁸⁻²⁹. Furthermore, Ga₂O₃ is recognized as one of the widest bandgap oxide materials, which shows tremendous potential properties, includes excellent electrical properties, high mobility, chemical stability and high transparency^{33, 63, 91-93}. β-Ga₂O₃ acts as an n-type semiconductor device at higher temperatures, where semi conductivity is inversely proportional to the partial pressure of oxygen⁹⁴⁻⁹⁵. In other words, the material's semi conductive nature alters based on oxygen deficiency. At elevated temperatures, β-Ga₂O₃ has a lack of oxygen in the crystal lattice, which is in dynamic balance with the oxygen in the surrounding ambient. Ionized oxygen vacancies form donors and eventually affect the conductivity of the oxygen sensor. Therefore, increase in the concentration of reducing gases and/or reduction in the oxygen in the surrounding ambient in which a sensor is located leads to an increasing number of conducting electrons and therefore an increase in conductivity⁹³. In addition, conductivity will decrease drastically at lower partial pressures, as β-Ga₂O₃ does not undergo any phase transformation⁵⁹. Fleischer et al. reported that β-Ga₂O₃ exhibits the same charge carrier mobility, irrespective of either monocrystalline or polycrystalline state, where electron mobility is independent on its grain boundaries⁶⁵. The melting point is approximately 1800 °C, which makes β-Ga₂O₃ sensors potential candidates to work beyond 1000 °C. Despite this, due to the low electrical conductivity, the favored performing temperatures are below 500 °C. Eranna et al. reported that β-Ga₂O₃ material can be used to detect oxygen, which is usually operated with the bulk-volume-defect in equilibrium between 900 and 1000 °C. Eranna et al. also reported that at lower temperatures the volume-defect equilibrium is not attainable and sensor response is mainly affected by the surface²⁸. At operating temperatures between 500 and 900 °C, β-Ga₂O₃ can be used to detect reducing gases such as CH₄, propane, H₂, and CO and chemical solvents.

Intrinsic β -Ga₂O₃ is a wide bandgap insulating oxide, but it can be changed to an *n*-type semiconductor by selective doping³¹. While the mechanism of *n*-type conduction in β -Ga₂O₃ appears to be mostly by electrons generated from oxygen vacancies ionization, the overall electrical conductivity of the resulting materials upon doping is still under debate. Doping with carefully chosen metallic ions can significantly alter the properties of β -Ga₂O₃^{31, 43, 96}. Innovative approaches to tailor the functionality and/or promising future applications in emerging technologies are the primary considerations currently driving the significant interest in Ga₂O₃ single-phase materials and Ga₂O₃-based multi-component architectures or hybrid materials with nanostructured morphologies. For instance, excellent luminescence has been demonstrated in Sn- or Cr-doped Ga₂O₃ nanowires for application in display devices⁴². Similarly, solution-processed Ga₂O₃ dielectrics are promising to contribute to the development of next-generation, large-area green electronics. Enhanced photocatalytic activity for application in energy-harvesting devices has been reported for metal-doped Ga₂O₃ or metal/Ga₂O₃ hybrid materials. Doping metal ions, such as Ni⁹⁷, Zn⁸⁶ and Pb⁷⁶, into Ga₂O₃ has been reported to enhance the photocatalytic activity of Ga₂O₃. From an optical properties point of view, doping with Sn⁷⁵, Cr⁴², Cu⁴⁰, and W⁴³ metals into β -Ga₂O₃ has been reported to induce changes in the optical absorption and bandgap.

Li et al. reported that Ga₂O₃ sensors doped with Zn showed response times of 100 s at the operating temperature of 450 °C, whereas Ce doping reduced the response time to 40 s at the same operating temperature. On the other hand, at the operating temperature of 520 °C, Sb- and W-doped Ga₂O₃ sensor film had the same response time of 90 s. Y. Li et al. also reported that doping the gallium oxide thin films with Zn, Ce and W reduced the operating temperatures, and concluded that Ga₂O₃ films doped with Zn, Ce, and W are promising candidates for oxygen sensing applications⁹⁸.

Table 3.1: Characteristics and performance metrics of gallium-based sensors and dopants.

Gallium Oxides (dopants)	Sensing Gas	Operating Temperature (°C)	Range of detection limits	Sensing elements from	Sensor physical properties
β -Ga ₂ O ₃	O ₂	480 – 820	7x10 ⁻⁵ Pa	Sputtered thin film from alumina substrate (2 μm)	Electrical conductivity by using interdigital structure
Ga ₂ O ₃ , SnO ₂ , ZnO ₂ , TiO ₂	General	Room Temperature	---	Thin films	Electrical conductivity & Chemisorption studies
Metal Oxides (Ga ₂ O ₃ , SnO ₂ , SrBiO ₃ , BaSnO ₃)	CH ₄ , Co, Auto mobile exhaust gases	500 – 1000	550 ppm (for CH ₄) 500 ppm (for CO)	Sputtered/screen-printed films (1 to 5 μm)	Electrical resistance by using interdigital Structure
Ga ₂ O ₃ -Ta ₂ O ₅ , WO ₃ , NiO, AlVO ₄	NO NH ₃ O ₂	600 -1000	300 ppm 30 ppm 10000 ppm	Thin films on BeO with different top Surfaces	Element electrical resistance
Ga ₂ O ₃ (with Rh, Ru, Ir)	Ethanol Propane	540 – 800	25 to 50 ppm	Thick film on alumina substrate (~2 μm)	Element electrical conductivity
Ga ₂ O ₃ (SnO ₂)	CH ₄ CO iso-Butane	500 – 950	10000 ppm 10000 ppm 100 ppm	Paste screen-printed onto alumina Substrate	Electrical conductivity by using Interdigital Structure
Ga ₂ O ₃ (ZrO ₂ , TiO ₂ , MgO)	O ₂	900 – 1200	0.002 to 0.2 bar	Layered sandwich structure with Dopant	Electrical conductivity by using Interdigital Structure

Summarizing the above-mentioned table, no one has studied the effect of Mo incorporation into Ga_2O_3 . The ionic radii for Mo^{6+} and Ga^{3+} are very close to each other, i.e., 0.56 and 0.62, respectively. Furthermore, the crystal radii are also very close, at 0.73 and 0.76 for Mo and Ga atoms. Therefore, Mo^{6+} ions can go into the lattice as substitutional metal dopants and acts as donors. Y. Li, et al. reported that using donor dopants may lower the sensor resistivity⁹⁸.

Chapter 4: Materials and Experimental Methods

4.1. MATERIALS

Sputtering Targets: The sputtering target materials for RF deposition were obtained from Plasmaterials and Kurt J. Lesker. The Ga_2O_3 target of 2 in. diameter and 0.125-inch thick with 99.999% purity and Mo-target of 2 in. diameter and 0.125-inch thick with 99.95% purity were employed to evaluate the modification caused to the structural, chemical, and sensor properties with varying Mo concentration in Ga_2O_3 matrix. The targets were fabricated in such a way that they will be fit exactly fit in the equipment and used for thin-film depositions. The corresponding target images are represented in Figure 4.1. A thin Cu backing plate is used to protect the target.

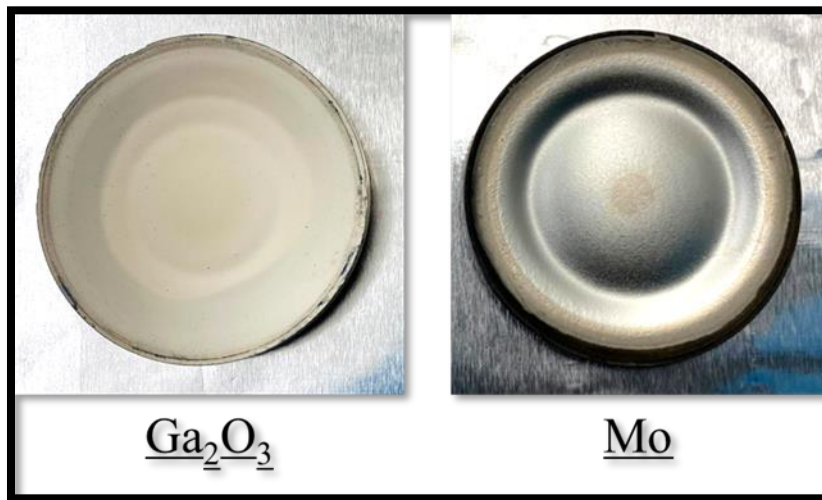


Figure 4.1: Sputtering Targets

Substrates: Three different types of substrates were employed to deposit intrinsic Ga_2O_3 and with co-sputtering of variable Mo concentration to evaluate the properties.

1. Silicon (Si (100)), used to facilitate the characterization of films physical and chemical properties.
2. Quartz glass, to evaluate the optical characteristics.

3. Al₂O₃, with integrated Pt interdigital electrodes of 200 nm thick with a distance of 10 μm between electrodes, to evaluate the sensor properties.

4.2. SUBSTRATE CLEANING

The silicon and quartz samples were acquired from University Wafer Inc and Chemglass Life Science, respectively. The silicon substrates of P-type were cleaned by a bath of 99.9% ethanol for 15 minutes to remove organic residue and films from silicon wafers. The standard RCA cleaning (referred to as standard clean-1 or SC-1) was developed by Werner Kern in 1965, at RCA laboratories (Radio Corporation of America), to eliminate the organic contaminants, i.e., organic clean along with particle clean, to abolish the thin oxide layer, and to eliminate the ionic contamination. The following procedure was performed:

1. SC-1, used to remove the insoluble organic contaminants at a mixture of 5 parts (H₂O), 1 part 30% (H₂O₂) and 1 part 27% (NH₄OH). This solution was processed by heating 50 ml of deionized (DI) water to a temperature of 70 °C, for 10 minutes and then adding every 10 ml of NH₄OH and H₂O₂ to the DI water.
2. Immersion in 1:100 solution of HF: H₂O, in order to remove native oxide.
3. SC-2, for the removal of heavy and ionic metal atomic-level components at a ratio of 6 parts (H₂O), 1 part 30% (H₂O₂) and 1 part (HCl). The preparation of SC-2 solution was made by 10 ml each of H₂O₂ and HCl to 50 ml of water.

The silicon substrates were soaked for 10 minutes each solution and followed by 5 minutes of DI water rinse after each soak.

4.3. THIN FILMS SYNTHESIS - SPUTTERING DEPOSITION SYSTEM

The thin film synthesis was carried out by radio frequency (RF) magnetron sputtering. Figure 4.2 refers to the simple schematic mechanism of the sputtering process. The sputtering

deposition process involves the ionized atoms of inert gas, in our case Argon (Ar), by applying the voltage. A voltage of 13.56 MHz was applied to the targets or cathode. As a result, the positively charged gas ions (Ar^+) attract and bombard the negatively biased target surface, which causes the targets material to sputter off in the form of fine vapor to cover the substrate. This vapor form condenses and makes a thin layer which is called a thin film. On the other hand, secondary electrons also form during the bombardment, but these electrons do not contribute significantly to sustaining the ejected atoms onto the substrate surface, and are likely to cause unwanted heating. The sputtering system was equipped with magnets which were placed on the backs of the targets; due to these magnets, the secondary electrons remain closer to the target by creating the magnetic field. This mechanism will help in ionization efficiency, or in other words, higher deposition rates⁹⁹.

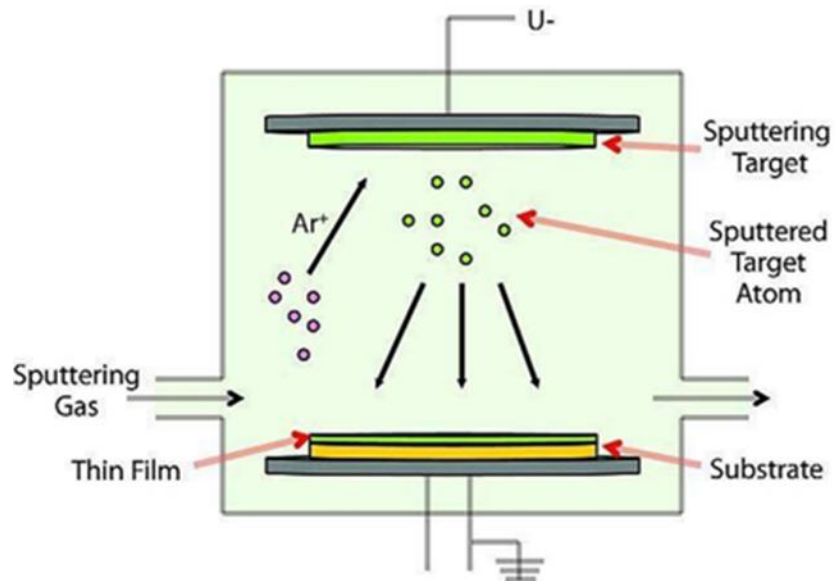


Figure 4.2: Schematic Representation of Sputtering Process

An Excel Instruments sputter deposition system, Model DCSS-12, was used for thin film depositions. In this research, two targets, namely Ga_2O_3 and Mo, and a pair of electrodes were placed on cathode and Si, with quartz and Al_2O_3 placed towards the anode. The samples were

thoroughly cleaned by RCA technique before being introduced into the vacuum chamber. The samples were placed on the substrate holder with clips and connected with a K-type thermocouple located within the sample holder/heater. The target-to-substrate distance was maintained at 7 cm for all the depositions. The deposition chamber was evacuated to a base pressure of $\sim 10^{-7}$ Torr. The sputtering guns were chilled by water using a Polyscience recirculation chiller. The deposition was made by co-sputtering of Mo metal and Ga₂O₃ ceramic targets. A sputtering power of 20 W was initially applied to each target while introducing high-purity argon (Ar) into the chamber to ignite the plasma. Once the plasma was ignited, the power for each target was increased to their respective sputtering power for reactive deposition. The flow of Ar and oxygen (O₂) were controlled using MKS mass flow meters. Before each deposition, the targets were pre-sputtered for 20 min with a closed shutter above the gun. Deposition of Mo-doped Ga₂O₃ (referred as GMO hereafter) samples was performed by keeping Ga₂O₃ sputtering power constant at 100 W and varying the Mo power in the range of 0-100 W. The intended purpose of variable sputtering power to the Mo target was to vary the amount of Mo content into Ga₂O₃ films or to produce GMO samples with variable Mo content. The substrate temperature (T_s) was fixed at 500 °C for all the GMO films. The primary reason for this is the fact that a deposition temperature of 500 °C is critical to promote the formation of nanocrystalline β -Ga₂O₃ films, as reported previously elsewhere. For comparison, intrinsic Ga₂O₃ films without any Mo dopant were also deposited under the same temperature and sputtering power conditions. For clarity and understanding of the results, the GMO sample identification numbers were generated using the sputtering power applied to the Mo target. Different composition of samples was deposited using this technique by varying target sputtering power in the Mo target, as presented in Table 4.1. The schematic layout of the

sputtering system and their components employed for the fabrication of GMO films is presented in Figure 4.3.

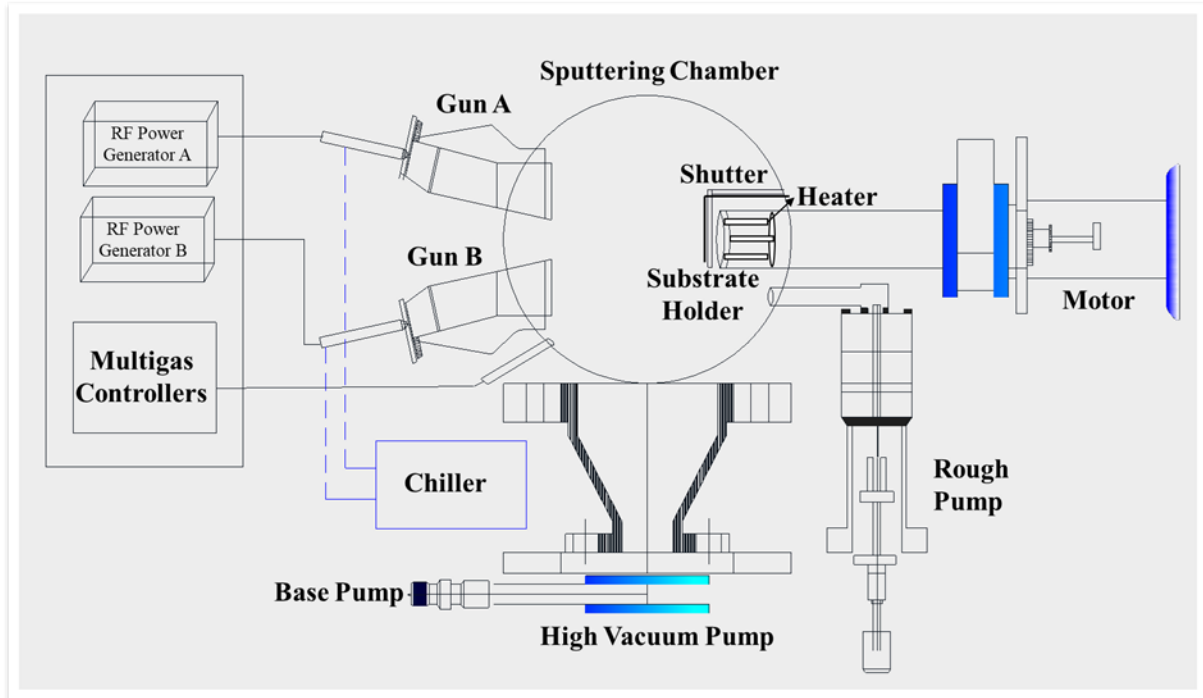


Figure 4.3: The schematic layout of the sputtering system employed for the fabrication of thin film depositions

Table 4.1: List of the samples and deposition conditions .

Sample ID	Target Sputtering Power (W)		Temperature (°C)	Ar:O ₂ flow (sccm)
	Ga ₂ O ₃	Mo		
GMO-0	100	0	500	30:10
GMO-20	100	20	500	30:10
GMO-40	100	40	500	30:10
GMO-60	100	60	500	30:10
GMO-80	100	80	500	30:10
GMO-100	100	100	500	30:10

4.4. ANALYTICAL METHODS

4.4.1. Grazing Incidence X-Ray Diffraction (GIXRD)

Grazing incidence X-ray diffraction (GIXRD) is an analytical technique for performing X-ray diffraction on thin films. The basic principle involves directing monochromatic X-rays, generated by a cathode ray tube, at various incident angles towards the substrate, and observing how these X-rays diffract due to the atoms. These diffracted X-rays are collected by the detector and allow us to collect various information such as the phase identification and crystal structures of the substrate material. Figure 4.4. represents the schematic working mechanism of X-ray diffraction (XRD). The interaction of the incident X-rays with the substrate material produces constructive interference and a diffracted beam when conditions satisfy Bragg's Law (Equation 1).

$$n\lambda = 2d\sin\theta \quad (1)$$

In Equation 1 above (Bragg's Law), n is an integer referred as the order of reflection, λ = X-ray wavelength (1.54056 Å for Cu K α radiation), d = the interplanar spacing between the planes, and θ = the Bragg's angle.

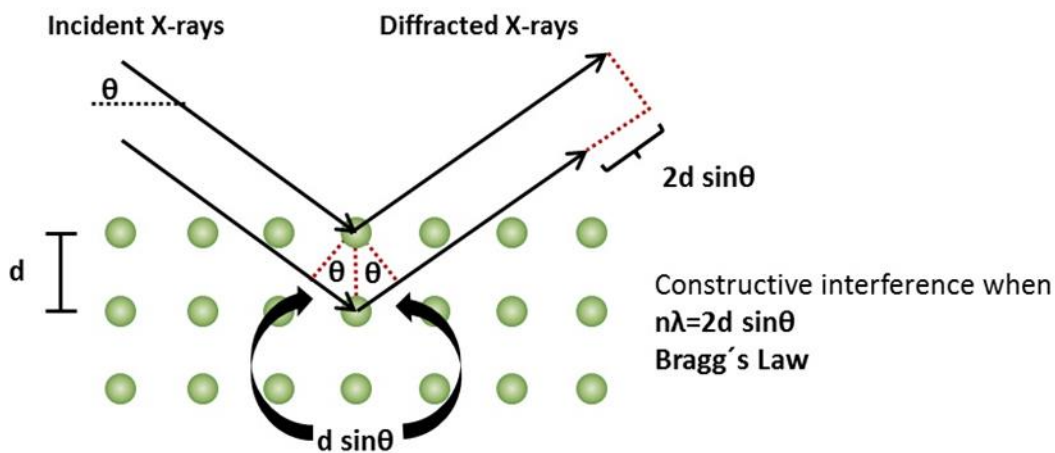


Figure 4.4: Schematic representation of X-rays and Bragg's Law

The GIXRD characterizations for Ga_2O_3 and GMO thin films were performed at room temperature using a Bruker D8 advance X-ray diffractometer, shown in Figure 4.5. The measurements were made for intrinsic Ga_2O_3 and as a function of variable Mo content in the GMO samples deposited on an Si wafer. The grazing incident angle was fixed to 1° for the incoming X-ray beam, so that it was used to study only surfaces and layers for the thin films. The detector scan mode was used, where the detector can move freely in the plane of incidence to receive the various diffraction patterns. The detector varies between the angles of 10° to 67° at a scan rate of 0.5 sec/step. The collected diffracted data was analyzed using EVA software in order to correlate XRD peaks to check the crystal structure and lattice parameters. The same experimental conditions were maintained for all the set of films.



Figure 4.5: Bruker D8 Advance X-ray Diffractometer to characterize the Ga_2O_3 and GMO films

4.4.2. X-ray Photoelectron Spectroscopy (XPS)

X-ray photoelectron spectroscopy (XPS) was used to corroborate the composition of the films and to determine the chemical bonding of the ionic species in the film. XPS measurements allowed probing the chemical characteristics of the surface. The XPS measurements were made on the as-deposited GMO films and with variable Mo content. The samples were mounted on a Cu stub with the help of double-sided Cu tape and analyzed using a calibrated Kratos Axis Ultra DLD spectrometer (Kratos Analytical, Manchester UK) which has a high-performance Al K_{α} (1486.7 eV) spherical mirror analyzer. A piece of Cu tape was attached on the sample surface up to the stub surface in order to avoid charging issues (e.g., peak broadening, peak shifting, etc.). Despite this, the charge neutralizer was used to compensate for the surface charging effects. Survey and multiple high-resolution scans were collected at pass energy of 160 and 40 eV, respectively. Survey spectra were obtained over the binding energy (BE) range of 1400-(-5) eV with a step size of 0.5 eV, whereas high-resolution scans were obtained with an energy step of 0.1 eV. The analysis area ($700 \times 300 \mu\text{m}$) is referred to the full width at half maximum (FWHM) of 0.70 eV for Ag 3d_{5/2} collected at 40 eV pass energy. High-resolution scans were obtained for Ga 2p, Ga 3d, Mo 3d, O 1s, and C 1s peaks. Each high-resolution scan was recorded for at least 8 sweeps in order to get well-resolved spectra. Both survey and high-resolution scans were collected under ultra-high vacuum (UHV- 2×10^{-9} torr) condition. C 1s binding energy at 284.8 eV was used for the charge reference. Survey and high-resolution spectra were analyzed using CasaXPS V2.3.16 to obtain the atomic composition and for more in-depth studies, respectively. Peak areas were calculated employing both Gaussian/Lorentzian (GL(30)) line shape and line asymmetry and Shirley background subtraction, whereas the compositional analysis was performed using the relative

sensitivity factors for the instrument. For a concentration of various elements present, i.e., Ga, Mo, and O, the error estimation was ± 0.01 at% for metals (Ga, Mo) and ± 0.1 at% for oxygen.

4.4.3. Rutherford Backscattering Spectroscopy (RBS)

Rutherford backscattering spectrometry (RBS) measurements were made using an NEC 3 MV tandem accelerator (9SDH-2) to understand the chemical composition and elemental depth distribution of the GMO–Si (100) samples. An incident ion beam of 1.5 MeV He⁺ at 0° angle of incidence was used. The backscattered ions were detected using a silicon barrier detector at a scattering angle of 160°. Composition and depth profiles were determined by simulating the experimental backscattered spectra from ion beam analysis using SIMNRA software. The simulated curves were calculated using SIMNRA code for the fixed set of experimental parameters: (a) the incident He⁺ ion energy; (b) the integrated charge; (c) the energy resolution of the detector; (d) the scattering geometry; (e) and pure Ga₂O₃ stoichiometry. The error of estimation is ± 0.02 at% ± 1 nm for concentration and thickness/depth values, respectively. The schematic of the setup is depicted in Figure 4.6.

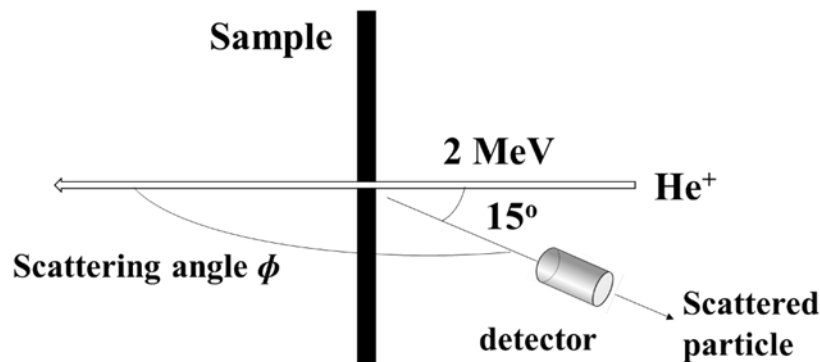


Figure 4.6: Schematic representation of RBS working principle

4.4.4. Spectroscopic Ellipsometry

Spectroscopic ellipsometry was utilized to find the optical properties and surface/interface characteristics of the GMO coatings. Δ and ψ were determined using a J.A. Woollam vertical variable-angle spectroscopic ellipsometer in conjunction with a computer-controlled Berek wave plate compensator (J.A. Woollam Co, Lincoln, NE). Measurements were done over a wavelength range of 380-900 nm at 300 K in the air with 60°, 65°, and 70° acting as the angles of incidence for the measurements. Post analysis of the ellipsometry data was performed using commercially available WVASE32 software.

Optical properties and microstructure of the samples can be related to the measured angles via:

$$\rho = \frac{R_p}{R_s} = \tan \tan \Psi \exp \exp (i\Delta) \quad (2)$$

where R_p is the complex reflection coefficients of the light polarized parallel to the plane of incidence. Additionally, R_s is the light perpendicular to the plane. In order to minimize the mean-squared error (MSE), the Levenberg-Marquardt regression algorithm was used.

$$\text{MSE} = \frac{1}{2N-M} \sum_{i=1}^n \left[\left\{ \frac{(\Psi_{exp} - \Psi_{calc})}{\sigma_{\Psi_i}^{exp}} \right\}^2 + \left\{ \frac{(\Delta_{exp} - \Delta_{calc})}{\sigma_{\Delta_i}^{exp}} \right\}^2 \right] \quad (3)$$

where Ψ_{exp} , Ψ_{calc} , and Δ_{exp} , Δ_{calc} is the measured (experimental) and calculated ellipsometry functions, N is the number of measured Ψ , Δ pairs, M is the number of fitted parameters in the optical model, and σ are standard deviations of the experimental data points.

In order to factor in optical inhomogeneity, multiple measurements were performed, and analyses were done to calculate the level of inhomogeneity in the films. Standard procedure was used and determined that the variation in index of refraction was $\Delta n = \pm 0.01$.

4.4.5. UV-Vis Spectroscopy

The optical characteristics of GMO films were evaluated using spectrophotometry measurements employing Cary 5000 UV-Vis-NIR double-beam spectrophotometer (shown in Figure 4.7). GMO films were deposited on a quartz glass substrate to evaluate the optical properties such as an absorption edge and transmittance, which allows us to calculate the bandgap/energy gap of the films. The measurements were carried out in the wavelength range of 175 to 3300 nm with the help of deuterium emitter for UV and halogen lamp for visible regions.

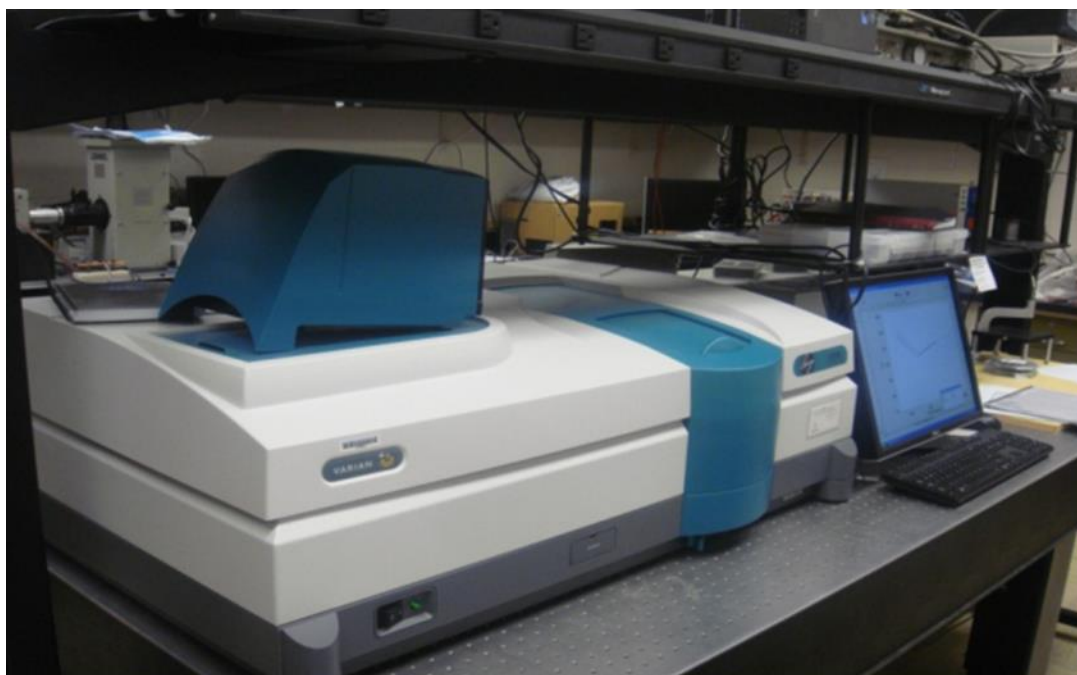


Figure 4.7: Cary 5000 UV-Vis-NIR double-beam spectrophotometer

The light beam is split into component wavelengths using a diffraction grating and a slit helps to send a beam of monochromatic light into the next section which has a rotating disc. The rotating disc consists of three different segments, namely a transparent section, opaque black section, and a mirrored section. Some portion of the monochromatic light hits the transparent section of the disc and passes to the sample, whereas the other portion of the light hits the mirror and get reflected. This light beam passes through the reference cell and is collected by the detector.

If the light hits the black opaque section, the light gets blocked. This enables the system to make corrections for any current generated in the absence of light.

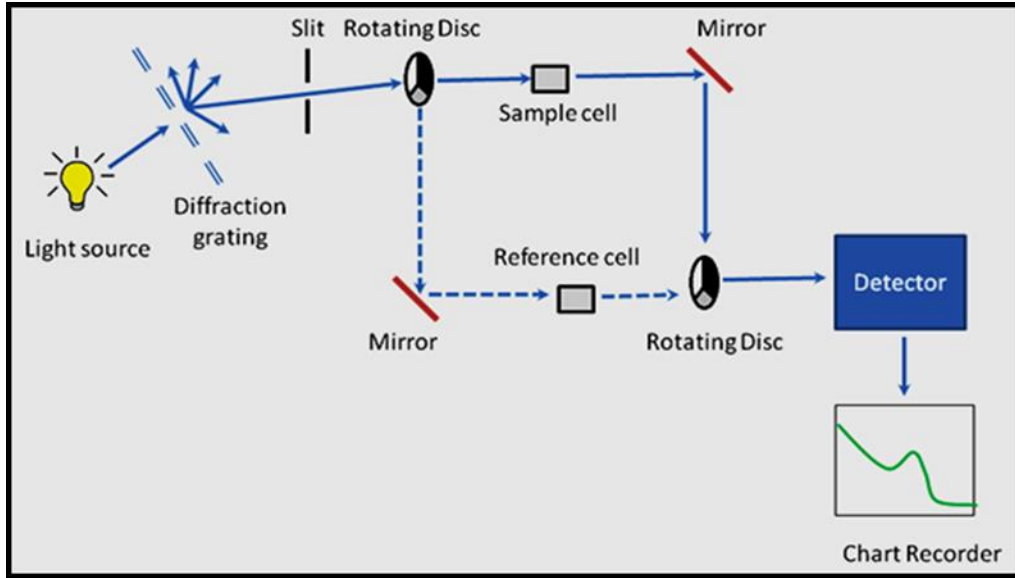


Figure 4.8: Schematic representation of UV spectrophotometry working principle

The absorption coefficient (α), determined using the thickness (t) of the GMO films and the transmittance spectra (T) using the relation

$$\alpha = \frac{-\ln T}{t} \quad (4)$$

The photon energy ($h\nu$) will be calculated by considering the wavelength (λ)

$$\alpha = \frac{-\ln T}{t} \quad (5)$$

The photon energy ($h\nu$) will be calculated by considering the wavelength (λ)

$$h\nu = \frac{1240}{\lambda} \quad (6)$$

Then we calculate the bandgap using the following relation

$$(\alpha h\nu) = B (h\nu - E_g)^{1/2} \quad (7)$$

where $h\nu$ is the energy of the incident photon, α the absorption coefficient, B the absorption edge width parameter, and E_g the bandgap.

4.4.6. Scanning Electron Microscopy (SEM)

The Surface morphology of the Ga_2O_3 and GMO films deposited on Si were characterized by the SEM technique. SEM is a technique that employs a focused beam of electrons to expose the observed features presented on the sample surface. The high-energy electrons are emitted from an electron gun, which is focused towards the specimen to scan the surface. The electron beam is scanned in a raster scan pattern where the beam illuminates one point at a time and produces images. The Ga_2O_3 and GMO samples were mounted on the 1-inch-diameter stage using the double-sided carbon tape to avoid charging issues and assist electron flow. The SEM technique provides images with detailed morphological characteristics such as particles and grain sizes at adjustable magnifications. The equipment used to perform the experiments is a Hitachi S-4800 electron microscope, represented in Figure 4.9.

The ImageJ software program was used for further analysis of the Ga_2O_3 and GMO thin films to measure their grain size regions.



Figure 4.9: Hitachi S-4800 SEM

4.4.7. Nano-Indentation Testing

The nano-mechanical analysis for the thin films was carried out by nano-indentation and nano-scratch techniques. A Hysitron 750, represented in Figure 4.10, was equipped for both the indentation and scratch analysis. The indentation technique offers detailed nanomechanical testing and solutions for tailored mechanical characterizations at the nanoscale level.



Figure 4.10: Hysitron 750 Nano-indentation System

The nano-indentation measurements were made employing a triangular pyramid Berkovich diamond indenter with a normal angle of 65.3° between the tip axis; the faces of the triangular pyramid and the effective size of the apex are about 100 nm. A commonly accepted rule suggests that the substrate measurements can be obtained if the indentation depth is kept less than 10% of the film thickness. At such small indentation loads, the produced indents on the thin films can be microscopic to submicroscopic. Because of their small size, measuring these indents is thus very difficult and not accurate. Therefore, the most common method so far has been to gauge the size of the indentation from the loading and unloading curves generated during the test performance.

The deformation during loading is assumed to be of elastic/plastic tendency, whereas during unloading, it is assumed that only elastic displacements are recovered, and it is this predominantly elastic nature of the unloading curve that facilitates analysis. Therefore, the standard procedure was employed to derive the mechanical properties with the help of loading and unloading curves¹⁰⁰⁻¹⁰¹. The method developed by Oliver and Pharr, represented in Figure 4.11, was employed to calculate the mechanical characteristics of hardness and reduced elastic modulus (H and E_r , respectively),

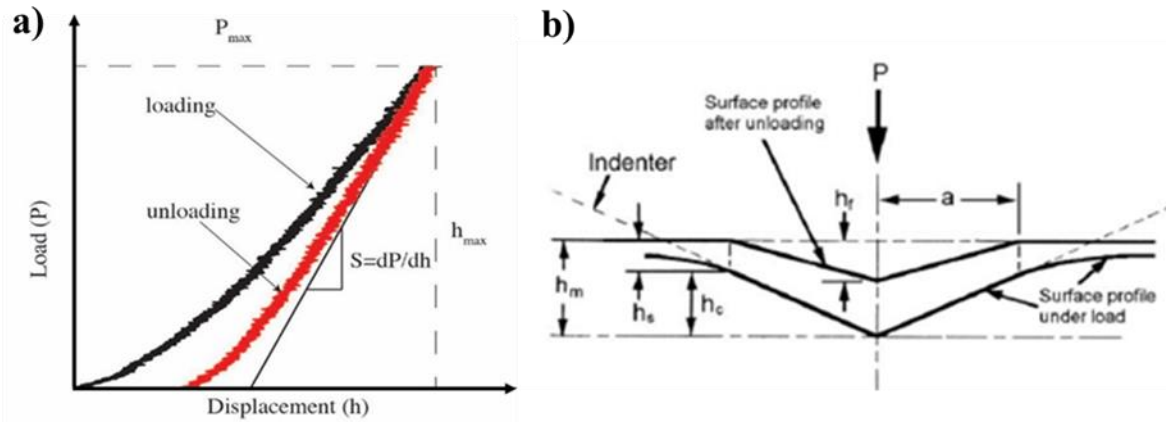


Figure 4.11: a) Schematic illustration of indentation load-displacement data and b) Schematic illustration of the unloading process showing parameters characterizing the contact geometry

where P is the indentation load, h_m is the maximum displacement, h_c is the contact depth, h_s is the elastic surface displacement at the perimeter of contact, and h_f is the depth of residual impression after unloading.

Using this approach, E_r can be calculated by finding the stiffness (S) of the film from the slope of the unloading curve. The relation between E_r and S can be described using:

$$E_r = \frac{\sqrt{\pi}}{2} \frac{S}{\sqrt{A}} \quad (8)$$

where A is defined as the area of contact at peak load:

$$A = F(h_c) \quad (9)$$

To find the hardness value H , the same value for the area of contact is used along with the maximum load (P_{max}):

$$H = \frac{P_{max}}{A} \quad (10)$$

To minimize the substrate effect, the load-controlled indentation tests were performed initially on each sample to determine the maximum depth that would not be more than 10% of the total film thickness. Seventeen indents of selected 100 μN load were performed at 0.2 s^{-1} strain rate, and the average H and E_r values were calculated on each sample.

4.4.8. Nano-Scratch Testing

For nanostructured samples, film or coating, the adhesion to the substrate is one of the paramount characteristics related the coating quality and life endurance¹⁰²⁻¹⁰³. Therefore, the GMO film adhesion was analyzed by nano-scratch test (Hysitron T1750 Tribo nano-indenter). This test was performed at room temperature under load increments from 0 to 8000 μN . The same standard triangular pyramid Berkovich diamond indenter tip was used. The length of the scratch was 16 μm and the scratch speed was 0.18 $\mu\text{m/s}$.

4.4.9. Electrical Analysis

For electrical analysis, Ecopia HMS 3000 Hall measurement system was used to determine the electrical properties such as resistivity, conductivity, and mobility. Four electrical contacts on the sample were made using a two-part conducting epoxy and silver wires. In this method, voltage and current were measured using eight different combinations of the four contact points on the sample. Current was applied to the test sample using four small contacts and the corresponding voltage was measured on a flat arbitrarily shaped sample of uniform thickness. The four-electrode probes were placed at the periphery of the samples and on measurement, provided the average resistivity of the sample. A current of 2mA was applied to the sample using a Keithley 220 programmable current source. A Keithley 196 sensitive digital voltmeter was used to read the voltage, and a 196 DMM system was used to read the current between two contacts. A Keithley

2001 switch was used to switch between contacts. The meters were connected to a computer and LABVIEW data acquisition system via the IEEE-488 GPIB for automatic data recording. The final properties were calculated using the van der Pauw principle taking into account the sample thickness, the shape factor, and other limitations.

The average resistivity is given by

$$\rho_{avg} = \frac{\rho_a + \rho_b}{2} \quad (11)$$

$$\text{where } \rho_a = \frac{\pi}{\ln \ln 2} f_A t_s \frac{V_1 - V_2 + V_3 - V_4}{4I} \text{ and } \rho_b = \frac{\pi}{\ln \ln 2} f_B t_s \frac{V_5 - V_6 + V_7 - V_8}{4I}$$

Here, ρ_a and ρ_b are resistivity in $\Omega\text{-cm}$, t_s – sample thickness in μm , $V_1 - V_8$ are voltages measured, I is current applied to the sample in Amperes, and f_a and f_b are geometrical factors based on sample symmetry.

Hall mobility is given by

$$\mu = \Delta R * \frac{10^8}{BR_{sh}} \quad (12)$$

where ΔR is the induced change in resistance of the magnetic field B , and R_{sh} is the sheet resistance of the material.

Similarly, resistivity is inversely proportional to the free carrier concentration n and mobility μ , and is given by the relation

$$\rho = \frac{1}{en\mu} \quad (13)$$

4.4.10. High-Temperature Oxygen Sensor Performance

Figure 4.12a represents the schematic representation of sensor setup equipment. The oxygen sensing characteristics of the materials were evaluated using the Al_2O_3 substrate with interdigital electrodes deposited on the surface and the films deposited on top of the electrodes (shown in Figure 4.13a and b). Electrodes were then transferred to the controlled chamber and afterwards placed on a substrate holder. The electrode was connected to two wires by high-temperature silver paste (Ted Pella) and cured for one hour. The sensor performance was evaluated at a temperature of $500\text{ }^\circ\text{C}$; the electrical measurements were recorded using Keithley 6514

electrometer, and the input current (10 nA) was supplied via a Keithley 220 Programmable Current Source. Since the principle behind the sensor is change in resistivity at different partial pressures, Ohm's Law was employed as follows:

$$V=IR \quad (14)$$

where V refers to voltage, I refer to input current, and R refers to the resistance of the film. The resistivity was calculated using

$$\rho = R \frac{A}{l} \quad (15)$$

where ρ is the resistivity, A is the cross-sectional area of electrodes, and l is the distance between interdigital electrodes. The conductivity will be calculated using the equation:

$$\sigma=1/\rho \quad (16)$$

Two gas tanks were employed, namely Ar (baseline gas) and O₂ (analyte gas) of 99.99% purity, to control different partial pressures (pO₂). The gasses were controlled using an MKS mass flow controller to get different partial pressures of oxygen. All the sensor performance responses were recorded as a function of Mo concentration and features such sensitivity and time response are measured. The tests were performed under different partial pressures of oxygen such as 8, 12, 23, 31, and 40 Pa of pO₂ in cyclic periods where pure Ar flow for a constant time was followed by Ar/O₂ flow for the same period.

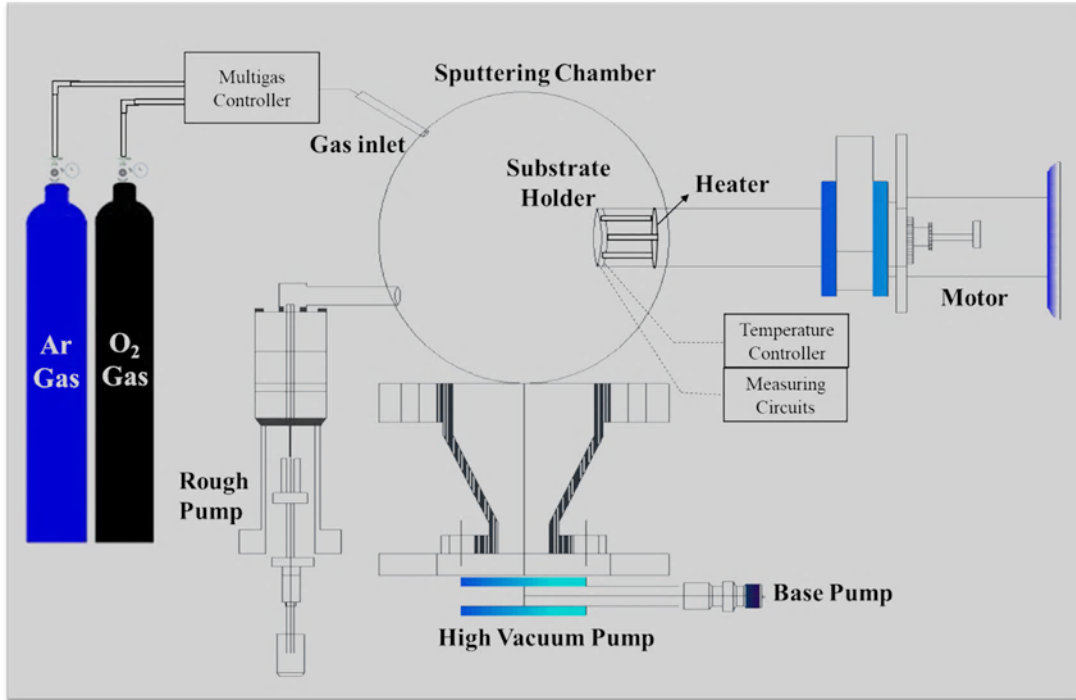


Figure 4.12: Schematic representation of the oxygen sensor setup

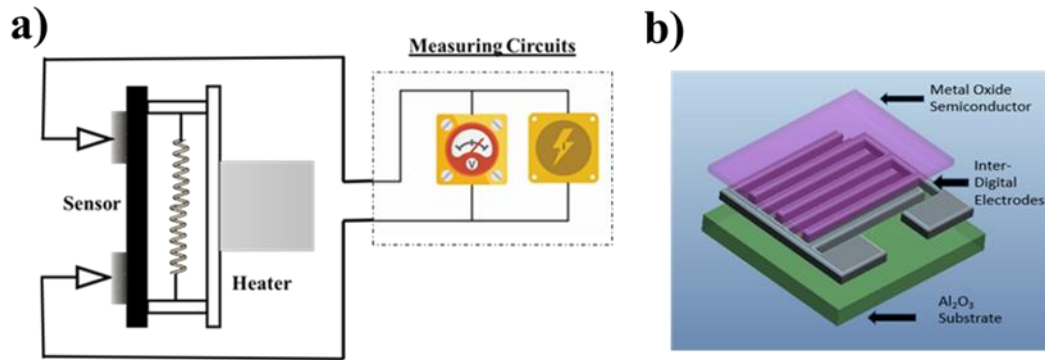


Figure 4.13: Schematic representation a) sample mounting b) sensor sample

Chapter 5: Structural and Mechanical Properties of Intrinsic Gallium Oxide - Nanocrystalline and Amorphous Gallium Oxide Thin Films

Recent developments in surface coating technology, particularly in the production of nanostructured films, have revealed exciting possibilities to control hardness and elastic modulus with some degree of independence, thereby producing wear-resistant surfaces with combinations of properties which were previously unobtainable¹⁰⁴. Current scientific thrust to produce the so-called ‘nanocomposite’ coatings is directed primarily towards the design and development of super-hard or ultra-hard wear-resistant materials¹⁰⁵⁻¹⁰⁷. The performance of these nanocrystalline materials is closely connected to their microstructure and phase, and also depends on the mechanical characteristics to improve the desired properties for a given technological application¹⁰⁸⁻¹⁰⁹. In fact, the designing of materials must combine excellent properties, or comparable to those of the currently used materials, with excellent hardness and elastic modulus, good adhesion, toughness, durability on Si with low interface stresses, which are quite essential for their utilization in extreme environment applications, especially in automotive and coal-based power plant industries¹¹⁰⁻¹¹¹. Under such conditions, it becomes critical to understand how the structural modifications (if any) affect the properties, most importantly the mechanical characteristics which determine their survivability. Therefore, a fundamental understanding of the mechanical characteristics of Ga₂O₃ nanostructures is essential for utilizing them in energy related applications, such as absorber layers in concentrated solar power plants and integrated sensors in oxy-combustion as encountered in engine technologies and coal-based power plants. Under the specific conditions, the materials’ ability and a survivability to sustain sudden impact loads or temperature fluctuations is of major concern¹¹². Thus, a fundamental knowledge and a deeper understanding of the mechanical properties and how these characteristics depend on the microstructure is quite important to effectively utilize Ga₂O₃ under the presence of extreme environment and/or energy related applications. However, unfortunately, while Ga₂O₃ has proven to be a good candidate for such applications, especially those involving exhaust systems of engines

and energy storage and conversion technologies, the efforts to understand the mechanical stability of Ga₂O₃-based nano-materials have been meager. On the other hand, in the context of evolving new hybrid materials based on Ga₂O₃ for energy-related applications as well as new technological applications of Ga₂O₃, a fundamental knowledge of mechanical properties of intrinsic Ga₂O₃ films is quite important. Thus, the primary objective of this work is to fill this knowledge gap by establishing a structure-mechanical property relationship in nanocrystalline and amorphous Ga₂O₃ films. Thus, we have focused our efforts and employed a range of deposition conditions to produce Ga₂O₃ films with variable microstructure. Recent studies suggest that the mechanical properties of Ga₂O₃ in the perfect 2D form, obtained from liquid metals, can provide extraordinary opportunities for enhancing such characteristics^{52, 113}. Furthermore, much of the recent research on nanocomposite super-hard coatings has been focused purely on hardness; however, lately it has been realized that the toughness and plasticity index are important in many of the aforementioned technological applications. Therefore, we performed a comprehensive study in order to understand the interplay between the structure, mechanical properties, and performance of Ga₂O₃ films, which will lead to obtaining strong Ga₂O₃ sheets in the future.

5.1. CRYSTAL STRUCTURE

The GIXRD patterns of Ga₂O₃ films are shown in Figure 5.1 as a function of T_s. The very first characteristic nature that can be noted is the clear variation in the diffraction patterns with increasing T_s. The Ga₂O₃ films deposited at RT exhibit diffuse pattern, which did not show any diffraction peaks, indicating the amorphous nature of the films. The trend continues with an increase in T_s from RT to 500 °C, at which point the presence of diffraction peaks began to appear. The peaks' evolution in the XRD pattern at T_s=500 °C indicates the film crystallization at this temperature. The XRD patterns of Ga₂O₃ films deposited at T_s=500-700 °C correspond to monoclinic β-phase (space group C2/m) with identified peaks ($\bar{2}01$), (400), (002), (111) and ($\bar{2}04$)

at 2θ values of 18.95, 30.05, 31.74, 38.36 and 64.17, respectively, according to JCPDS (00-043-1012)⁵⁰. It can be noted that the (400) peak at $2\theta=30.05^\circ$ exhibits the dominance in intensity for Ga_2O_3 films. The (400) peak evolution with increasing T_s is evident; the intensity of this peak increases while the peak width is reduced. These observations clearly indicate that the T_s strongly influences the growth behavior, and, hence, the structure of Ga_2O_3 films. The amorphous nature of the set of Ga_2O_3 films deposited at $T_s < 500^\circ\text{C}$ can be attributed to the lack of sufficient thermal energy to promote structural order. If T_s is low such that the period of the atomic jump process of adatoms on the substrate surface is very large, the condensed species may stay stuck to the regions where they are landing, thus leading to an amorphous Ga_2O_3 film. The adatom mobility on the surface increases with increasing T_s . The onset of diffraction peaks in XRD indicates that 500°C is the critical temperature to promote the growth of nanocrystalline Ga_2O_3 films. For the given set of experimental conditions, a temperature of 500°C is, therefore, favorable to provide sufficient energy for Ga_2O_3 film crystallization. These results agree with our previous findings, although film thickness is quite high in this work compared to previous studies⁵⁰.

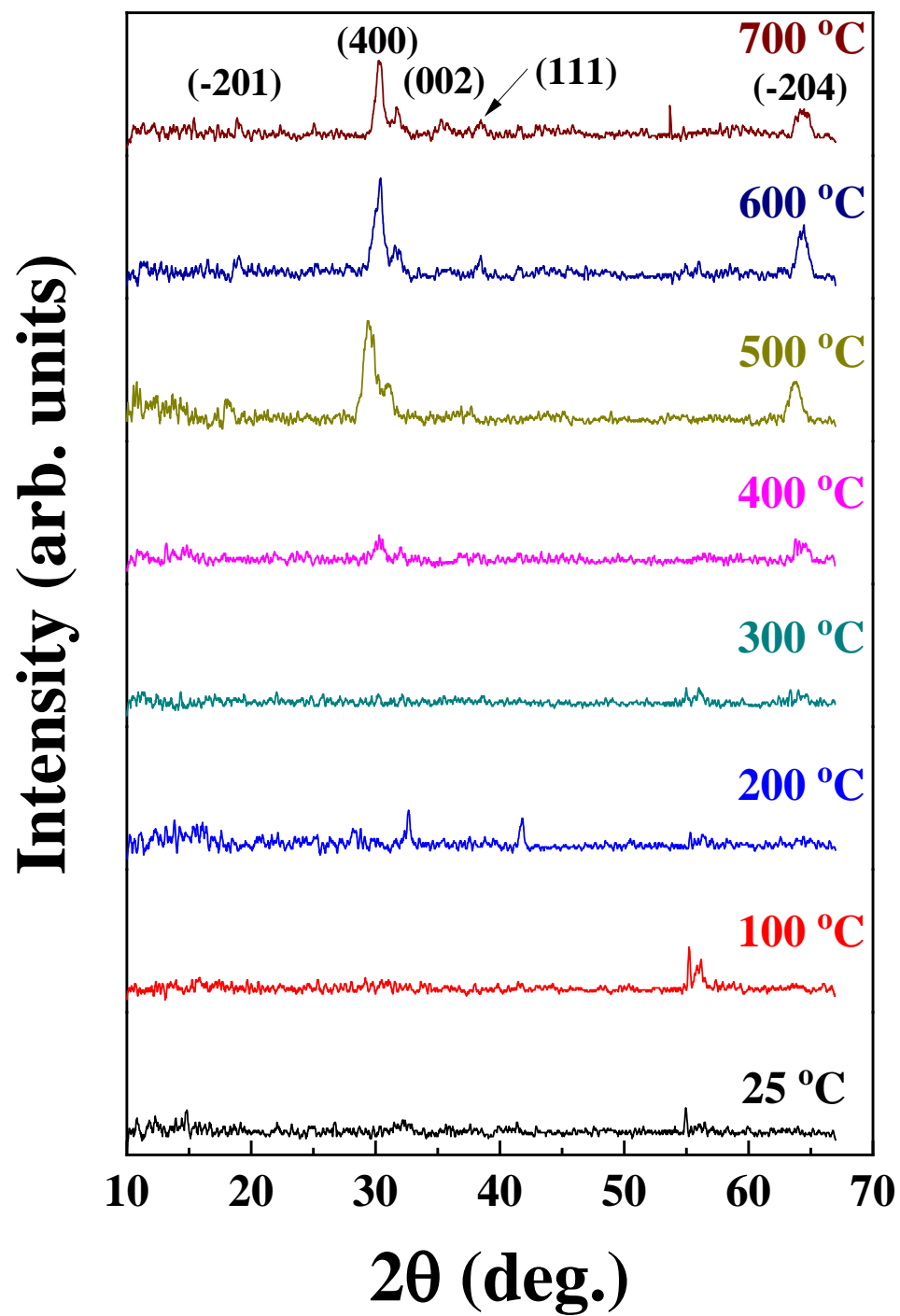


Figure 5.1: X-ray diffraction patterns of Ga₂O₃ films

5.2. SURFACE MORPHOLOGY

The scanning electron microscopy (SEM) images of Ga₂O₃ films are shown in Figure 5.2. The surface morphology is uniform and exhibits different grain structures when increasing the deposition temperatures from RT to 700 °C. The thin films deposited from RT to 300 °C exhibit the presence of particles, but not grown or evolved completely^{88, 114}. By comparing with the XRD spectra, these films could be said to be amorphous. A fine microstructure and uniform distribution of dense particles can be seen in Ga₂O₃ films grown at T_s=500 °C. The dense morphology seen at 500 °C is more or less similar until T_s reaches 700 °C, where the particle size increases further. However, it is evident that Ga₂O₃ films deposited at 700 °C exhibit some porous structure although the average size generally increases with T_s. It should be noted that this trend is general for oxide films and, earlier, the surface morphology variation and other properties improvement was observed for different oxides¹¹⁵⁻¹¹⁸. The average grain size increases from 15 to 35 (±2) nm with increasing T_s.

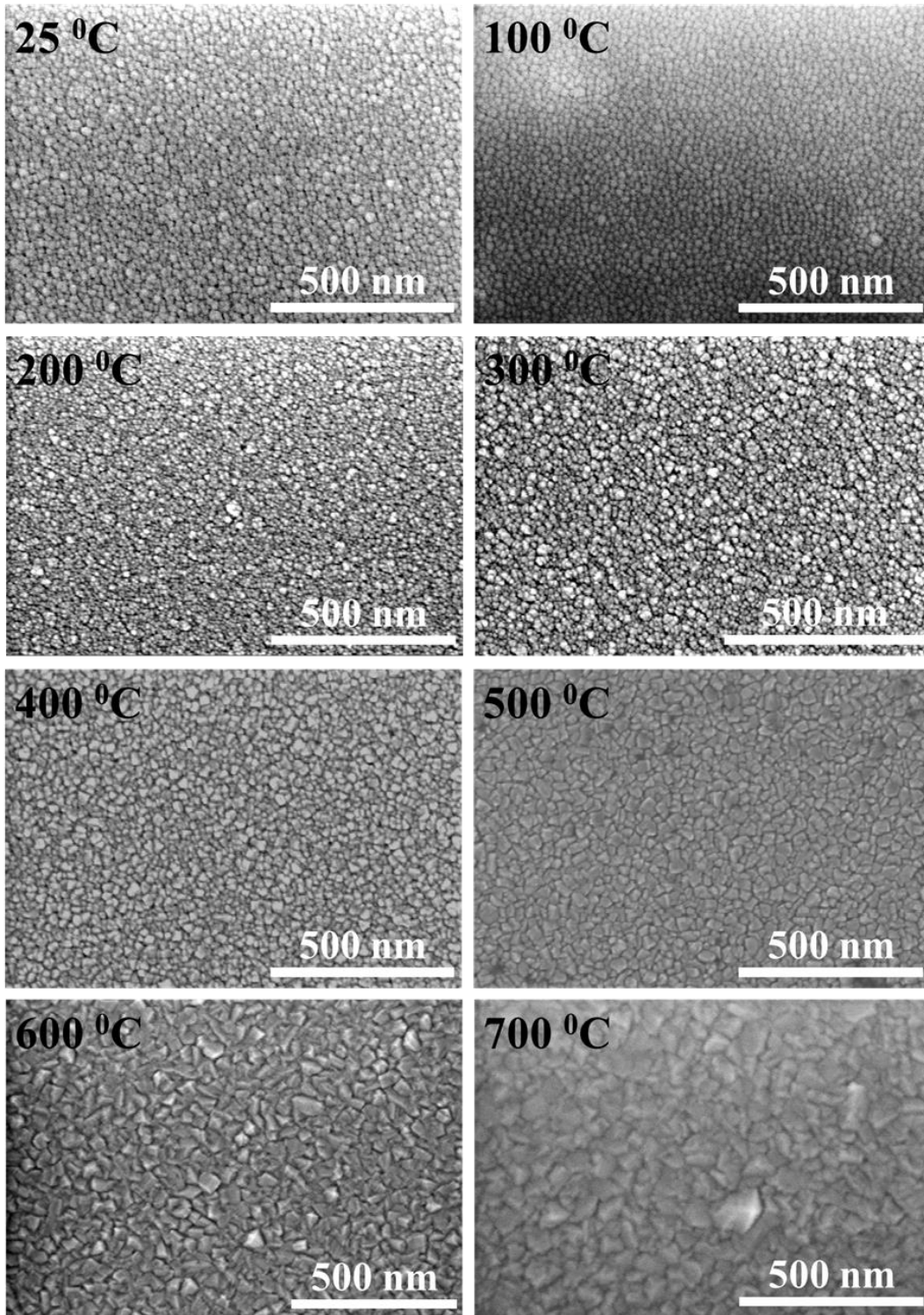


Figure 5.2: SEM images of Ga₂O₃ thin films as a function of T_s

5.3. MECHANICAL PROPERTIES

5.3.1. Indentation Load (L) – Penetration Depth (d) Characteristics

The data of peak indentation load (L) - indentation depth (d) of the Ga₂O₃ films are shown in Figure 5.3. Unfortunately, for thin films, the underlying substrate properties strongly influence the indentation response, and it is difficult to obtain the intrinsic properties of nanocrystalline films^{110, 119}. However, nano-indentation measurements are well known, reliable, and provide a simple and quick method for obtaining information about the mechanical properties of thin films¹¹⁰. The reproducibility is good, but when the ratio of indentation depth to the film thickness (d/t) exceeds a critical value, then the measured mechanical properties are going to be influenced by the substrate material and it is no longer characteristics of the coating^{101, 120}. Therefore, one needs to identify the penetration depth by monitoring the phenomena concerning the indentation load. The critical d/t ratio ~10% is preferred. The results (Figure 5.3) indicate that all the Ga₂O₃ films exhibit the same type of response to indentation load, i.e., an increase in the indentation depth concerning the increasing load. The load was varied from 100 μN to 2000 μN. At the initial load, i.e., at 100 μN, the obtained depth was ~8 to 9 nm for all the Ga₂O₃ films. At 350 μN load, all the Ga₂O₃ films reach the depths ~19-21 nm which is 10% of the total thickness. Beyond this load (10% of the total thickness), the variation in penetration depth can be noted. The penetration depth increases with the increasing indentation load. The variation is ~36 nm for a variation in T_s from RT to 700 °C while the load is constant at 2000 μN. The Ga₂O₃ film deposited at RT had a higher penetration depth, which is ~95±2 nm. The data obtained (Figure 5.3a) indicate that the penetration depth decreases with increase in T_s. This is due to the fact that the measured indenter penetration will be greater in the case of less dense-packed or loosely packed films¹²¹⁻¹²². The penetration depth for Ga₂O₃ films deposited at 500-700 °C is almost the same with the negligible difference of ±2 nm. The penetration depth variation is directly related to the structural evolution of Ga₂O₃ films as a function of T_s. As revealed by the XRD and SEM analyses, Ga₂O₃ films deposited at T_s=RT-400 °C are fully amorphous, while those deposited at T_s=500-700 °C are

nanocrystalline. Therefore, for amorphous Ga₂O₃ films, the surface is no longer stiffer to resist the penetration of indentation, and, hence, the depth is greater. It should also be noted that the fully crystalline films with an excellent packing of atoms are expected to be stiffer and stronger than the films with the less dense packing of atoms. Therefore, the nanocrystalline Ga₂O₃ films deposited at T_s=500-700 °C resist indentation, resulting in the decrease of penetration depth.

The loading and unloading curves are shown in Figure 5.3b, where typical load vs. displacement curves are shown. The data shown are obtained at a constant load of 2000 μN. Three important quantities can be measured from the load vs. displacement curves: the maximum load (P_{max}), maximum displacement (h_{max}) and elastic unloading stiffness (S), i.e., the slope of the upper portion of the unloading curve during the initial stage of unloading. The accuracy of the H and E_r values were dependent on how well these parameters can be measured experimentally. Another important consideration was the final depth (h_f), the indentation depth of penetration after the indenter is fully unloaded¹⁰¹. The load vs displacement curves are different for Ga₂O₃ films deposited under variable T_s. Notably, the slope varies with T_s. Similar to indentation load versus penetration depth characteristics, the slope variation can be attributed to the initial amorphous nature and then to the amorphousness due to the crystalline transformation of the Ga₂O₃ films with increasing T_s. However, all the nanocrystalline Ga₂O₃ films deposited in the range of 500-700 °C exhibit the loading and unloading curves with negligible differences in the slope and penetration depth.

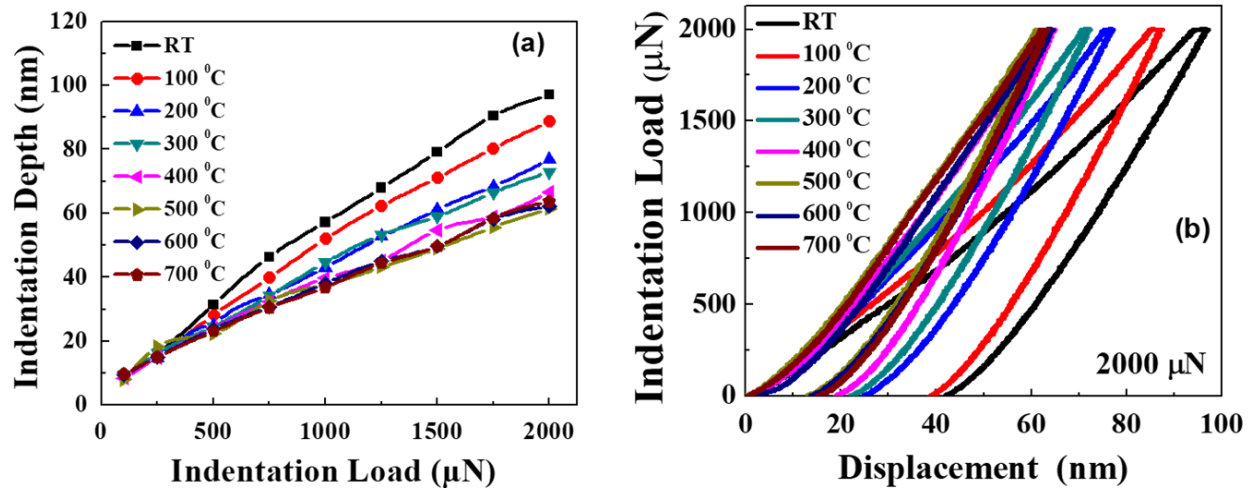


Figure 5.3: (a) Effect of indentation load on the Ga₂O₃ films in terms of indentation depth (b) Load-displacement curves of Ga₂O₃ films obtained at 2000 μN indentation load.

5.3.2. Effect of indentation Load (L) on Hardness (H) and Reduced Elastic Modulus (E_r)

The hardness variation of Ga₂O₃ films as a function of indentation peak load is presented in Figure 5.4a. It can be noted that there is a remarkable difference in H values of Ga₂O₃ films deposited at various T_s. For thin films, the measured hardness varies continuously with the indentation load, penetration depth, film thickness, and the substrate hardness. In the present work, the film thickness and hardness of the substrate were kept constant. Therefore, the variables are indentation load and penetration depth. Theoretically, H values depend on the L and d^{105, 108, 123-124}. In the present case, the data, as well as comparison, indicate that the phenomena are dependent on the crystallinity of the Ga₂O₃ films. It is evident that the H values increase with increasing T_s. This is mainly due to the improved crystalline nature of Ga₂O₃ films with T_s increase, as evidenced by XRD and SEM studies. Note that the hardness is related to the bonding between the atoms and to the ability of the bonds to withstand deformation^{122, 125}. The data follow a similar trend for Ga₂O₃ films deposited at T_s=25-100 °C, and then H values increase slightly for Ga₂O₃ films deposited at T_s=200-400 °C. Therefore, these films have a similar trend and there was a noticeable difference. Finally, for T_s=500-700 °C, the data show a similar trend with a negligible difference between the values. This negligible difference is mainly due to the grain size refinement. For these films, the

hardness increases until the critical load $350 \mu\text{N}$, at which point hardness decreases slightly and remains constant with minimum variations. This phenomenon is mainly due to substrate effects. In practice, in indentation experiments, penetration depth has to be maximum of 10% of the total film thickness to avoid the substrate effects. Thus, both the L-d and H-L relationships are in corroboration with the observed differences in terms of structural changes of Ga_2O_3 films. The E_r variation with load in Ga_2O_3 films is shown in Figure 5.4b, where similar behavior is also noted in E_r data. The E_r values gradually decrease with increasing load. Also, E_r value increases with increasing T_s . Thus, the decreasing E_r is due to structural transformation; E_r values of an amorphous material are usually lower than its crystalline counterpart because of less dense packing¹¹².

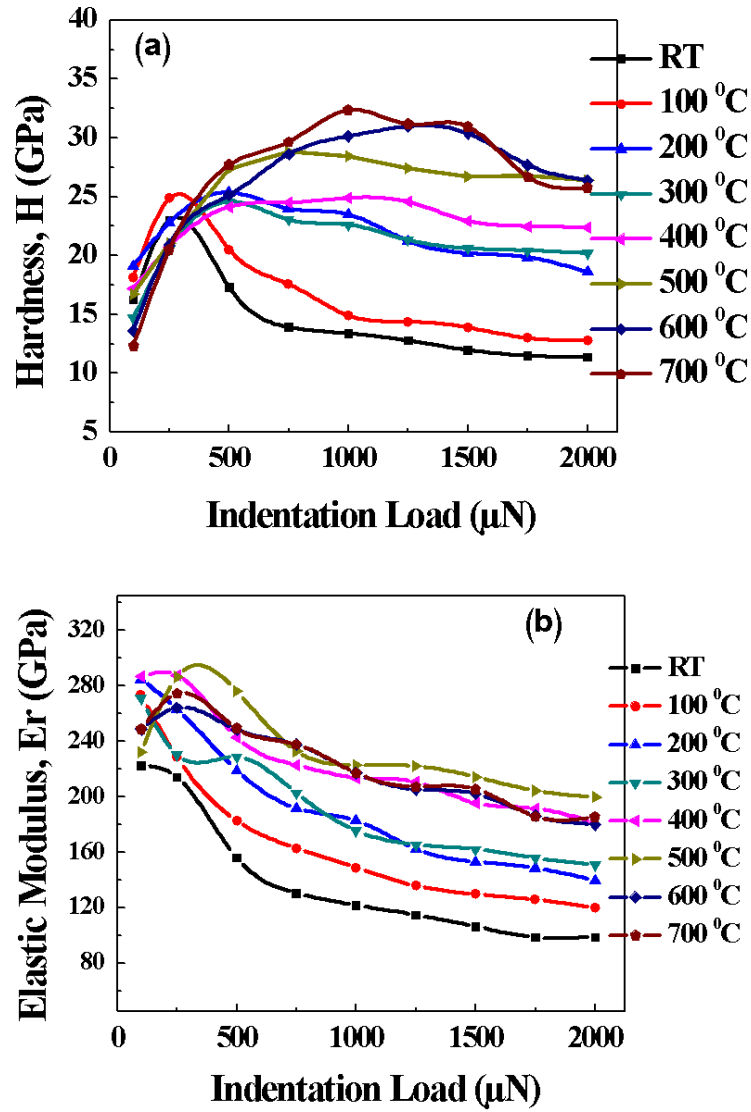


Figure 5.4: (a) Effect of indentation load on H; (b) Effect of indentation load on E_r.

5.3.3. H and E_r at Critical Load

To obtain reasonable and reliable H and E_r values, the penetration depth where substrate-induced effects can be safely neglected is important. The evaluation of loading and unloading curves for the Ga₂O₃ films at 350 μN, is shown in Figure 5.5. At 350 μN indentation load, there was an optimum displacement between the loading and unloading curves. The obtained penetration depth was ~20 nm, which is almost 10% of the total thickness. By considering the above reasons, as well as those discussed in previous sections, we can conclude that the optimum load was 350

μN , where we can get the accurate H and E_r results. The mechanical properties of the Ga_2O_3 films deposited at $500\text{ }^\circ\text{C}$ is investigated first to establish the baseline properties. This is also for the other reason that, according to XRD and SEM analyzes, the realization of nanocrystalline $\beta\text{-Ga}_2\text{O}_3$ films occurs at $T_s=500\text{ }^\circ\text{C}$. The H and E_r data of Ga_2O_3 films are shown in Figure 5.5. It is evident that the T_s and structural evolution significantly influence the mechanical characteristics of Ga_2O_3 films. The influence of the grain size on mechanical properties (H and E_r) is complex since the grain boundaries may either act as obstacles to dislocation slip (strengthening effect) or provide a positive contribution to the deformation of the material (softening effect)^{106, 126}. As a result, the H values gradually increased from 17 to 27 GPa for the Ga_2O_3 films with increasing T_s from RT to $500\text{ }^\circ\text{C}$ and then remained more or less constant with further increase in T_s to $700\text{ }^\circ\text{C}$. However, the hardness of Ga_2O_3 films deposited at $700\text{ }^\circ\text{C}$ slightly decreased compared to that obtained for the film deposited at $500\text{ }^\circ\text{C}$. Similarly, E_r values also increase from ~ 210 to 290 GPa. The H and E_r characteristics follow almost a similar trend (Figure 5.5). The observed variation and differences in the mechanical characteristics of Ga_2O_3 films can be explained as follows. Nanocrystalline materials, due to their nano-sized grains and high density of interfaces, show high strength and hardness, and also many other interesting properties¹²¹. Therefore, the higher values of H and E_r observed are, undoubtedly, due to the texturing and interface microstructure of the nanocrystalline, granular Ga_2O_3 films. These parameters (E_r and H) are intrinsic mechanical properties of a material dominated by the strength and chemical bonds between constituent atoms^{124, 127-128}. It is well known that the improvement in the strength of materials is due to its grain refinement. The role of grain boundaries is enhanced significantly with the reduction in grain size^{106, 127, 129}. Thus, the E_r value of an amorphous material is usually lower than its crystalline counterpart because of less dense packing. Therefore, we believe and conclude that the observed changes in mechanical properties are mainly due to the microstructure changes in Ga_2O_3 films.

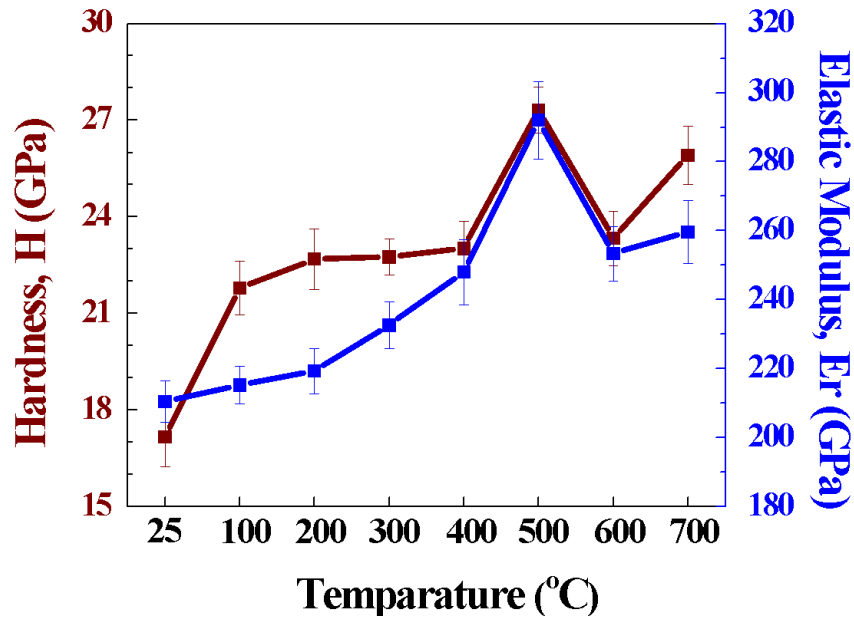


Figure 5.5: Hardness and elastic modulus of Ga₂O₃ films.

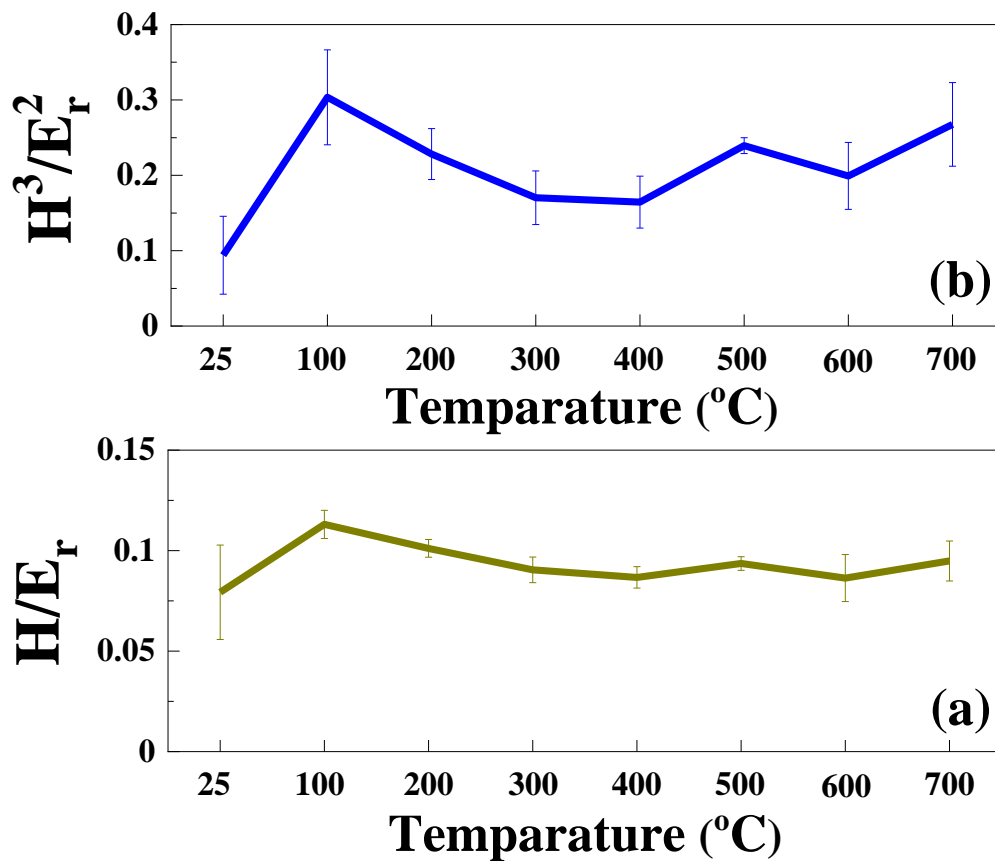
5.3.4. Significance of H/E_r and H^3/E_r^2

In recent years, just hardness is considered to be the primary requirement for wear resistance. In addition to H, elasticity and toughness are also regarded as important factors¹⁰⁴. Therefore, combined analysis and consideration of H/E_r and H^3/E_r^2 along with H and E_r has been proposed as a realistic means to derive a better understanding of the mechanical behavior of nanomaterials, especially nano-composite thin films and coatings¹³⁰. From the measured values of H and E_r , H/E_r and H^3/E_r^2 can be calculated. The H/E_r and H^3/E_r^2 data of Ga₂O₃ films is presented in Figure 5.6. The ratio between H and E_r is referred to as the plasticity index (sometimes it is also indicated as coating durability)^{104-105, 110, 131}, and it is widely accepted as a valuable measurement for determining the limit of elastic behavior of the thin films. This ratio is important to avoid wear. The term H^3/E_r^2 should be a reliable indicator of a coating's resistance to plastic deformation and is referred to as toughness¹⁰¹. In this case, the two parameters' (H/E_r and H^3/E_r^2) values and their trends will be helpful for the clear understanding of the intrinsic Ga₂O₃ films' mechanical behavior, especially for their integration in high-temperature sensors to be operated under extreme

environments¹³². The data obtained for Ga₂O₃ films (Figure 5.6a) indicate that most of the films exhibit $H/E_r \leq 0.1$. Note that the Ga₂O₃ films deposited are ceramics; therefore, H/E_r ratio is expected to be less than 0.1¹²⁰. The H/E_r ratio for the nano-crystalline Ga₂O₃ films is 0.085 ± 0.05 and almost constant. The H^3/E_r^2 data for Ga₂O₃ films are presented in Figure 5.6b. The H^3/E_r^2 data exhibit a similar trend to that noted for H/E_r . The values are in the range of ~ 0.1 - 0.3 GPa. The H^3/E_r^2 values gradually increased from 0.17 to 0.24 ± 1 GPa for the crystalline Ga₂O₃ films. This is due to the variation in the grain size of these films, as explained in the previous section. Ga₂O₃ films deposited at 500 °C exhibited the highest value of H^3/E_r^2 , which were $\sim 0.23 \pm 0.01$. The H^3/E_r^2 ratio is the indication of the coating's resistance to plastic deformation. Therefore, the higher the ratio, the higher the resistance to deformation^{104, 110}. Therefore, the H/E_r and H^3/E_r^2 indicate that Ga₂O₃ films deposited at 500 °C with a characteristic nano-crystalline and dense morphology exhibit the highest deformation resistance or toughness.

We believe that the superior mechanical characteristics of nanocrystalline Ga₂O₃ films are derived from the interconnected network of densely packed, smaller crystallites. Thus, a simple model can be formulated to explain the observed functional relationship between the mechanical characteristics (H and E_r) and structure in nanocrystalline Ga₂O₃ films. Evident from the results, the H , E_r , H/E_r , and H^3/E_r^2 depend on the structural quality and grain size. XRD and SEM results evidenced that Ga₂O₃ films deposited at RT are completely amorphous. In fact, all the films deposited at $T_s < 500$ °C are amorphous. It is, therefore, reasonable to attribute the observed low mechanical quality or lower values of H , E_r , H/E_r , and H^3/E_r^2 to a very low packing density in the Ga₂O₃ films. These films, which are characterized by a structural disorder, may be causing a decrease in mechanical characteristics. However, the initial improvement or increase in H , E_r , H/E_r , and H^3/E_r^2 values when Ga₂O₃ films were deposited within the range of 300-400 °C is due to a slight improvement in the structure but still mostly the amorphous structure is dominating. However, the structural transformation from amorphous-crystalline Ga₂O₃, as noted in XRD and SEM measurements, enhances the mechanical characteristics. Therefore, we believe that improved structural order results in the formation of a dense network of nanocrystals leading to an

enhancement in the packing density. This characteristic change in structure results in the observed enhancement in H , E_r , H/E_r , and H^3/E_r^2 . Furthermore, in nanocrystalline Ga_2O_3 films, the nanostructure is characterized by dense, randomly oriented nanocrystals¹³⁰. Musil et al. have defined the parameter (H^3/E_r^2) as the resistance to plastic deformation and demonstrated a general, linear relationship between H^3/E_r^2 and H for many coatings for mechanical and tribological applications¹³³⁻¹³⁴. Furthermore, using nano-indentation and nano-scratch testing, Beake et al.¹⁰⁸ have also demonstrated such a linear relationship in TiN/Si_3N_4 composites. Therefore, an attempt has been made in this work to examine the H^3/E_r^2 versus H relationship. The variation of H^3/E_r^2 with H for the Ga_2O_3 films is shown in Figure 5.6c, where it can be seen that the data fit approximately to a linear relationship. Perhaps the nanocrystalline Ga_2O_3 films may be equivalent to a composite structure under nanocrystallites embedded in a slightly porous structure.



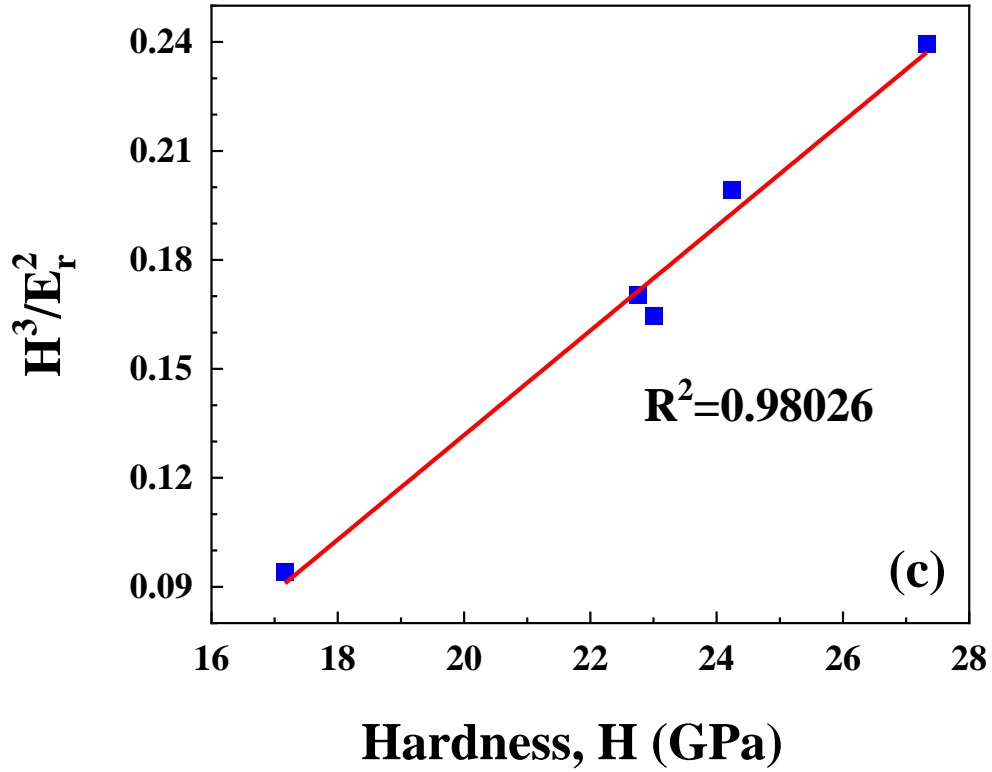


Figure 5.6: The effect of T_s on: (a) H/E_r and (b) H^3/E_r^2 values. (c) Linear relationship between H^3/E_r^2 and H as noted in Ga_2O_3 films.

5.3.5. Strain-Rate Experiments at Specific Indentation Load

Further examination of the mechanical characteristics is evaluated by indentation strain rate, also called an equivalent strain rate. Mayo and Nix¹³⁵ developed a nano-indentation method for the determination of strain rate sensitivity (SRS) on a submicron level by controlling the loading rate^{5, 135}. The indentation strain rate was determined from the depth–time data for a given range of indentation depth. According to Mayo and Nix, the indentation strain rate can be derived from the concept of true strain. Approximating the specimen length by the indentation depth and assuming the hardness to be independent of the indentation depth, this can be estimated as¹³⁵⁻¹³⁸:

$$m_{\text{nano-indentation}} = \frac{d(\ln \ln H)}{d(\ln \ln \dot{\epsilon})} \quad (17)$$

where m is the SRS exponent, which describes the SRS behavior of the material assuming a constant microstructure, and $\dot{\epsilon}$ is the quantity

$$\dot{\epsilon} = \frac{1}{2} \frac{\dot{P}}{p} \quad (18)$$

where \dot{P} is the loading rate and P is the applied maximum load; in other words, $\dot{\epsilon}$ is the ratio of the indenter displacement velocity to the plastic depth.

Loading rates and equivalent strain rates are directly proportional to each other, as can be seen from the equation above. The hardness variation with equivalent strain rate for Ga₂O₃ films is shown in Figure 5.7. To evaluate the strain rate dependence of the hardness, seven different indentation strain rates (0.05, 0.07, 0.10, 0.16, 0.25, 0.50, and 1.00 s⁻¹) were applied during the nanoindentation. The average H values measured at different strain rates were performed at specific load conditions, i.e., 350 μN. The trend clearly shows a distinct and experimentally detectable effect of indentation strain rates. For Ga₂O₃ films deposited at RT, the H values continuously decrease due to the amorphous nature. However, the nanocrystalline Ga₂O₃ films show negligible change. The strain rate sensitivity (m) is the resistance of the material to prevent necking during the deformation of a material¹³⁹⁻¹⁴⁰. The measured m values were 0.017, 0.013, 0.011, 0.013 for RT, 100 °C, 300 °C, 500 °C, and 700 °C, respectively. It can be observed clearly that the substrate temperature, and, hence, the microstructure, significantly influence the strain rate sensitivity of the Ga₂O₃ films.

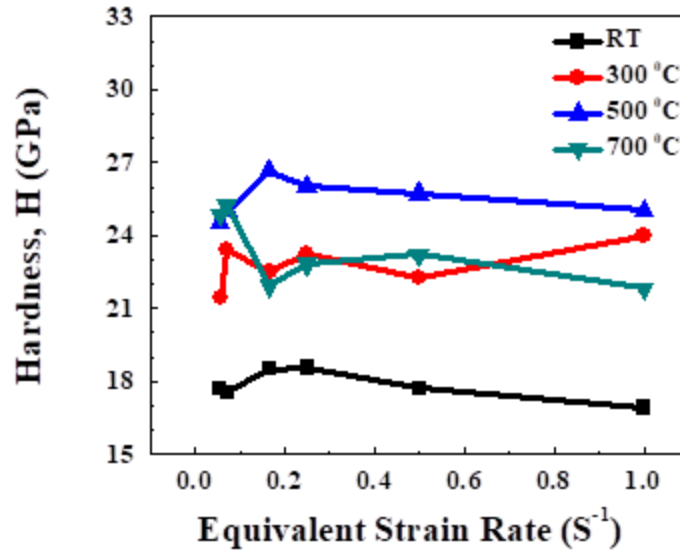


Figure 5.7: Variation of hardness with equivalent strain rates at a constant load of 350 μN .

5.3.6. Adhesion and Interfacial Bonding – Scratch Testing

Scratch resistance is one of the most critical parameters required for thin film coatings, such as automotive topcoats, floor coatings, and optical components^{123, 141-142}. Because most of the coatings encounter a wide range of mechanical stresses during their working lifetime, a scratch test is one of the most prominent and widely accepted methods to evaluate the adhesion strength between the thin, hard coatings and substrates¹⁴³⁻¹⁴⁴. The depth profiles and scratch test results of Ga_2O_3 films are presented in Figures 5.8 and 5.9, respectively. The data reveal that the Ga_2O_3 films deposited at 500 °C exhibit the best interfacial bonding in terms of depth profile, i.e., 67 nm after the performance of the scratch test (Figure 5.8). The scratch test was performed in such a way that, when the cohesive failure occurs, the area around the scratch deforms while the rest of the film remains undamaged^{105, 145}. It is important to recognize that the nanocrystalline Ga_2O_3 films do not exhibit any delamination other than pile up deformation. The depth profiles (Figure 5.8) show the cross-section of the films at the maximum applied force along the scratch. The negative scratch depth means that the indenter is located above the initial sample surface, and positive depth indicates the indenter is moved below the initial surface. The nano-scratch was performed in

ramping mode, where the normal force is increasing along with the scratch X-direction. The lateral force applied on the tip by deforming material could also be used to determine plastic properties of the films. However, it was determined that a cross-section profile of the scratch when 8000 μN force is applied better demonstrated the deformation mechanisms. Evidently, the depth profile cross-sections obtained at the maximum 8000 μN force exhibits that the scratch depth was continuously decreasing with increasing crystallinity. This behavior matches with the H behavior shown in Figure 5.9. The depth profiles were almost constant for the films with minimal variation, i.e., all the films lay between 67 and 74 nm, which follows the H^3/E_r^2 trend. As discussed, the H^3/E_r^2 ratio is proportional to the coating resistance to plastic deformation, which indicates that the higher the ratio, the higher the deformation resistance. Also, it should be noted that nano-scratch (Figure 5.9) tests showed material pile-up, but no evidence of channel cracking or delamination of the films was observed.

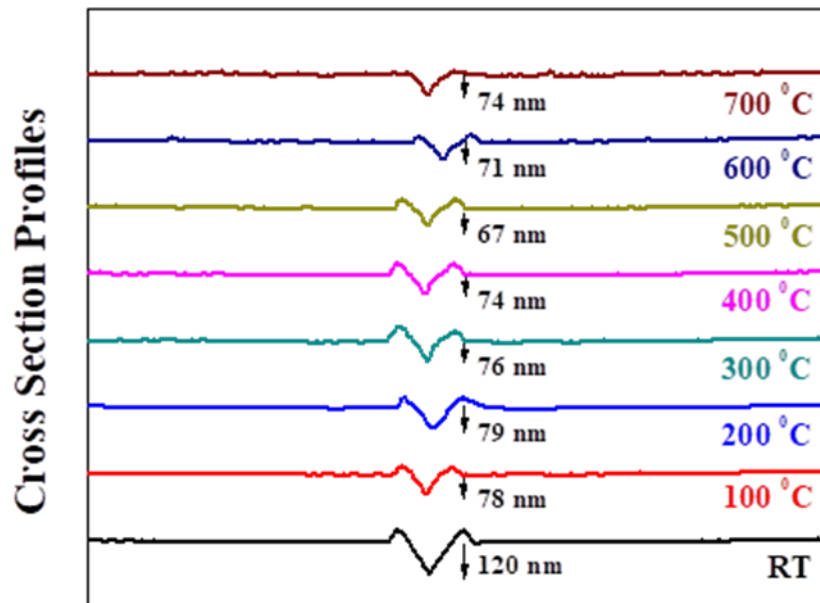


Figure 5.8: Scratch testing profiles of Ga_2O_3 thin films. Depth profiles for Ga_2O_3 thin films deposited at various T_s are shown.

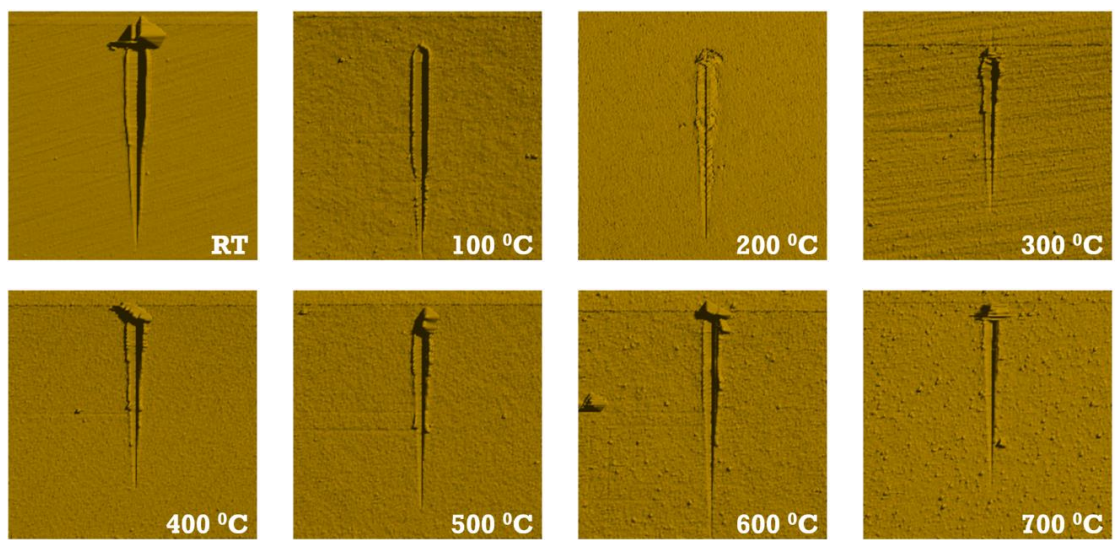


Figure 5.9: Scratch testing data of Ga_2O_3 films. Surface images after scratch test are shown.

Chapter 6: Molybdenum Incorporated Ga₂O₃ Nanocrystalline Thin Films – Structure, Morphology and Chemical Analysis

6.1. Structural Analysis-Crystal Structure Properties (XRD)

The GIXRD patterns of Mo-incorporated Ga-oxide films are presented in Figure 6.1. For comparison, the XRD curve of intrinsic Ga₂O₃ films is also included. The appearance of the diffraction peak intensity of GMO-0, i.e., without any Mo incorporation, in the XRD pattern indicates the formation of nanocrystalline β -Ga₂O₃. The GIXRD patterns of Mo-doped Ga₂O₃ films as a function of applied sputtering power to the Mo-target indicates the significant effect of Mo on the crystal structure. The GIXRD pattern of intrinsic Ga₂O₃ corresponds to monoclinic β -phase (space group C2/m) with peaks (-201), (400), (002), and (-204) at corresponding 2θ values of 18.95, 30.05, 31.74, and 64.17, respectively¹⁴⁶, according to JCPDS (00-043-1012). The evolution of these peaks showed an interesting trend as a function of Mo-incorporation in the Ga₂O₃ nanocrystalline films. The very first characteristic feature that can be noted is the dominance of the (400) peak at $2\theta=30.05^\circ$ for intrinsic Ga₂O₃ films. The intensity of this peak is seen to diminish at the very first Mo-doping into Ga-oxide while still maintaining the overall structural order in the films. Further increase in the sputtering power to the Mo target at ≥ 40 W, i.e., Mo content higher than 4 at%, introduces structural changes in Ga₂O₃ as is evident from GIXRD patterns. Mo incorporation suppresses the peak intensity, which eventually disappears at ≥ 40 W, i.e., Mo content higher than 4 at%. This observation indicates the Mo-induced amorphization of the GMO films with increasing Mo content. Thus, the XRD results suggest that increasing Mo content to ~ 4 at% and above induces complete amorphous characteristic nature in the GMO films.

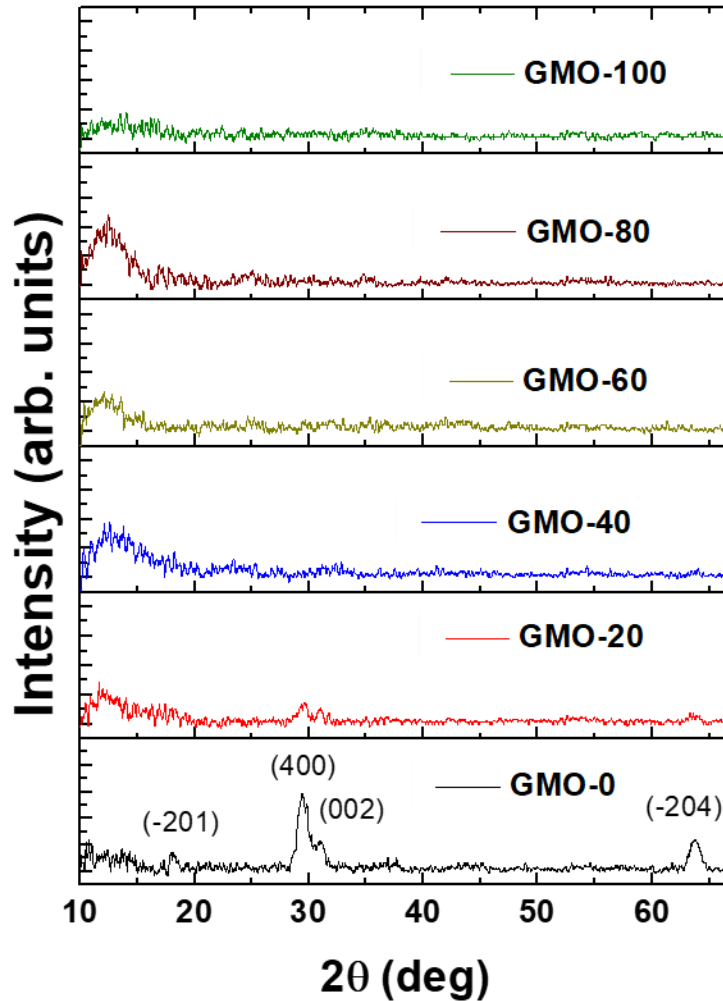


Figure 6.1: GIXRD patterns of GMO samples. The structural evolution as a function of Mo content is evident.

6.2. Morphology Analysis - Scanning Electron Microscopy (SEM)

The SEM images indicating the characteristic surface morphology of the GMO films are shown in Figure 6.2. It can be noted that the intrinsic Ga_2O_3 films exhibit uniform grains. Dense packing arrangement and well-resolved grain boundaries can also be seen in the pure Ga_2O_3 films as well as in films deposited with sputtering power applied to Mo target at ≤ 40 W. As revealed by structural characterization, the nano-size grains are fully crystalline. Molybdenum incorporation induces interesting morphology changes. For a small amount of Mo, the changes are negligible. GMO films still exhibit the grain structure as well as the partial crystalline structure as is evident

in XRD studies. However, with further increase in Mo, the grain morphology disappears completely. These SEM observations thus corroborate the XRD data indicating the crystalline-to-amorphous transformation of GMO film surfaces.

The observed growth behavior, crystal structure variation, and surface morphology evolution in nanocrystalline GMO films can be explained based on the combined effect of thermodynamic parameters and Mo-incorporation. In general, the growth of either single or multicomponent oxide films with a single/complex phase resulting from physical vapor deposition is influenced by the growth temperature, which is an important thermodynamic parameter^{115, 147}. Thus, since other parameters are kept constant, deposition temperature and Mo content are the two factors that play a key role in deciding the structural chemistry as well as properties of Ga-Mo-O films resulting from vapor-transport deposition. As reported elsewhere and demonstrated in this work, 500 °C is optimum to produce β -Ga₂O₃ films³¹. However, the Mo-incorporation induced structural changes in the growth behavior of Ga-Mo-O films are reflected in XRD patterns of GMO films (Figure 6.1). The small size grains in electron imaging analysis coupled with the presence of well-resolved peaks in XRD indicate the structural order retained and formation of the nanocrystalline β -Ga₂O₃ phase in GMO films deposited with relatively low Mo content. However, due to the absence of diffraction peaks in XRD patterns and surfaces becoming smooth with disappearance of granular morphology in SEM, it can be concluded that the films are completely amorphous for increasing Mo content to 4 at% and above. Such Mo-induced effects were also noted in Mo incorporated WO₃, where higher deposition temperatures were required to obtain nanocrystalline samples of W-Mo-O compared to pure WO₃ films due to the effect of Mo doping¹⁴⁷. Furthermore, the disordering effect or amorphization due to metal-doping into WO₃, where the dopant prevents the crystallization and leads to the amorphous nature, is also noted in

the Ti-doped Ga_2O_3 films³¹. Thus, the amorphous nature of GMO films is primarily due to the effect of Mo incorporation, which prevents the crystallization or induces changes in the energetics so that the growth kinetics are dependent on the amount of Mo content in the formation of GMO film matrix.

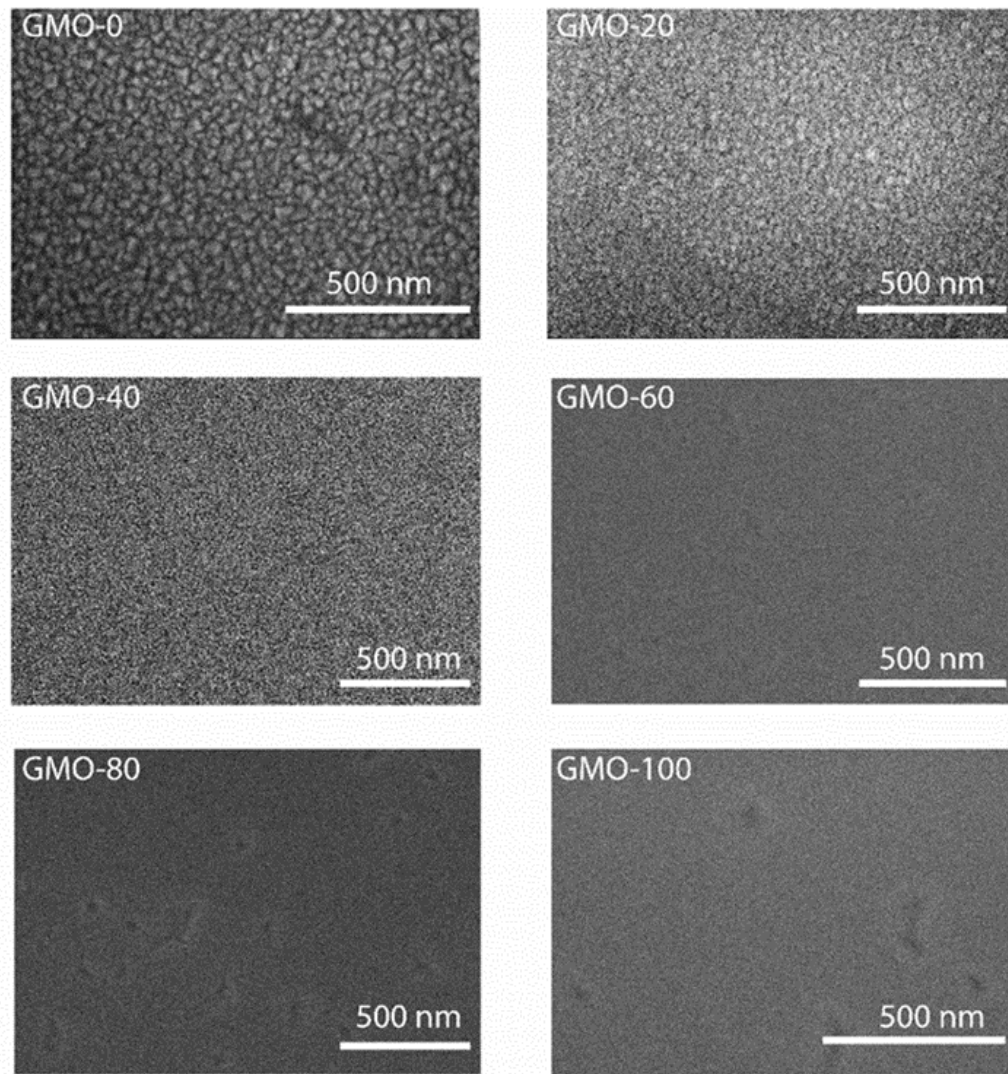


Figure 6.2: SEM images of GMO films. The effect of Mo on the morphology evolution of GMO films is evident.

The cross-sectional microscopy images are represented in Figure 6.3, showing the interfaces of GMO films deposited on Si by varying the Mo content at constant deposition time of 3 hrs. A clear trend could be noticed in increasing the thickness from GMO-0 to GMO-100, the interfacial SiO₂ layer could be easily noticeable for GMO-0 and GMO-40 samples, whereas for the films GMO-60 onwards there is no sign of a SiO₂ interface layer. The thickness was calculated using the ImageJ software package for these cross-sectional images. The thicknesses were approximately 180 nm, 240 nm, 325 nm, 366 nm, 380 nm for GMO-0, 40, 60, 80, and 100, respectively. In this, the deposition time was kept constant; varying Mo target sputtering power is the only variable, and with increasing power the Mo content increased, and, as a result, the thickness increased.

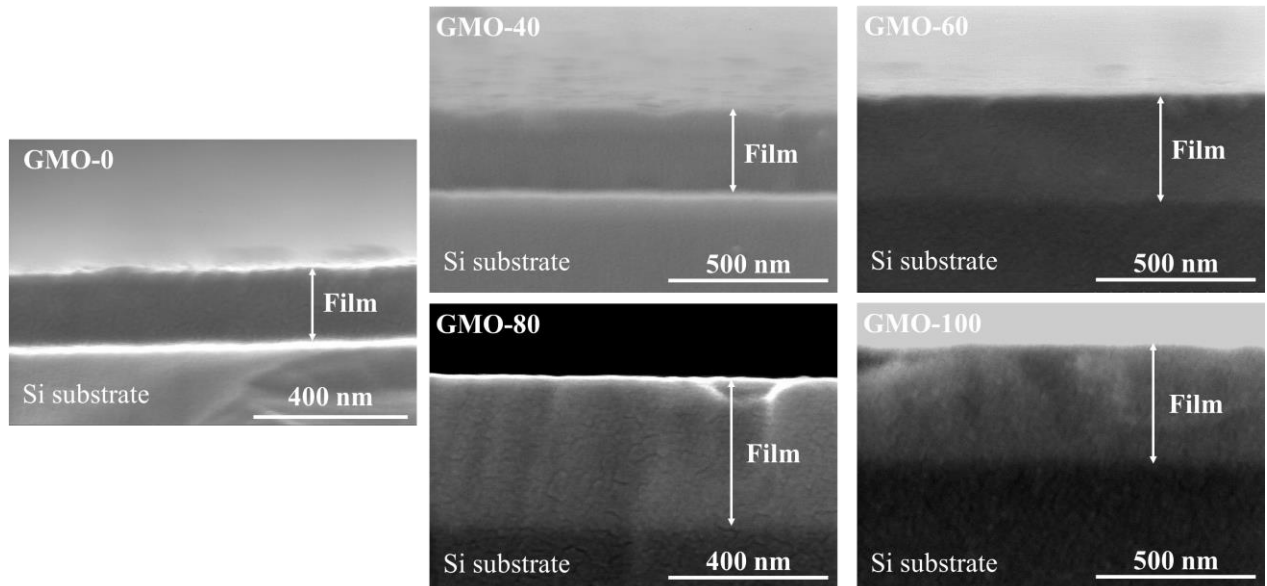


Figure 6.3: SEM cross-section data of GMO films.

6.3. Chemical Analysis - X-Ray Photoelectron Spectroscopy (XPS)

Surface chemical analyses using XPS provide us additional information on the surface and interfacial chemical changes. We present the XPS survey spectra of GMO films in Figure 6.4. The spectra show that Ga, Mo, and O are the main constituents of the deposited films. The presence of C 1s is clear in the survey spectra. The carbon peak in the XPS spectra is because of adventitious carbon from exposure to air following fabrication and/or before being placed in the XPS system. Therefore, the spectra were calibrated to C 1s peak at a binding energy (BE) of 284.6 eV. The absence of a Si substrate peak is because the deposited Ga-oxide films cover the Si surface and are sufficiently thick to prevent detection of photoelectrons originating from the substrate. The XPS measurements allow us to determine chemical valence states of the constituent ions present in the GMO samples. To determine the chemical states of the metal ions presented in the films upon a detailed analysis of the core level spectra of the main constituents was performed. High-resolution scans were performed for Ga 3*d*, Mo 3*d*, and O 1s and analyzed to get their chemical states and the interaction between individual metal ions and oxygen.

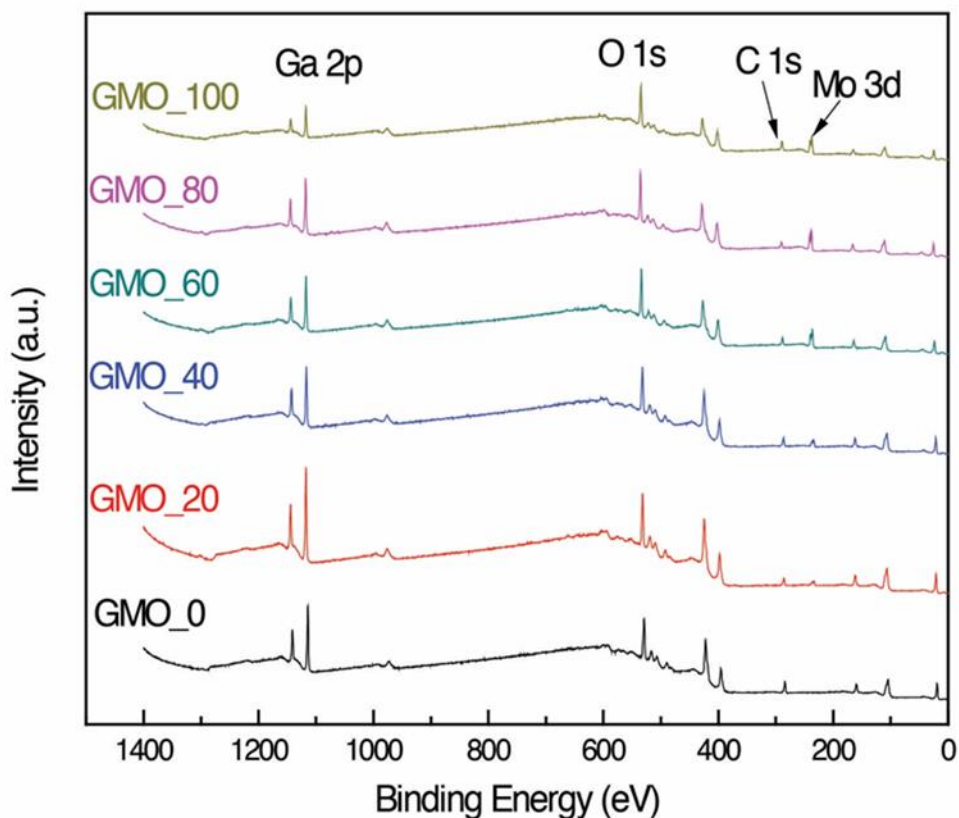


Figure 6.4: XPS survey scan for GMO films

The core-level XPS spectra of the Ga $3d$ region are shown in Figure 6.5a. The data shown are for samples with a variable Mo content. It can be seen that the Ga $3d$ peak is located at a binding energy (BE) of ~ 20.5 eV. The intrinsic Ga_2O_3 films (without Mo) show Ga $3d$ peak at 20.5 eV characterizing the Ga^{+6} state of Ga ions. In bulk Ga_2O_3 crystal, this Ga $3d$ peak appears at 20.6 eV. Thus, the BE location of Ga $3d$ peak at ~ 20.5 eV accounts for the Ga–O bonds, where Ga ions exist in their highest oxidation state, i.e., Ga^{+6} . Also, no significant effect is seen in G $3d$ peak shape or BE position with variable Mo content. These observations indicate that irrespective of the Mo content incorporated into Ga-oxide, the structural chemistry and chemical valence state of Ga ions are highly stable.

The high-resolution XPS spectra of O $1s$ core level are displayed in Figure 6.5b. It can be seen that the O $1s$ spectra exhibit rather broader nature with the presence of a wide shoulder on the higher BE side. However, the O $1s$ core level of GMO-0 samples, i.e., intrinsic Ga-oxide films

without Mo, exhibit symmetrical nature and narrower compared to those samples with Mo incorporated. As a result of the fitting, the dominant component, which is reasonable for oxide crystals, is positioned at a BE of 530.63 eV for GMO-0 (without Mo). The shoulder is effectively described by a minor intensity component at a BE of 532.15 eV, which corresponds to oxygen bonded to carbon. This component usually presents on the oxide film surfaces due to carbon chemisorbed from the atmosphere. The intensity of the minor component is very low in reference to the total intensity of O 1s peak. Therefore, the component at 530.63 eV is attributed to crystal bulk oxygen for Ga₂O₃, and the component at 532.15 eV is related to absorbed species. The other component, i.e., de-convoluted peak, located at BE~531.5 eV, is attributed to Mo oxides. The evolution of this component is interesting as can be seen in the spectra (Figure 6.5b) with increasing Mo content.

The detailed XPS spectra of Mo 3d region of the GMO samples are shown in Figure 6.5c. The intrinsic Ga-oxide samples didn't show any Mo contribution. While the peak intensity is not appreciable for samples with low Mo content (GMO-20 and GMO-40), the intensity of Mo 3d peak increases with increasing sputtering power to the Mo-target, i.e., Mo content in the films. The spectra can show the appreciable intensity for GMO films when Mo incorporated is ≥ 4 at%. The intrinsic Ga-oxide samples without any Mo didn't show any sign of Mo contribution in the XPS (not shown). It is evident that the Mo 3d doublet (due to spin-orbit splitting; $j=5/2$ and $j=3/2$) are resolved with a spin-orbit splitting energy separation, $\Delta E(\text{Mo } 3d)$, of 3.19 eV. Both the Mo 3d_{5/2} and Mo 3d_{3/2} peaks show a weak but pronounced shoulder contribution from the lower BE side. Therefore, the component analysis was performed by considering the peak as a superposition of two doublets shifted in energy but with the same intensity ratio of the components and spin-orbit splitting. A most notable feature is the fact that the evolved Mo 3d scan is rather broad in nature, indicating the presence of Mo ions existing in multiple valence states^{115, 148-151}. Note that the Mo chemistry is complex due to its ability to take chemical valence states ranging from 2+ to 6+. The peak-fitting procedure confirms that the Mo ions exist in Mo⁶⁺, Mo⁵⁺, and Mo⁴⁺ states in the GMO films upon thermal annealing. However, as evident from spectra shown in Figure 6.5c, the specific

valence state(s) is/are dependent on the amount of Mo incorporated in GMO films. The peak-fitting procedure indicates that the Mo $3d_{5/2}$ component dominant in intensity is positioned at a BE of 232.51 eV and minor intensity component is located at BE=231.17 eV. MoO_3 is an insulator, and the severe charging effect is observed for this compound under X-ray illumination. The energy shifts due to surface charging would be accounted in reference of C 1s core level of adventitious hydrocarbons but the binding energy of this core level is different in different XPS spectrometers, and the respectively systematic error appeared in element-binding energy determination. This error source results in noticeable scatter of binding energy values of representative element core levels reported in the literature for the same crystal. To avoid this effect, in our opinion the using of a difference of element-binding energies is more reasonable for a compound characterization, and higher robustness of this method has been recently demonstrated in several studies. Therefore, the binding energy difference $\Delta = (\text{O } 1s - \text{Mo } 3d_{5/2})$ is a suitable parameter to evaluate the valence state of Mo ions in the films studied. Such deeper analysis of Mo $3d$ spectral region and comparison with literature in the present case of GMO films indicates that the possibilities in GMO films are MoO_3 , MoO_x , and Mo_4O_{11} . Quite interestingly, upon thermal annealing or under as-deposited conditions, GMO films with Mo content ≤ 4 at% (set of films up to GMO-40) exhibit a well-resolved doublet, which can be assigned only to MoO_3 without any ambiguity. Also, the formation of MoO_3 occurs and without any components related sub-oxides of Mo (MoO_x). We believe that the absence of Mo sub-oxides for Mo ≤ 4 at% under the set of a given thermodynamic conditions employed is due to the ability of Mo to oxidize under the presence of thermal energy coupled with oxygen present in the atmosphere.

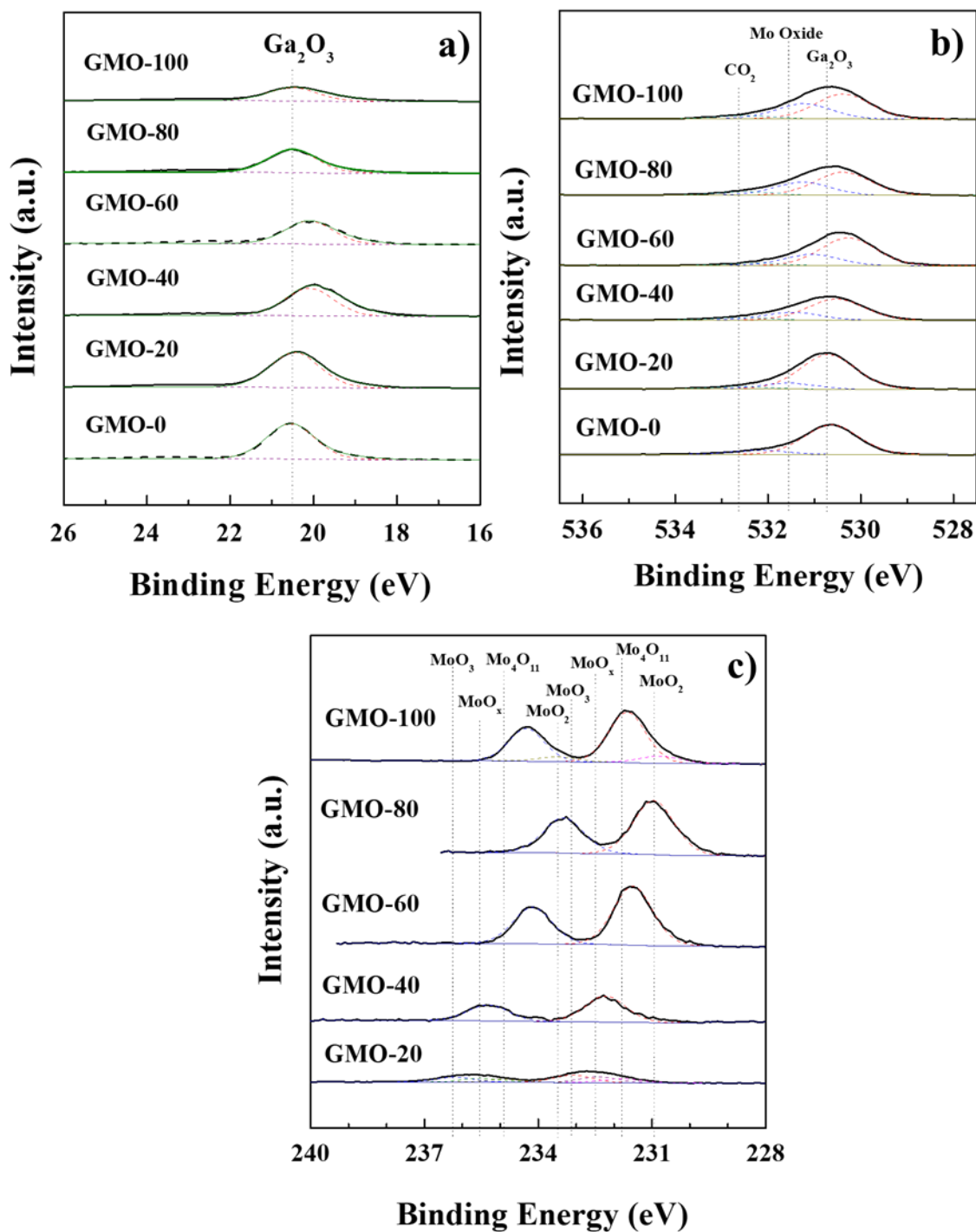


Figure 6.5: High-resolution XPS data of Ga, O, and Mo core level peaks in GMO films deposited at variable Mo concentration. a) Ga 3d high-resolution XPS spectra. b) O 1s high-resolution XPS spectra. c) Mo 3d core-level XPS spectra

However, X-ray photoelectron spectroscopy measurements also allow determining the atomic percentage of Mo as shown in Figure 6.6. It is evident that the Mo content increases with

increasing sputtering power. Increasing the sputtering power from 0 to 100 W increases the Mo content from 0 to ~11.23 at%. As can be seen from Figure 1, the amount of Mo incorporated into GMO was low for sputtering power of 60 W, at which point the amount of Mo increases considerably. This can be understood from the fact that the sputtering yield from the Mo target can be appreciable only when optimum cathode power is applied. It appears that 60 W is optimum to incorporate a reasonably good amount of Mo leading to the formation of GMO films.

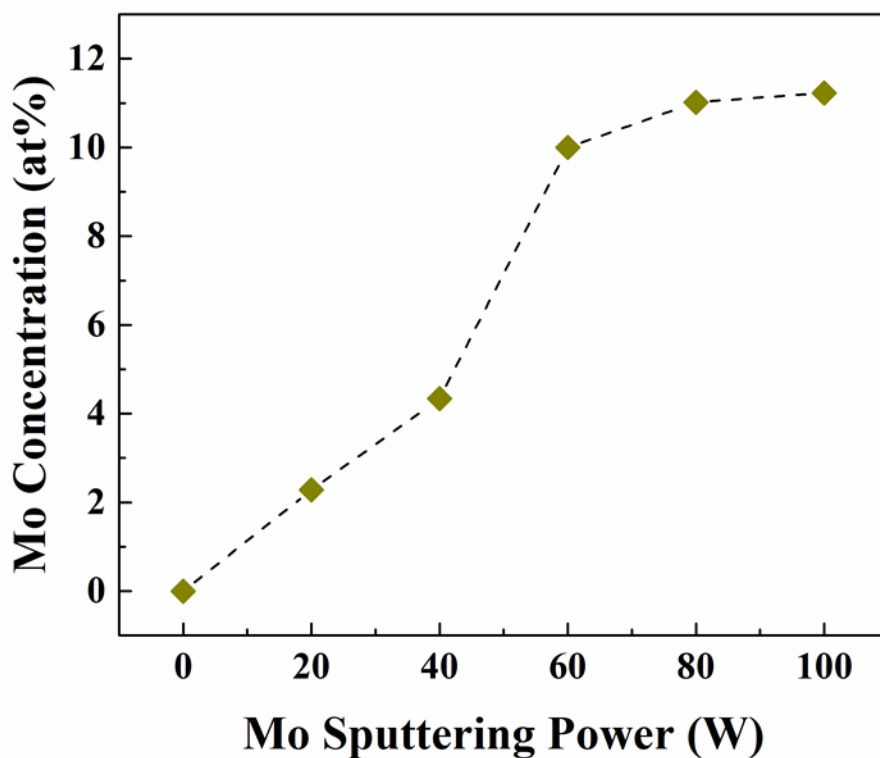


Figure 6.6: concentration of Mo as a function of Mo target sputtering power

6.4. Chemical Analysis - Rutherford Backscattering Spectrometry (RBS)

The bulk of the film (along with the depth to the substrate) chemistry and interface chemical stability were probed using Rutherford Backscattering Spectroscopy (RBS). The RBS data of GMO samples are shown in Figure 6.7. The backscattered ions scattered from various elements present in the sample areas are indicated at their respective energy position in Figure 6.7.

Mo is the heaviest among all the elements present either in the film or the substrate. Therefore, the ion scattering from Mo atoms occurs at higher energy (Figure 6.7). As indicated, the step edge and peaks due to ion backscattering from Ga, Si (substrate), and O atoms (film) are observed at 625, 320, and 280 channel number, respectively. The simulation curve (circles) calculated for a film agrees with the experimental curve for a sample composition of Mo doped Ga_2O_3 films. The perfect fit of GMO-60 experimental data can only be achieved by adding hydrogen in the film section which suggests the presence of porosity from RBS data.

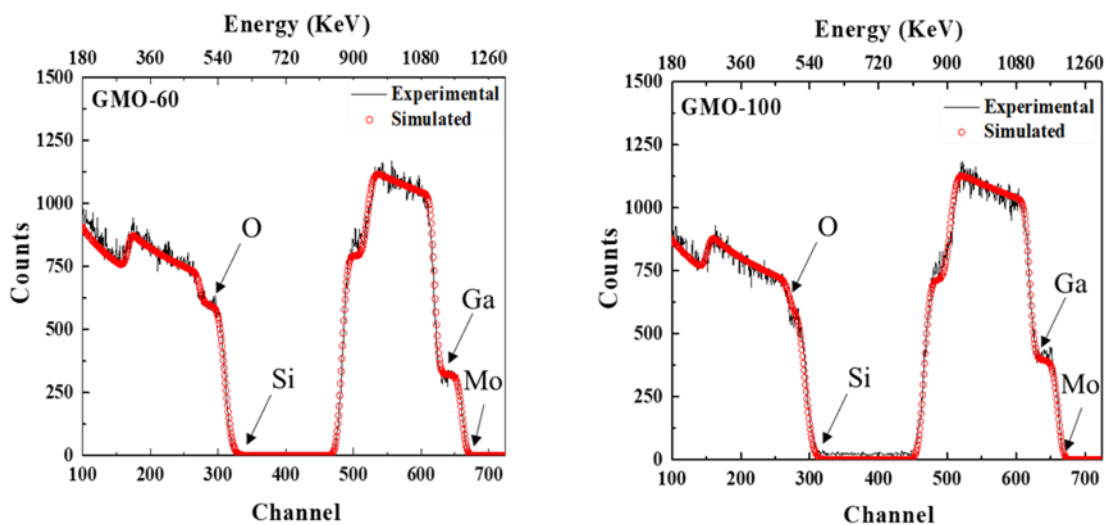


Figure 6.7: RBS data for GMO films, deposited under variable Mo concentration (experimental curves (circles) and SIMRA simulated curves (lines)).

Chapter 7: Molybdenum Incorporation Ga₂O₃ Nanocrystalline Thin Films – Mechanical Properties

7.1 Nano-Mechanical Analysis - Nanoindentation

7.1.1. Indentation Load (L) - Penetration Depth (d) Characteristics

To determine the optimum and reliable H and E_r values, optimizing the penetration depth and indentation load is critical. The data of peak indentation load - indentation depth relationship of the GMO films are shown in Figure 7.1. The results indicate that all the GMO films exhibit the same type of response to indentation load, i.e., an increase in the indentation depth with respect to the increasing load. The load was varied from 100 μN to 2000 μN. At the initial load i.e., at 100 μN, the obtained penetration depth was ~8 nm for GMO-0 films, whereas for Mo incorporation, the penetration depth is seen to decrease slightly but continuously with increasing Mo content. This trend is continued up to a load of 350 μN load, where the penetration depth is almost constant (~20 nm) for all the films. After this critical load, the penetration depth is seen to increase rapidly with further increase in the load from 350 μN to 2000 μN for those films with higher Mo content. While the film surfaces are expected to be harder with Mo, the observed trend of penetration depth increase with increasing Mo content can be attributed mainly to the Mo-induced surface structural modification. Initial incorporation of Mo did not change the crystal structure of the GMO films as seen in XRD studies; therefore, the net result is that there was an opposing force for indenter penetration into the film. That could be the reason why the intrinsic Ga₂O₃ films as well as GMO films deposited with relatively low sputtering power to the Mo target exhibit the lower penetration depth. However, increasing Mo content induces the crystalline-to-amorphous structural modification as noted in XRD and SEM studies. As such, the GMO films' surfaces are no longer stiffer to offer resistance to the penetration and increases the penetration depth with increasing Mo

content. It should be noted that the nanocrystalline films or fully crystalline films are expected to be stiffer and stronger than the amorphous films^{101, 121, 130, 152}. Therefore, there was no opposing reaction to indentation load and hence the penetration depth was more in amorphous materials than those observed in crystalline materials^{110, 121, 132, 153}.

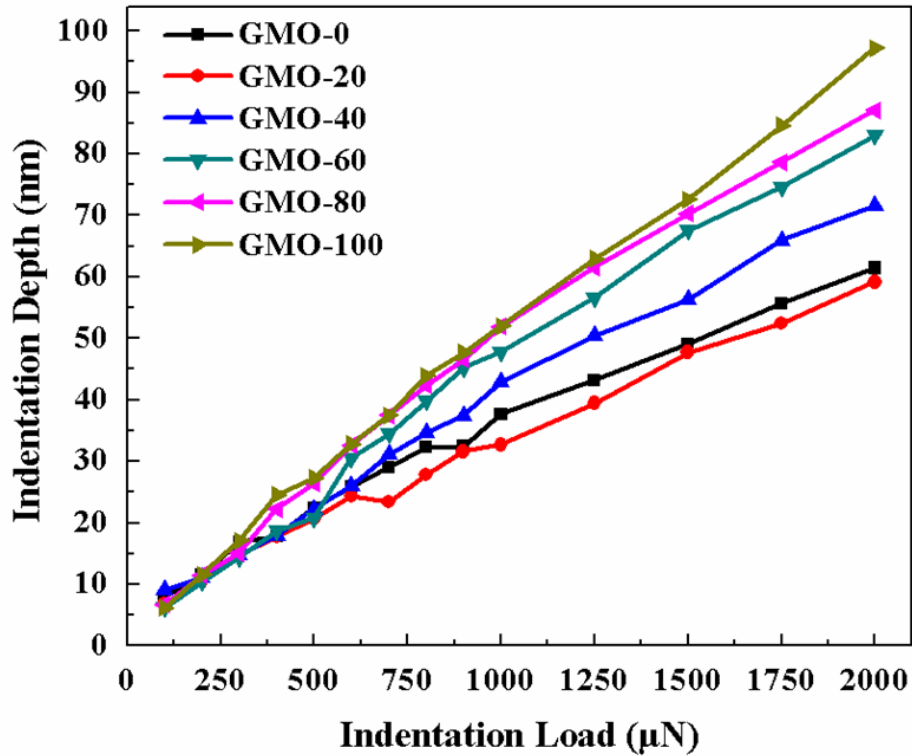


Figure 7.1: Effect of indentation load on the GMO films in terms of indentation depth.

7.1.2. Effect of Indentation Load (L) on Hardness (H) and Reduced Elastic Modulus (E_r)

The hardness variation of GMO films as a function of indentation peak load is presented in Figure 7.2a. The data, as well as a comparison, indicates that the GMO-0 and GMO-20 films present a similar behavior with different H values, although the H values of Mo incorporated samples are higher. This is mainly due to the crystalline nature of these films as evidenced by XRD studies. Note that the hardness is related to the bonding between the atoms and to the ability of the bonds to withstand deformation^{121, 154-155}. In fact, the same behavior is also noted in the load vs.

depth analysis (Figure 7.1). For GMO-0 and GMO-20 films, the hardness increases until the critical load 350 μN , at which point it starts decreasing slightly and remaining constant with minimum variations. This phenomenon is mainly due to substrate effects¹⁴⁷. In practice, in indentation experiments, penetration depth has to be maximum 10% of the total film thickness to avoid the substrate effects^{101, 104}. On the other hand, GMO samples with increasing Mo content also present the same type of behavior, i.e., increasing H values with load and starts decreasing continuously. Thus, both the L-d and H-L relationships are in corroboration with the observed differences in terms of structural changes, which are mainly crystalline versus amorphous nature of the films due to Mo incorporation. Hardness and crystallographic structure relationships are well established for crystalline materials. However, it is not the case for amorphous materials^{152, 156}. The E_r variation with load in GMO films is shown in Figure 7.2b. GMO films exhibit similar behavior. The E_r values gradually decrease with increasing load. Also, increasing Mo content decreases E_r values. This is because the films become amorphous with Mo incorporation. Thus, the decreasing E_r is due to structural transformation; E_r values of an amorphous material is usually lower than its crystalline counterpart because of less dense packing^{26, 121, 156-158}.

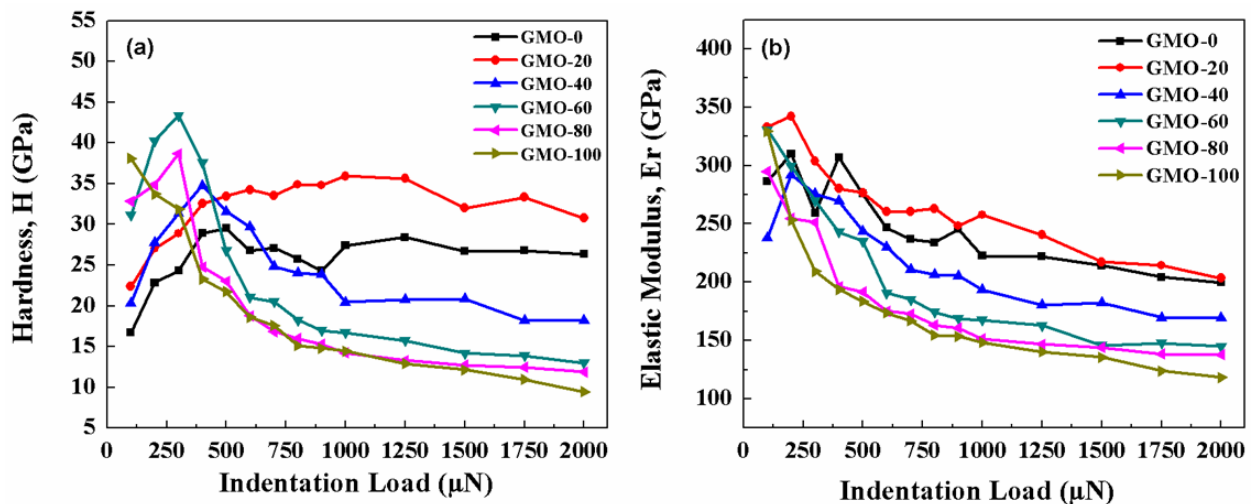


Figure 7.2: (a) Effect of indentation load on H; (b) Effect of indentation load on E_r

7.1.3. H and E_r at Critical Load

To obtain reasonable and reliable H and E_r values, the penetration depth where substrate-induced effects can be safely neglected is important. In general, 10% of the total thickness of the sample surface is acceptable to avoid the substrate effects while calculating the reliable H and E_r values of the coatings. As explained in earlier sections (load vs. depth), the critical load 350 μN is found to be optimum where the depth (~20 nm) is more or less equal to 10% of the total thickness. Therefore, this load was considered determining reliable H and E_r values. The evolution of H and E_r with the Mo content is shown in Figure 7.3. It is evident that the Mo incorporation into Ga-oxide significantly affects the mechanical characteristics. The H value increases from ~27 to 36 GPa for Mo content increase from 2 to 10 at%. However, a further increase in Mo content decreases the H value to ~30 GPa, whereas at the same time the E_r value is seen to decrease from 295 to 210 GPa continuously. Note that the elastic modulus is an intrinsic property and fundamentally related to atomic bonding^{147, 159}. The E_r value of an amorphous material is usually lower than the crystalline material. It is due to the arrangement of atoms and density. The amorphous material had less dense packing of atoms^{104, 159}. Therefore, we believe and conclude that the observed changes in mechanical properties are mainly due to Mo induced chemical and structural changes in the GMO films.

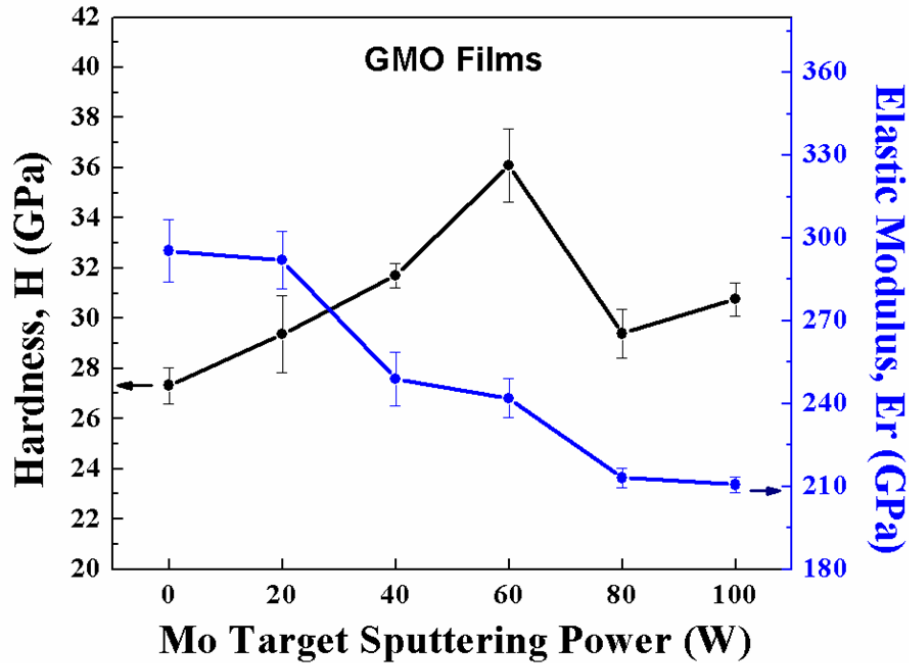


Figure 7.3: Hardness and reduced elastic modulus of GMO films

7.1.4. Significance of H/E_r

The mechanical behavior of a film/coating is not only strongly dependent on the combination of H and E_r but also the ratio of H to E_r , which is usually called the plasticity index. The concept of plasticity index is widely used in determining the limit of elastic behavior for the films^{18, 160}. In this case, the index will be helpful to understand the wear resistance of these GMO films, especially for their integration in high-temperature sensors to be operated under extreme environments. The obtained H/E_r ratio data and H^3/E_r^2 values for GMO films are presented in Figure 7.4. Careful observation of the data reveals that the trend is similar to that seen in H values which indicate that H/E_r and H^3/E_r^2 the ratio is dependent on the hardness of the sample. Usually, a high value of H/E_r (>0.1) exhibits high elastic recovery or high wear resistance¹⁴⁷. However, only Mo incorporated films exhibit H/E_r ratio >0.1 , while for intrinsic Ga-oxide H/E_r is <0.1 . These values can be understood as follows. The gallium oxide film is a ceramic, which is brittle in nature. Furthermore, Musil et al. have defined the parameter (H^3/E_r^2) as the resistance to plastic

deformation and demonstrated a general, linear relationship between H^3/E_r^2 and H for many coatings for mechanical and tribology applications¹³⁰. Incorporation of a refractory metal into the ceramic matrix is generally expected to improve the index as seen in the case of GMO films. Continuous increase in Mo induces the amorphous nature which accounts for the slight decrease in index values for higher Mo. However, the relatively higher H/E_r values upon Mo incorporation can be treated as an indication of excellent wear resistance of the films.

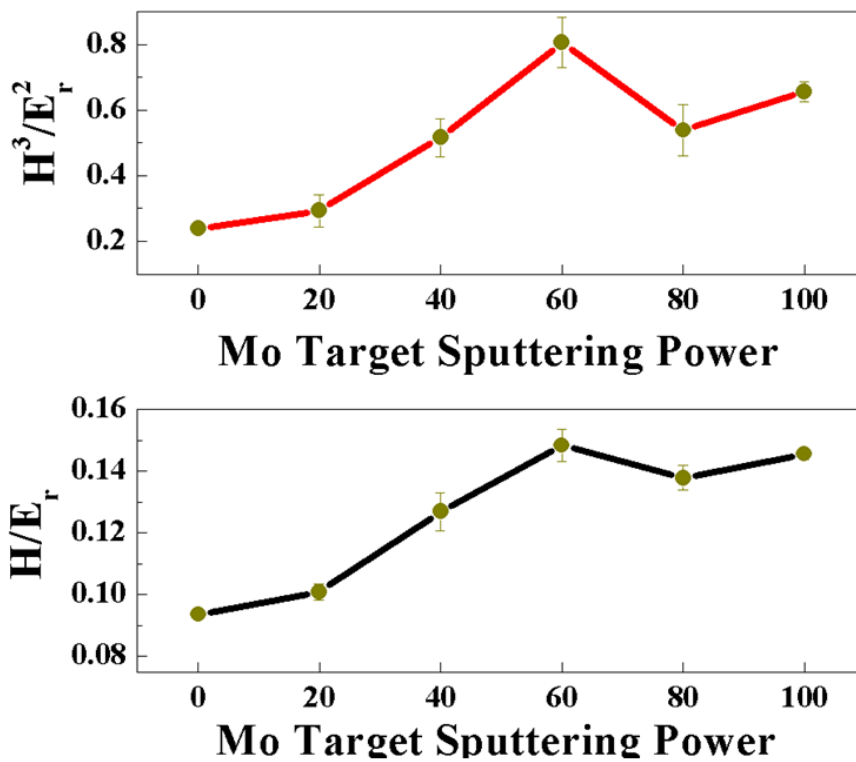


Figure 7.4: Effect of Mo-target sputtering power on H/E_r and H^3/E_r^2 values

7.2. Nano-Mechanical Analysis - Nanoscratch

Adhesion between the film/coating and the substrate is a critical parameter to estimate the life and film quality^{53, 143-144, 161-163}. Scratch testing is one of the most prominent and widely acceptable methods to evaluate the adhesion strength between film and substrate, durability, and functionality of the film. The adhesion strength of the GMO films was calculated. Poor adhesion

leads to early delamination of the film. The scratch testing procedure and depth profiles on GMO samples are shown in Figure 7.5 and 7.6. The data reveal that the GMO-0 films exhibit the interfacial bonding in terms of depth profile, i.e., 67 nm after the performance of the scratch test (Figure 7.6). The scratch test was performed in such a way that, when the cohesive failure occurs, the area around the scratch deforms while the rest of the film remains undamaged. It is important to recognize that the GMO films do not exhibit any delamination other than pile up deformation. The depth (Figure 7.6) profiles show the cross-section of the films at the maximum applied force along with the scratch. The negative scratch depth means that the indenter is located above the initial sample surface, and positive depth indicates the indenter is moved below the initial surface. The nano-scratch was performed in ramping mode, where the normal force is increasing along with the scratch X-direction. The lateral force applied on the tip by deforming material could also be used to determine the plastic properties of the films. However, it was determined that a cross-section profile of the scratch when 8000 μN force is applied better demonstrated the deformation mechanisms. Evidently, the depth profile cross-sections obtained at the maximum 8000 μN force exhibits that the scratch depth was continuously decreasing with increasing crystallinity. This behavior matches with the H behavior shown in Figure 6.10. Also, it should be noted that nano-scratch (Figure 7.5) tests showed material pile-up, but no evidence of channel cracking or delamination of the films was observed.

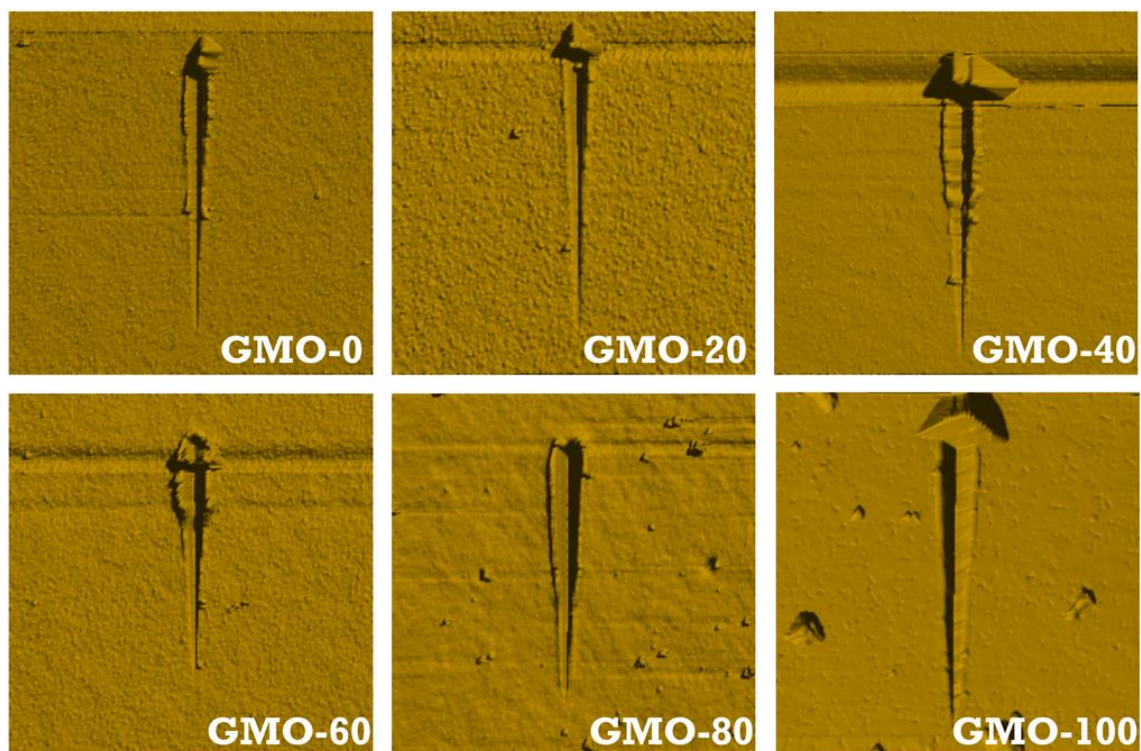


Figure 7.5: Scratch test performance on Ga-Mo films

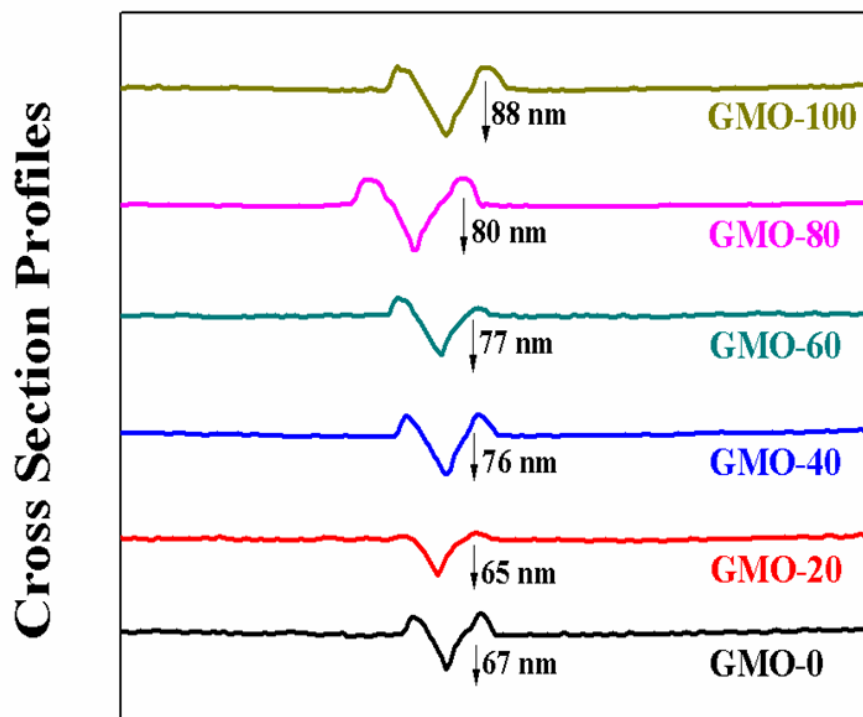


Figure 7.6: Scratch testing profiles of GMO thin films. Depth profiles for GMO thin films deposited at various Mo at% are shown

Chapter 8: Molybdenum Incorporated Ga₂O₃ Nanocrystalline Thin Films – Optical Properties

8.1. Optical Analysis-Ellipsometry

The refractive index (n) and extinction coefficient (k) of the thin films were fitted with a Tauc-Lorentz dispersion model, which proved successful in determining the optical properties of the GMO films. This model was chosen both for transparency in respective wavelength regions for GMO films and for providing a successful fit with the data while serving to explain the films' optical properties. To extract meaningful physical information from ellipsometry measures requires an optical model of the sample that accounts for multiple distinct layers with different optical dispersions. In particular, the layer interfaces act as optical boundaries where light can be refracted/reflected as per the Fresnel relations¹⁶⁴⁻¹⁶⁵.

Figure 8.1 displays the spectral dependencies of Ψ (azimuth) and Δ (phase change); these ellipsometric parameters are fitted using the appropriate models to find film thickness as well as the optical constants, namely refractive index (n) and extinction coefficient (k). These values are derived from the best fit between experimental and modelled spectra. As indicated in the figure, the curves obtained for the GMO films indicate high agreement between the experimental and simulated data across the experimental temperature range.

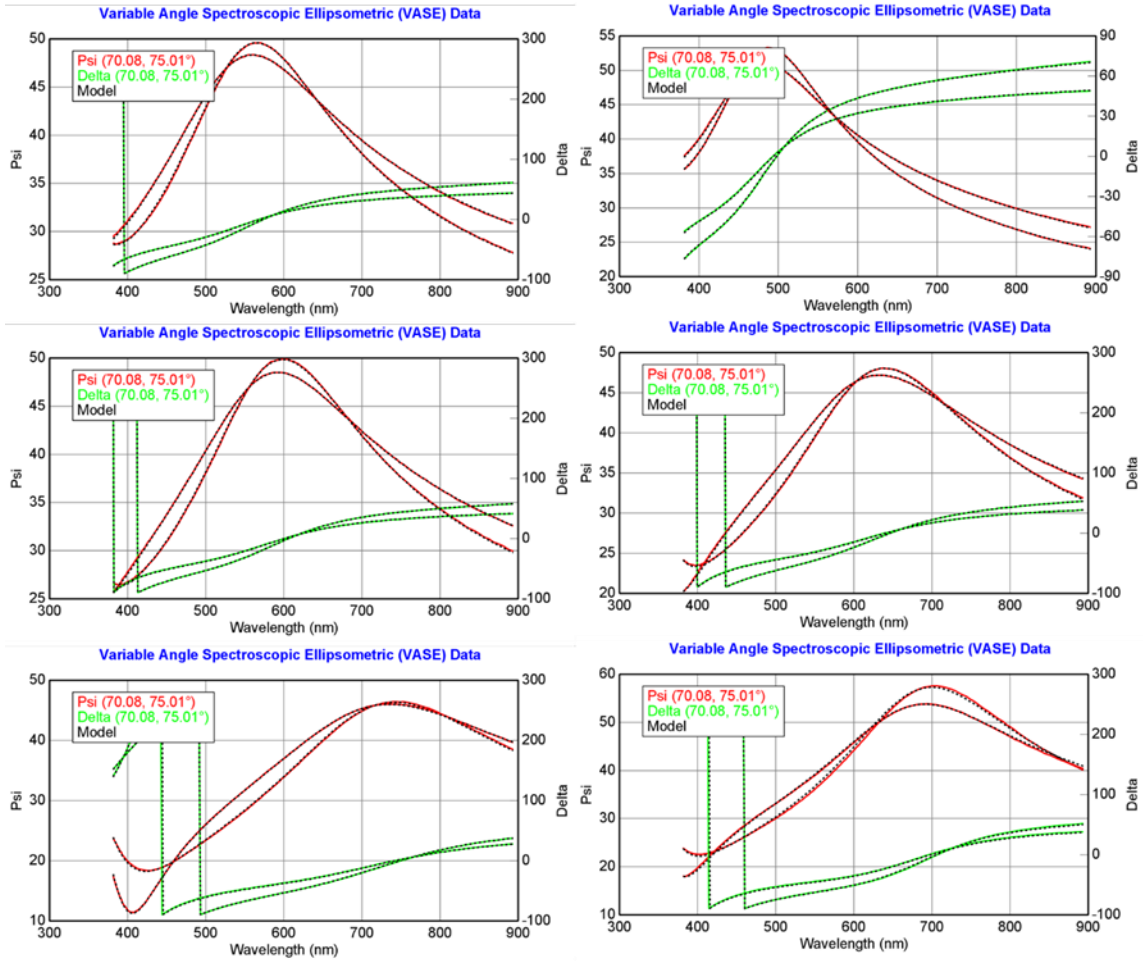


Figure 8.1: Spectral dependence of Ψ and Δ for GMO films. The experimental and modelling curves are shown

Figure 8.2a shows the refractive index and extinction coefficient profiles for the GMO films. There is a gradual decrease in the fundamental absorption of energy across the bandgap correlating with longer wavelengths. However, while the films show a general trend of increasing n values correlating with Mo content up to a Mo sputtering power of 80 W, the 100 W film shows a significant decrease in values, indicating a transition to a more amorphous structure. Increasing Mo content in the films shows a notable decrease in extinction coefficient values, though the unusually sharp decrease for the sample sputtered at 20 W is likely an artifact caused by the unexpectedly low thickness of a particular sample as shown in Figure 8.2b where thickness and

roughness of the samples as a function of applied Mo sputtering power is shown. The general lowering of the k values with increased Mo content indicates the doping procedure results in steadily decreasing optical losses due to absorption, particularly at high wavelengths. This behavior can act as a commentary on the optical quality of film growth and the effect of Mo dopants on gallium oxide films as the strong absorption can be attributed to the high quality of the grown layers and higher transparency with increasing Mo content.

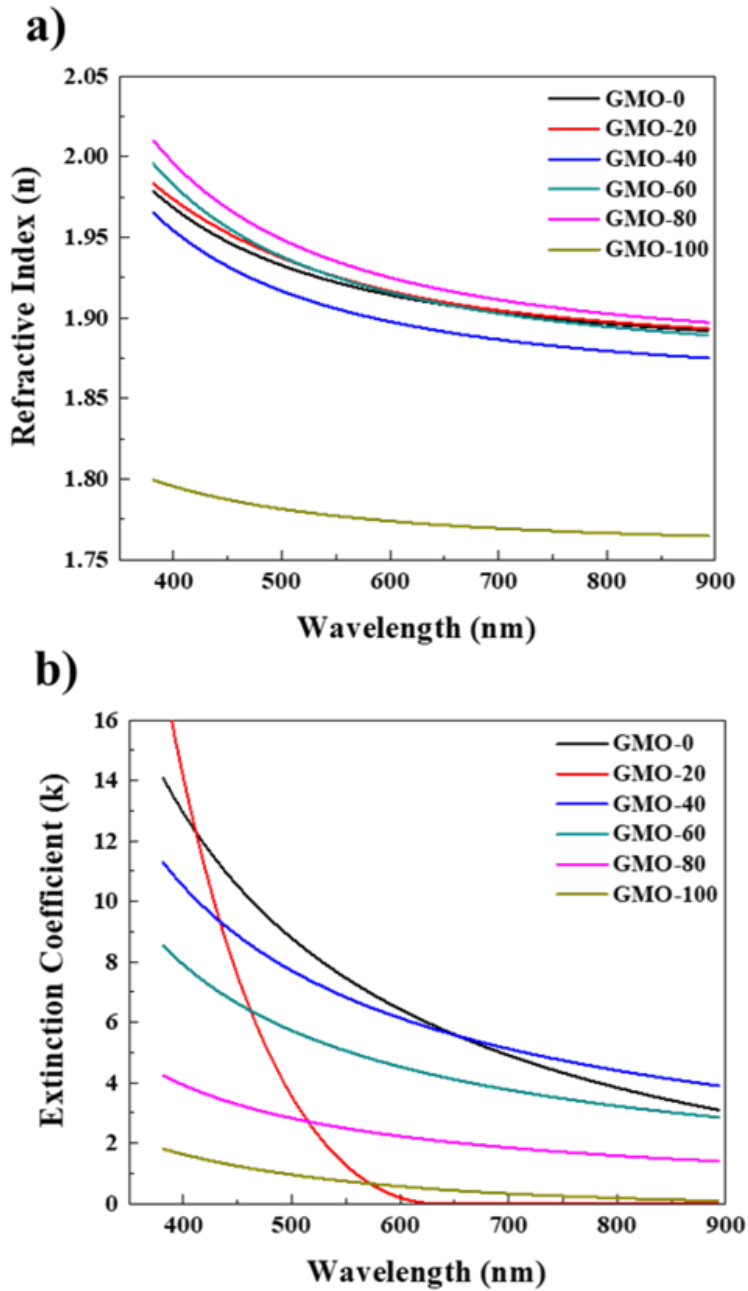


Figure 8.2: a) Refractive index (n) and b) Extinction Coefficient (k) dispersion profiles of GMO samples

The microstructure information such as film thickness and roughness were also obtained from the spectroscopy analysis. The GMO films deposited for a time of 1 h and Mo sputtering power was the only variable. As a result of that, the film thickness varied as a function of Mo sputtering power and/or Mo concentration is represented in Figure 8.3. From the spectroscopy

analysis, it is evident that the film thickness is steadily increased by increasing the Mo sputtering power. The obtained film thickness was approximately 85 nm for GMO film and increased to 115 nm for GMO-100 film. On the other hand, there was no significant change in the roughness, which ranged from between 0.1 to 0.8 nm.

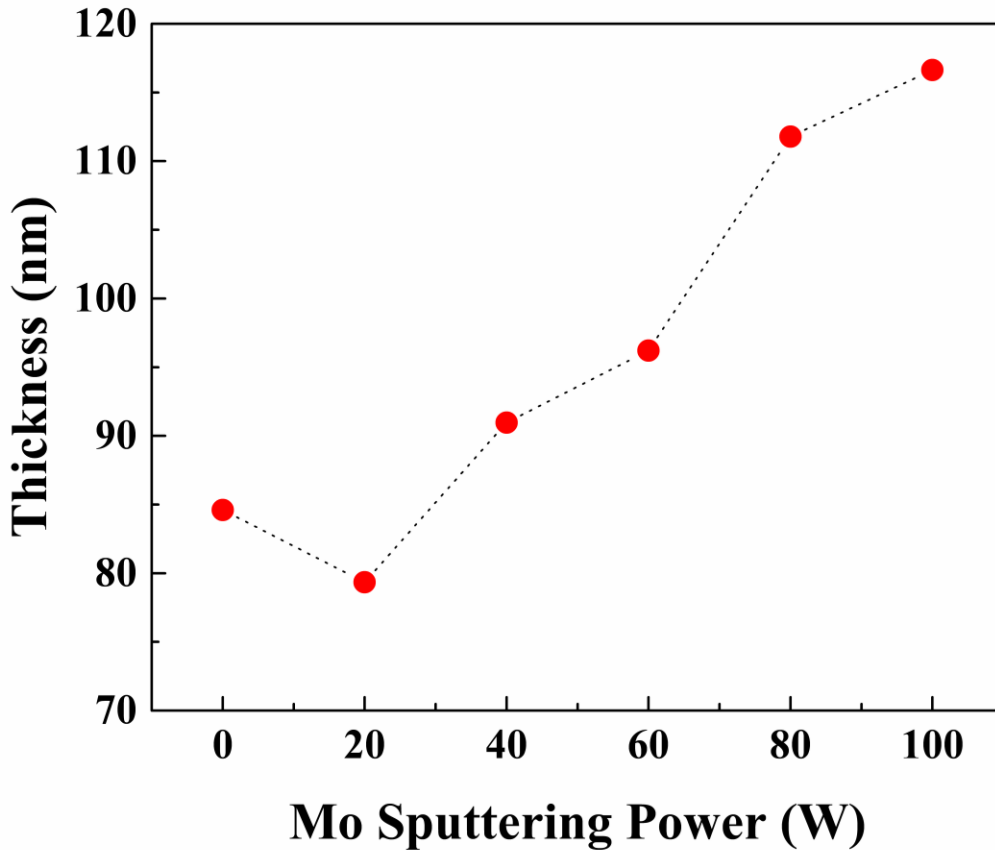


Figure 8.3: Thickness of Mo doped Ga₂O₃ thin films at a different sputtering power

When comparing the refractive index across all samples with regard to certain wavelengths, they remain fairly constant up to Mo concentrations of 11 at% and show an equally constant crystallinity and packing density. However, the sharp decrease in n values, as shown in Figure 8.4, further serves to support the idea of a transition to a decidedly more amorphous phase for the material, indicating that there is a threshold for Mo dopants where material crystallinity will become compromised.

For thin film and nanoscale materials, optical constants are generally very sensitive to the microstructure and chemistry and are heavily influenced by a variety of properties including crystal quality, lattice parameter, defect structure, and packing density. As a result, the good optical quality of intrinsic Ga₂O₃ films is the result of their nanocrystalline structure and stoichiometry, and the noted changes in n and k values can be directly attributed to the introduction of Mo into the structure. The relatively low values of the optical constants observed can thus be assumed to be the result of low packing density and/or stoichiometric defects resulting from the inclusion of the dopant at higher concentrations.

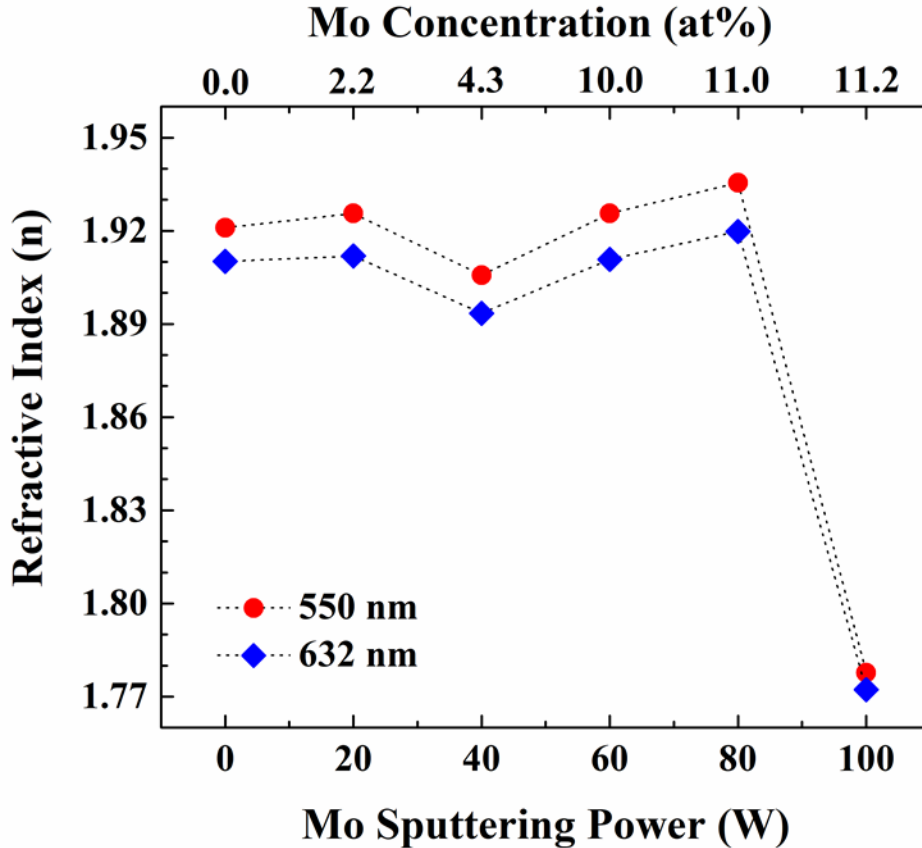


Figure 8.4: Variation of ‘n’ values of GMO samples at different two wavelengths.

Additional evidence for an amorphous transition in the GMO films is demonstrated in Figure 8.5, where the sharp decrease at 100 W of applied power for Mo for relative density stands

in contrast to the relatively constant densities, and correspondingly high crystallinities, of the lower sputter power samples. This also explains the trend shown with the refractive index with increasing Mo content as the density of films and their corresponding refractive indexes are closely related. To confirm this the relative density of the GMO films was calculated using the Lorentz-Lorentz relationship:

$$p = \frac{\rho_f}{\rho_b} = \frac{(n_f^2 - 1)(n_b^2 + 2)}{(n_f^2 + 2)(n_b^2 - 1)} \quad (19)$$

In which ρ_f is the density of the thin film, ρ_b is the density of the bulk material, n_f is mean refractive index of the film, n_b is the refractive index of the bulk material, and p represents the packing density. The bulk refractive index was taken as 1.9201, the value for $\beta\text{-Ga}_2\text{O}_3$. The refractive index was taken at two different wavelengths, 550nm, and 632 nm, to ensure consistency across the spectrum when calculating relative density.

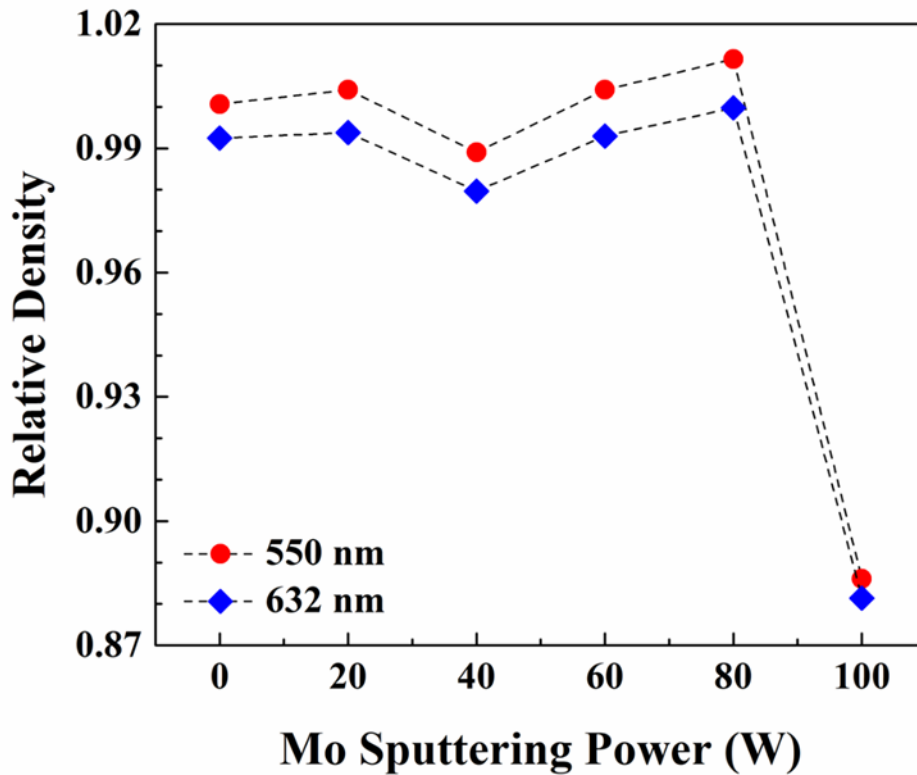


Figure 8.5: Relative density

8.2. Optical Analysis-Spectrophotometry

The spectral transmission characteristics of GMO films are shown in Figure 8.6. It is evident that the GMO films show high transparency in the entire spectral range; however, the sharp decrease in the UV and/or near UV-region corresponds to the incident radiation being absorbed across the bandgap (E_g). Further analysis of the spectra is performed in order to better understand the effect of Mo-incorporation on the optical properties and to derive a quantitative structure-chemical composition-optical property relationship in GMO. For β - Ga_2O_3 with direct bandgap^{34, 166}, the absorption follows a power law of the form:

$$(\alpha h\nu) = B (h\nu - E_g)^{1/2} \quad (7)$$

Where $h\nu$ is the energy of the incident photon, α - the absorption coefficient, B- the absorption edge width parameter, E_g - the bandgap. The optical absorption coefficient, α , is evaluated using the standard relation taking the GMO thickness into account. The absorption is higher in GMO films compared to that of intrinsic Ga_2O_3 films. The absorption data and the plots obtained for GMO films are shown in Figure 6.19. It is evident that $(\alpha h\nu)^2$ vs. $h\nu$ results in linear plots in the high absorption region suggesting direct allowed transitions across E_g . The regression analysis and extrapolating the linear region to $h\nu=0$ provide the E_g value (Figure 8.6). The E_g value for intrinsic Ga_2O_3 (without Mo) is $5.21(\pm 0.03)$ eV. The E_g values were found to decrease with increasing Mo content in GMO films. The variation of E_g with applied sputtering power is shown in Figure 6.19. For the highest sputter-power of 100 W applied to the Mo-target in this work, the E_g decreases significantly down to $4.23(\pm 0.02)$ eV. The E_g -shift, $\Delta E_g \approx 1$ eV, is a substantial redshift associated with Mo-incorporation in Ga_2O_3 .

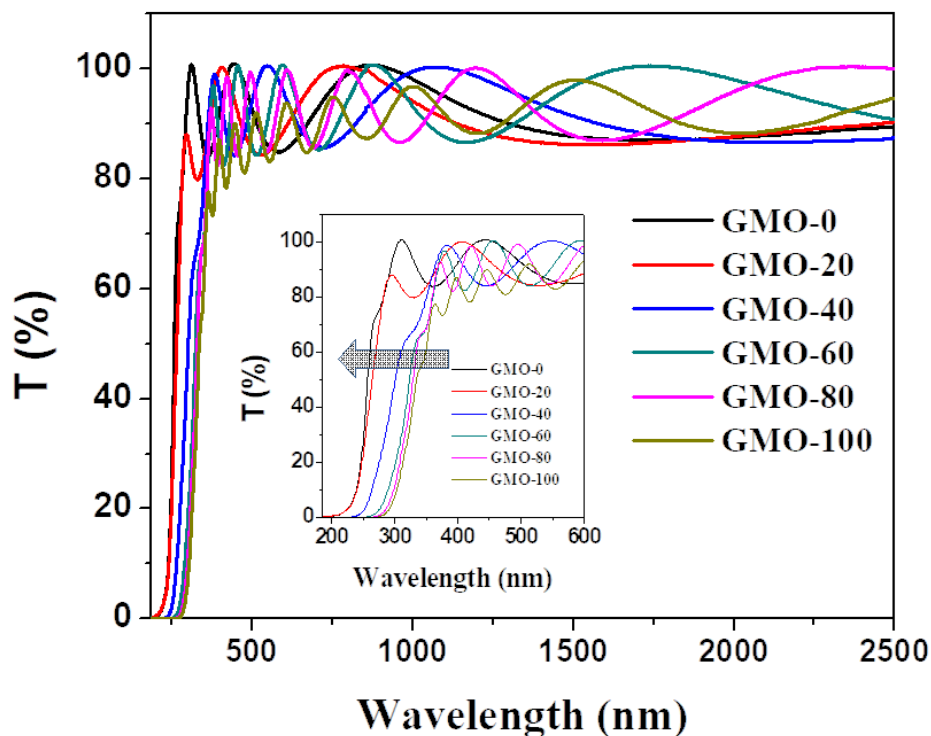


Figure 8.6: Spectral transmission characteristics of GMO films. The Mo-induced shift is evident from the inset, where the expanded region of the absorption region is shown

The effect of Mo-incorporation and the physics/chemistry of electronic structure changes leading to a substantial redshift in E_g can be understood as follows. We first consider the crystallographic data of Ga- and Mo- oxides separately and then consider the Mo-incorporation induced changes in the crystal structure of Ga_2O_3 . Most important to note is the fact that both Ga_2O_3 and MoO_3 exhibit polymorphism. While MoO_3 oxide exhibits only the orthorhombic and monoclinic phases routinely, the monoclinic phase is thermodynamically favourable for Ga_2O_3 ^{19, 50, 167-170}. If the ionic sizes are comparable, a solid solution without any structure change can be expected for Mo-incorporation into Ga_2O_3 lattice i.e., Mo can occupy the lattice positions of Ga inside the β -phase structure of Ga_2O_3 . This indeed is seen in XRD data (Figure 6.1), where no evidence of secondary phase or no distortion of the peaks of the parent β - Ga_2O_3 for Mo

concentration ≤ 4 at%. Thus, combined crystal structure and chemical composition analyses indicate that GMO films accommodate Mo-atoms without any structural distortion up to 4 at%, at which the onset of changes in texturing and/or secondary phase formation occurs, as revealed by XRD studies. The reason for GMO single-phase system could be the comparable ionic radii of Ga^{3+} and Mo^{6+} ions which are 0.062 nm and 0.059 nm, respectively¹⁷¹⁻¹⁷². Note that the ionic radius of Mo^{6+} is, in fact, lower, compared to that of Ga^{3+} . However, Mo ions can be occupied by the Ga_2O_3 structure without any perturbation only up to a certain concentration limit. Exceeding such limits might result in Mo occupying interstitial positions leading to changes in crystal structures observed for GMO films with $\text{Mo} > 4$ at%.

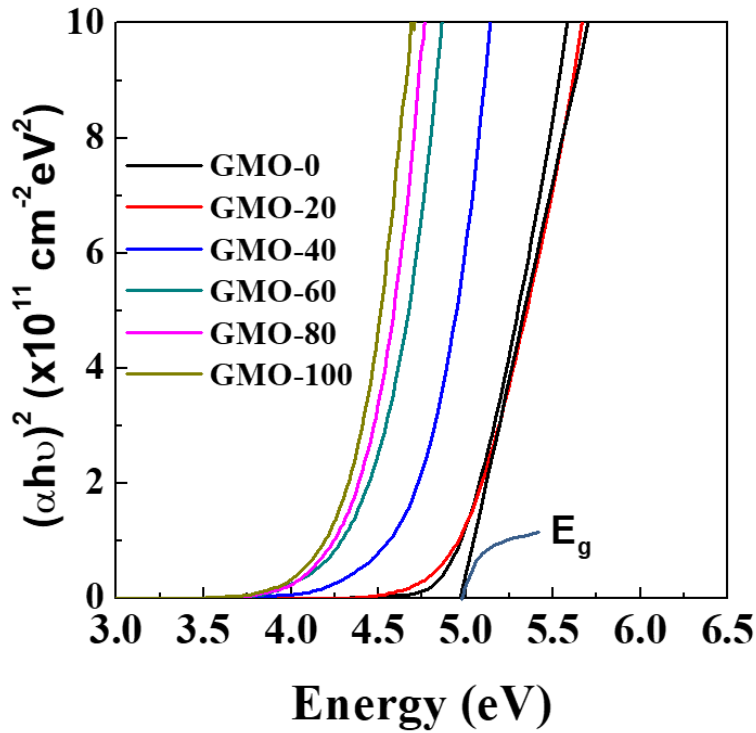


Figure 8.7: $(\alpha h\nu)^2$ vs. $h\nu$ plots of GMO. The linear region is extrapolated to zero absorption to obtain the E_g value. The absorption edge shift towards lower energy is evident.

The effect of Mo incorporation into Ga₂O₃ on the optical properties can then be understood as follows. The E_g value measured for Ga₂O₃ films without any Mo-incorporation (5.2 eV) is in reasonable agreement with that reported for β-Ga₂O₃^{43, 50}. Mo-incorporation effectively reduces E_g leading to a substantial red-shift of the cut edge (Figure 8.7). For the initial Mo-incorporation in the GMO films at Mo content ≤4 at%, Mo ions may form donor levels within the bandgap of Ga₂O₃. This is due to the substitutional nature of Mo in Ga₂O₃ as evidenced by crystal structure studies. Increasing the sputtering power to Mo-metal target from 0 to 100 W increases the effective Mo content incorporated into the Ga₂O₃. In turn, this will increase the donor levels within the bandgap which is responsible for the effective reduction of the bandgap. This accounts for the observed red-shift in the bandgap of Ga₂O₃. The substantial shift can be attributed to the Mo-ions able to form a single-phase system. This evidence comes from the structural analysis of the films where no perturbation to the parent crystal structure is seen, although the formation of the Ga₂O₃-MoO₃ composite at higher Mo content cannot be ruled out. It should be noted that the E_g of MoO₃ is ~3.2 eV¹⁷³. The measured E_g is not even close to this value which is an indication that the composite film consists of Ga₂O₃ as the dominant phase while MoO₃ may be only a minor component. We believe that there may be further options available to tune the structure and optical properties of Mo-Ga₂O₃ materials, which could be useful for improved TCO and photo-catalytic applications.

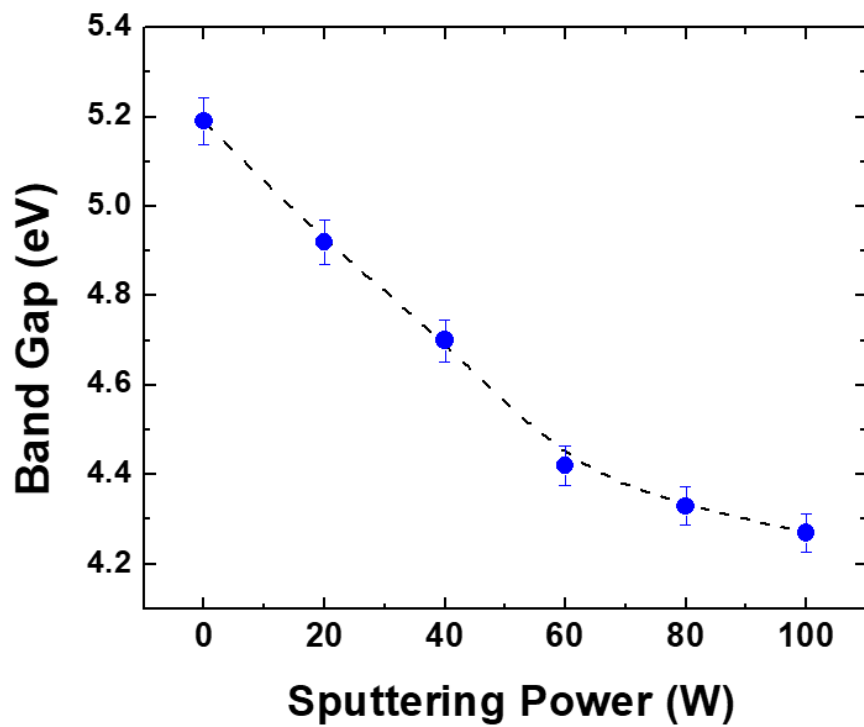


Figure 8.8: Variation in bandgap as a function of Mo sputtering power. A significant reduction in E_g with Mo is evident.

Chapter 9: Molybdenum Incorporated Ga₂O₃ Nanocrystalline Thin Films – Oxygen Sensor Performance Evaluation

9.1. Electrical Analysis - Hall Effect Measurements

In addition to structural and morphological characteristics, the electrical characteristics of Mo-doped Ga₂O₃ are quite important for this material's integration into sensor applications. Therefore, the electrical characteristics of GMO films were evaluated thoroughly. Figure 9.1 represents the electrical characteristics of Mo-doped Ga₂O₃ thin films with variable Mo sputtering power. The electrical mobility, resistance, and conductivity are shown with variable Mo at%. The Hall mobility was seen to gradually increase with increasing Mo at%. The mobility value was ~23 cm²/V-s for intrinsic Ga₂O₃ film (GMO-0) and increased to ~90 cm²/V-s for GMO-100. This phenomenon could be explained by the fact that, in general, for any uniformly doped semiconductor structure the number of minority phases, especially binary minority phases, will reduce when increasing the doping concentration, which ultimately leads to enhancement in the mobility values¹⁷⁴⁻¹⁷⁵.

The resistivity values were decreased continuously by incorporating the Mo concentration. For GMO film, the resistivity was ~8.4E+4 Ω-cm, while for GMO-100 film, the values decreased continuously and reached ~3.3E+4 Ω-cm. Serrao et al. reported that thickness and electrical resistivity are inversely proportional to each other, i.e., by increasing the film thickness, resistivity will decrease¹⁷⁶⁻¹⁷⁸. In this study, except for the Mo sputtering power, every deposition condition remained constant. By observing the ellipsometry results, the film thickness increased due to increasing the sputtering power. On the other hand, conductivity is increased by incorporating Mo into Ga₂O₃ films. Doping Mo in Ga₂O₃ increases the oxygen vacancies and hence tends to create

an additional source of free electrons¹⁷⁹⁻¹⁸⁰. This phenomenon will lead to enhancements in the n-type conductivity of the GMO films.

Finally, the effects of Mo content on the microstructure can be seen in the electrical resistivity of the GMO films. Namely, the electrical resistivity tends to become higher with grain size reduction due to increasing grain boundary volume and associated charge carrier flow impedance. Additionally, lattice imperfections, including vacancies and dislocations, are often present in nanocrystalline material and have a strong influence on electrical resistivity. An amorphous structure, for the given material, would tend to lack these features leading to overall decreased electrical resistivity and corroborating the trend indicated with the ellipsometry measurements¹⁸¹.

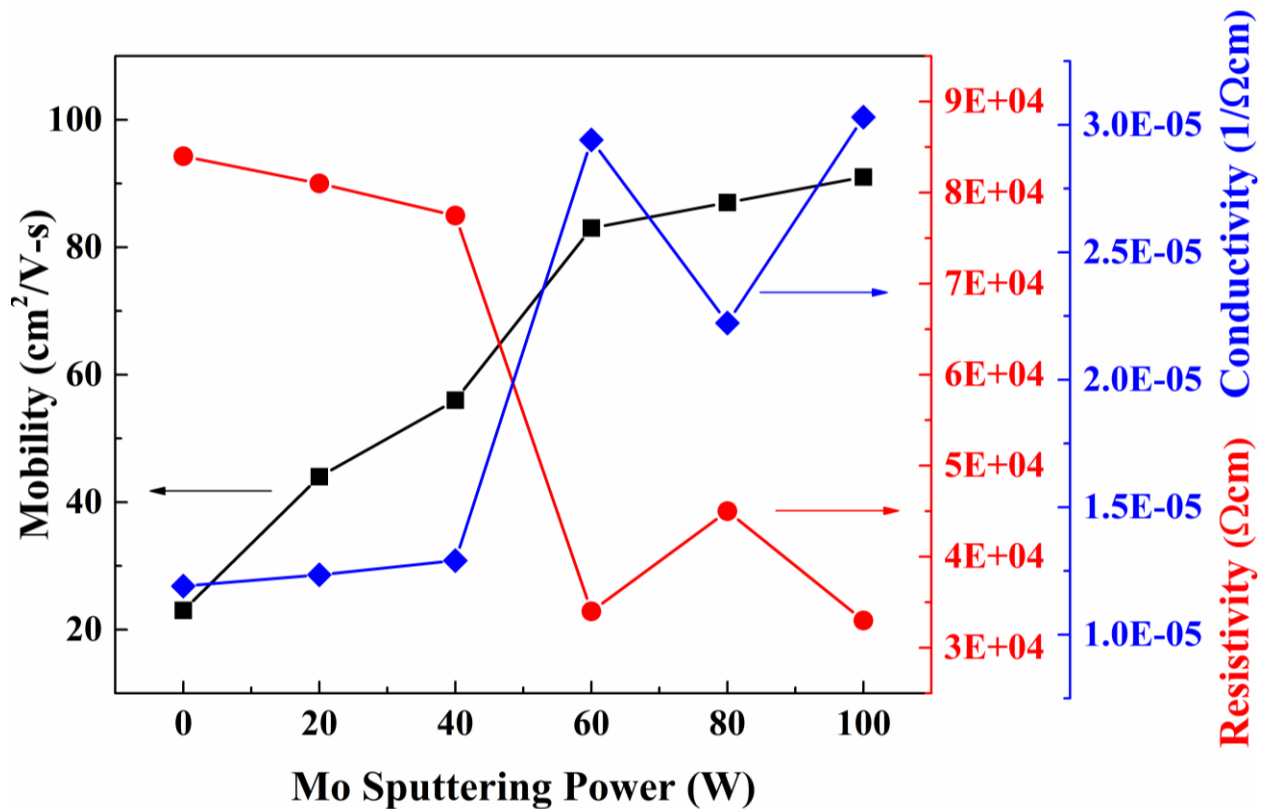


Figure 9.1: Electrical characteristics of GMO films at various Mo concentration.

9.2. Gas Sensing Analysis - High-Temperature Sensor Performance

The temperature-dependent electrical data of GMO samples are represented in Figure 9.2. The mechanism between the grains acts as a vital role in sensor conductivity, which has a Schottky-type nature. Therefore, finding out the activation energy plays an important role in determining the sensor qualities. The activation energy (E_A), i.e., the minimum energy molecules must possess to undergo a specified reaction, will be calculated from the slope of temperature-dependent electrical data using the relation

$$R = R_{\infty} e^{\left(\frac{E_A}{kT}\right)} \quad (20)$$

where R represents resistance, R_{∞} represents resistance at infinite temperature, E_A represents activation energy, k represents the Boltzmann constant, and T represents an absolute temperature. The temperature-dependent resistance values increased up to GMO-60 film (10 at%), but when further increasing Mo at%, the resistance values decreased, as shown in Figure 9.2. The E_A will be calculated based on the slope of temperature-dependent electrical data, represented in Figure 9.3. The E_A values decreased continuously for GMO films. The E_A value for intrinsic Ga_2O_3 film (GMO-0) is approximately 1 to 1.05 eV. By increasing the Mo content to 2 at%, the E_A value is slightly higher and within the error range. Further increasing the Mo content, the E_A values were decreasing continuously and for the atomic percentage of 11.23, the E_A value was around 0.30 eV. This phenomenon shows that the required thermal energy is becoming lower by incorporating the Mo content into Ga_2O_3 to detect the oxygen.

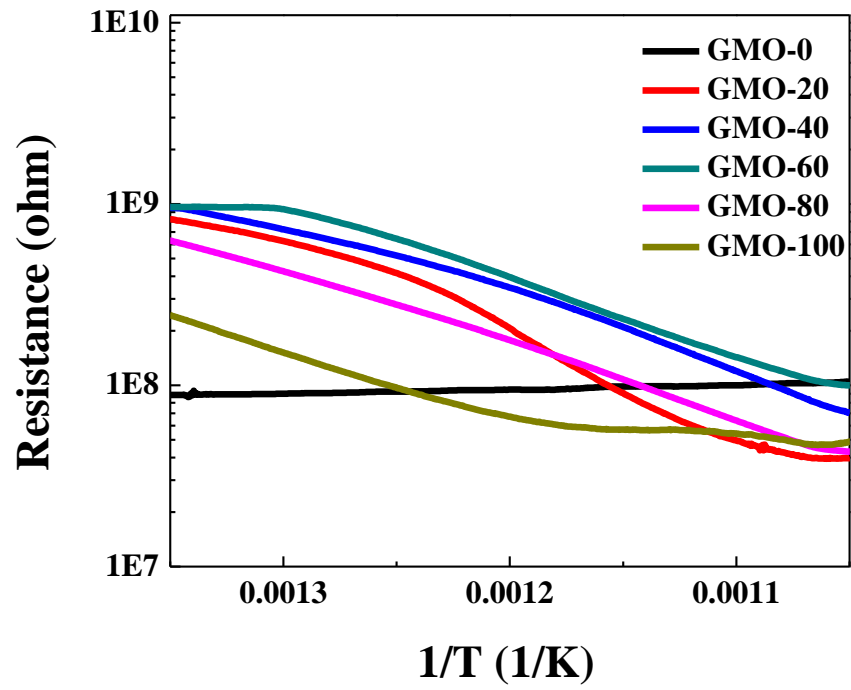


Figure 9.2: Electrical data of GMO films. Arrhenius plots are shown for samples with variable Mo content.

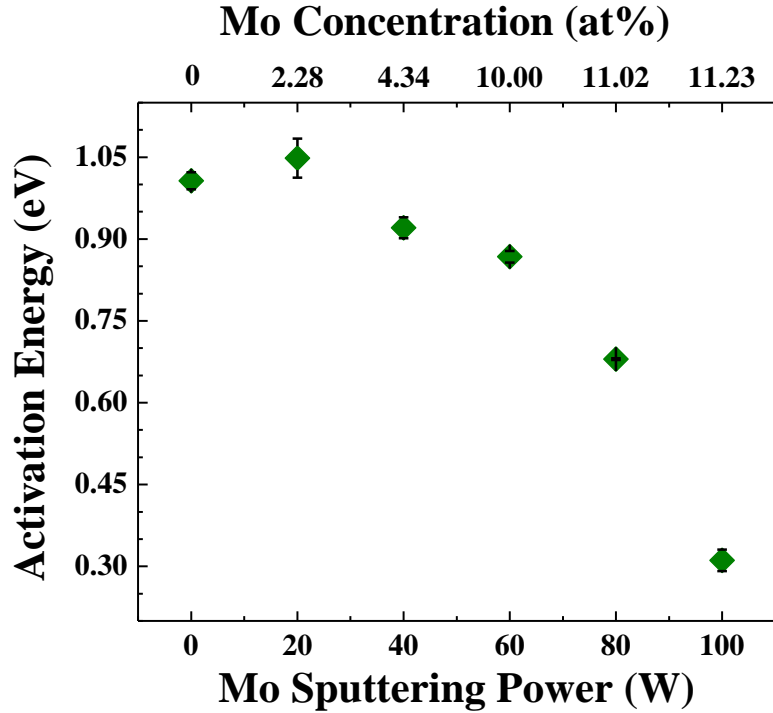


Figure 9.3: Activation energy of GMO films. The continuous decrease in EA values with Mo incorporation into Ga_2O_3 can be noted.

The oxygen sensor response in terms of resistance for GMO thin films is represented in Figure 9.4. The experiments were performed at a constant temperature of 500 °C at different oxygen partial pressures ($p\text{O}_2$) between 8 to 40 Pa in a cyclic manner. Pure Ar gas at a constant flow was introduced along with the $p\text{O}_2$ gas into a controlled environment. The schematic representation of the oxygen sensing setup is represented in Figure 4.12. The experiments were conducted ≥ 100 h to check stability and repeatability and maintained for 12 min of constant time between successive cycles. The resistance value increased rapidly when O_2 gas introduced for GMO-0. The intrinsic Ga_2O_3 (GMO-0) widely studied and suitable for oxygen sensing, reported in the literature^{7, 17, 32-33, 182}. GMO-20 film following the same trend concerning GMO-0 film. As discussed in the XRD and XPS, GMO-20 film had an Mo content of 2.25 at%, which was very low and did not have much effect in altering the intrinsic properties. On the other hand, for the

films GMO-40, GMO-60, and GMO-80, the resistance was flipped, i.e., when O₂ was introduced into the chamber, the resistivity decreased and vice-versa. This might be due to an increase in the Mo content of the films, which were 4.35 at% (GMO-40) and 11 at% (GMO-80). The same phenomena were observed in titanium introduced into Ga₂O₃ thin films as reported by Manandhar et al.¹⁷. However, for GMO-100 film, the resistance again increased and followed the same behavior as GMO-0. At the same time, there was a rapid response.

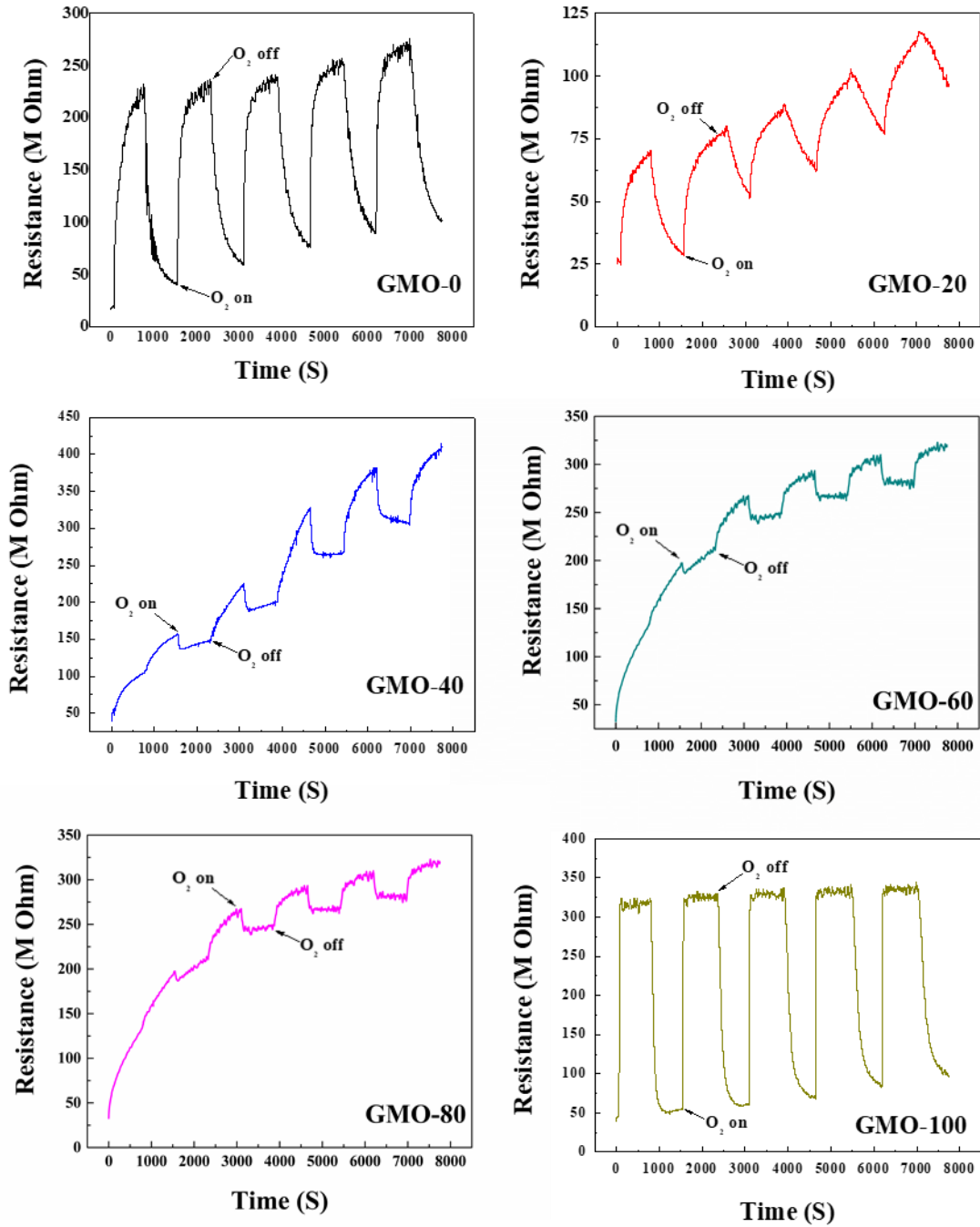


Figure 9.4: Gas sensing performance test for GMO films

Moseley et. al. mentioned the relation between pO_2 and the conductivity of mixed valence oxide sensor represented by¹⁸³:

$$\sigma = A * \exp \left[-\frac{E_A}{kT} \right] pO_2^{1/m} \quad (21)$$

where E_A represents the activation energy of the sensing film, k represents the Boltzmann constant, A represents a constant, T represents absolute temperature, pO_2 represents oxygen partial pressure, and m represents a parameter determined by the carriers (either n or p -type) and the defects in the oxide. The $|m|$ value gives the sensitivity of the sensor, i.e., the higher the value, the higher the sensitivity. The corresponding m values of GMO films are represented in Figure 9.5a. GMO-0 film (intrinsic Ga_2O_3) has an m value of -5.5, which is in close agreement with the literature. Frank et. al. and Ogita et. al. reported an m value of -4 for the bulk Ga_2O_3 ^{90, 95}. However, incorporating Mo into Ga_2O_3 altered the oxygen sensitivity properties. The m value was increased from -5.5 (GMO-0) to -0.5 (GMO-40); from there the value is reduced gradually, and finally for GMO-100 (11.23 at% of Mo) it is approximately -6.5. As per the equation reported by Moseley et al., the higher the value, the higher the sensitivity.

Figure 9.5b represents the response time in seconds for GMO thin films. Note that the response time is calculated based on the standard procedure. The response time for the GMO-0 film (intrinsic Ga_2O_3) is 25 ± 5 s, whereas incorporating Mo into Ga_2O_3 reduces the response time. For the film GMO-20, the response time increased abruptly to 70 ± 5 ; from there the response time reduced gradually, and finally for GMO-100 it was ~ 4 s at 11.23 at% of Mo, which is evident from the Figure 6.6. The response time can be influenced by the surface reaction rate and/or the diffusion rate. When pO_2 is increased, the oxygen molecules adsorbed at the surface split and occupy the vacancies near the surface. A diffusion process of oxygen inside the film, across the grain boundaries, will reestablish equilibrium with the gas phase^{32, 90}.

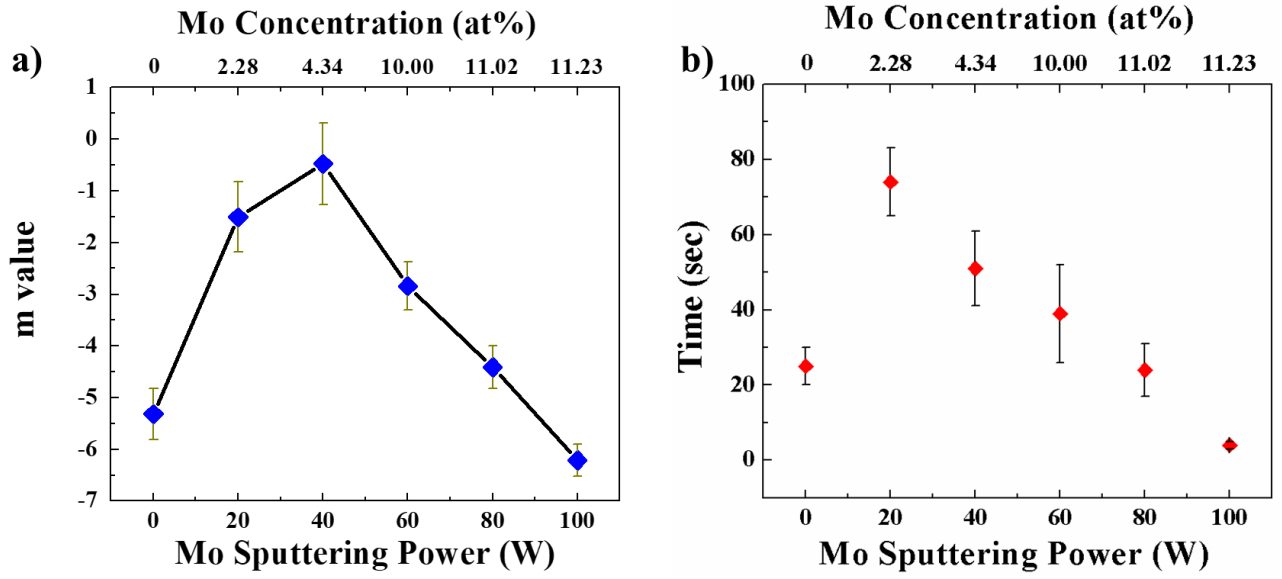


Figure 9.5: Oxygen sensor performance of characteristic values of GMO films. (a) m value (b) Response time determined from functional electrical characteristics of GMO

Chapter 10: Summary and Conclusions

The various studies were performed in this research to understand the overall phenomena of refractory metal doping, in this context molybdenum into gallium oxide thin films. Summarizing the results, Ga₂O₃ and Mo-incorporated Ga₂O₃ films were fabricated and their structural, chemical and optical properties were investigated. The effect of Mo-incorporation is significant to the structural and optical properties of Ga₂O₃. Mo-induced linear variability in E_g is demonstrated for Ga₂O₃. Based on the results, the Mo-incorporated Ga₂O₃ was found to be a chemically and optically variable system, where materials with desired electronic properties can be obtained for specific optoelectronics and photo-catalytic applications.

The GMO nanocomposite films with variable Mo contents (0-11.23 at%) were sputter-deposited onto Si(100) by varying the sputtering power ranging from 0 W to 100 W. The effect of Mo on the crystal structure and mechanical properties of GMO nanocomposite films was significant. While Mo content ≤ 4 at% retained the β -Ga₂O₃ phase, higher Mo content induced amorphization. Molybdenum incorporation into β -Ga₂O₃ reduced the grain size, leading to the amorphous nature of the entire film as well as its surfaces. The nano-indentation studies indicated the remarkable effect of structural evolution and Mo content on the mechanical properties of the deposited GMO thin films. While Mo incorporation increased the hardness from 25 to 36 GPa, elastic modulus decreased. Incorporation of Mo in the Ga-oxide phase with increased grain boundaries to resist dislocation movements is understood to be the primary reason for elevated mechanical characteristics. Molybdenum content of 4-5 at% was shown to be the optimum amount to produce β -Ga₂O₃ nanocrystalline films with structural quality and enhanced mechanical characteristics for application in energy systems.

Finally, based on the extensive characterization, results obtained and detailed analyses, we believe that this thesis work presents an interesting scientific approach to design refractory-metal incorporated Ga₂O₃-based materials with controlled structural, mechanical, and optical properties. The the combined effect of Mo-doping and processing parameters on the properties and oxygen sensor performance of GMO nanomaterials as presented and discussed may be applicable to a large class of RM-doped Ga₂O₃ materials. Additionally, the present approach of Mo-doping being successful to allow designing Ga₂O₃-based nanomaterials with tunable mechanical properties, there may be further options available to produce unique materials for enhanced technological performance. The oxygen sensor performance evaluation made using laboratory based measurements indicate enhanced sensor performance of GMO for high temperature oxygen sensing. Incorporating Mo into Ga₂O₃ reduces response time of the oxygen sensor by several orders of magnitude. Thus, it may be further possible to tune the conditions or explore other dopants to enhance the oxygen sensor performance under extreme environment conditions.

Chapter 11: Future Work

The following work is recommended for the continuation of this research:

- Investigation of the thermal stability of the Mo doped Ga_2O_3 thin films at higher temperatures.
- Fabrication of Ga-doped MoO_3 sensor for in-situ testing. This will reverse the charge imbalance and will allow the study of Ga in MoO_3 structure.
- 3D printed thin films for sensor applications.

References

1. Demarne, V.; Sanjines, R.; Sberveglieri, G., Gas sensors principles, operation and development. *Kluwer Academic, Netherlands* **1992**.
2. Fleischer, M.; Meixner, H., Fast gas sensors based on metal oxides which are stable at high temperatures. *Sensors and Actuators B: Chemical* **1997**, *43* (1-3), 1-10.
3. Francioso, L.; Presicce, D.; Siciliano, P.; Ficarella, A., Combustion conditions discrimination properties of Pt-doped TiO₂ thin film oxygen sensor. *Sensors and Actuators B: Chemical* **2007**, *123* (1), 516-521.
4. Gao, X.; Zhang, T., An overview: Facet-dependent metal oxide semiconductor gas sensors. *Sensors and Actuators B: Chemical* **2018**, *277*, 604-633.
5. Gönüllü, Y.; Rodríguez, G. C. M.; Saruhan, B.; Ürgen, M., Improvement of gas sensing performance of TiO₂ towards NO₂ by nano-tubular structuring. *Sensors and Actuators B: Chemical* **2012**, *169*, 151-160.
6. Mukherjee, A.; Okolie, J. A.; Abdelrasoul, A.; Niu, C.; Dalai, A. K., Review of post-combustion carbon dioxide capture technologies using activated carbon. *Journal of Environmental Sciences* **2019**.
7. Ramamoorthy, R.; Dutta, P.; Akbar, S., Oxygen sensors: materials, methods, designs and applications. *Journal of materials science* **2003**, *38* (21), 4271-4282.
8. Ivers-Tiffée, E.; Härdtl, K.; Menesklou, W.; Riegel, J., Principles of solid state oxygen sensors for lean combustion gas control. *Electrochimica Acta* **2001**, *47* (5), 807-814.
9. Mahajan, S.; Jagtap, S., Metal-oxide semiconductors for carbon monoxide (CO) gas sensing: A review. *Applied Materials Today* **2019**, 100483.
10. Phanichphant, S., Semiconductor metal oxides as hydrogen gas sensors. *Procedia Eng* **2014**, *87*, 795-802.
11. Kolmakov, A.; Zhang, Y.; Cheng, G.; Moskovits, M., Detection of CO and O₂ using tin oxide nanowire sensors. *Advanced materials* **2003**, *15* (12), 997-1000.
12. Ashik, U.; Kudo, S.; Hayashi, J.-i., An overview of metal oxide nanostructures. In *Synthesis of Inorganic Nanomaterials*, Elsevier: 2018; pp 19-57.
13. Barsan, N.; Koziej, D.; Weimar, U., Metal oxide-based gas sensor research: How to? *Sensors and Actuators B: Chemical* **2007**, *121* (1), 18-35.
14. Paladiya, C.; Kiani, A., Nano structured sensing surface: Significance in sensor fabrication. *Sensors and Actuators B: Chemical* **2018**, *268*, 494-511.
15. Dey, A., Semiconductor metal oxide gas sensors: A review. *Materials Science and Engineering: B* **2018**, *229*, 206-217.
16. Kumar, A.; Kumar, M.; Kumar, R.; Singh, R.; Prasad, B.; Kumar, D., Numerical model for the chemical adsorption of oxygen and reducing gas molecules in presence of humidity on the surface of semiconductor metal oxide for gas sensors applications. *Materials Science in Semiconductor Processing* **2019**, *90*, 236-244.
17. Manandhar, S.; Battu, A. K.; Devaraj, A.; Shutthanandan, V.; Thevuthasan, S.; Ramana, C., Rapid Response High Temperature Oxygen Sensor Based on Titanium Doped Gallium Oxide. *Scientific Reports* **2020**, *10* (1), 1-9.
18. Rebholz, C.; Leyland, A.; Schneider, J.; Voevodin, A.; Matthews, A., Structure, hardness and mechanical properties of magnetron-sputtered titanium–aluminium boride films. *Surface and Coatings Technology* **1999**, *120*, 412-417.

19. McCarron III, E.; Calabrese, J., The growth and single crystal structure of a high pressure phase of molybdenum trioxide: MoO₃-II. *Journal of solid state chemistry* **1991**, *91* (1), 121-125.
20. Sunu, S.; Prabhu, E.; Jayaraman, V.; Gnanasekar, K.; Gnanasekaran, T., Gas sensing properties of PLD made MoO₃ films. *Sensors and Actuators B: Chemical* **2003**, *94* (2), 189-196.
21. Lang, A.; Fleischer, M.; Meixner, H., Surface modifications of Ga₂O₃ thin film sensors with Rh, Ru and Ir clusters. *Sensors and Actuators B: Chemical* **2000**, *66* (1-3), 80-84.
22. Henrich, V.; Cox, P., *The Surface Science of Metal Oxides* Cambridge Univ. Press Cambridge: 1994.
23. Williams, D. E., Semiconducting oxides as gas-sensitive resistors. *Sensors and Actuators B: Chemical* **1999**, *57* (1-3), 1-16.
24. Comini, E.; Faglia, G.; Sberveglieri, G.; Pan, Z.; Wang, Z. L., Stable and highly sensitive gas sensors based on semiconducting oxide nanobelts. *Applied Physics Letters* **2002**, *81* (10), 1869-1871.
25. Varghese, O. K.; Grimes, C. A., Metal oxide nanoarchitectures for environmental sensing. *Journal of nanoscience and nanotechnology* **2003**, *3* (4), 277-293.
26. Fan, C.; Li, C.; Inoue, A.; Haas, V., Deformation behavior of Zr-based bulk nanocrystalline amorphous alloys. *Physical Review B* **2000**, *61* (6), R3761.
27. Reimer, A., *Horizons in World Physics*. Nova Publishers: 2004; Vol. 244.
28. Eranna, G.; Joshi, B.; Runthala, D.; Gupta, R., Oxide materials for development of integrated gas sensors—a comprehensive review. *Critical Reviews in Solid State and Materials Sciences* **2004**, *29* (3-4), 111-188.
29. Stepanov, S.; Nikolaev, V.; Bougrov, V.; Romanov, A., Gallium OXIDE: Properties and applica 498 a review. *Rev. Adv. Mater. Sci* **2016**, *44*, 63-86.
30. Yao, Y.; Davis, R. F.; Porter, L. M., Investigation of different metals as ohmic contacts to β-Ga₂O₃: comparison and analysis of electrical behavior, morphology, and other physical properties. *Journal of Electronic Materials* **2017**, *46* (4), 2053-2060.
31. Manandhar, S.; Ramana, C., Direct, functional relationship between structural and optical properties in titanium-incorporated gallium oxide nanocrystalline thin films. *Applied Physics Letters* **2017**, *110* (6), 061902.
32. Baban, C.; Toyoda, Y.; Ogita, M., Oxygen sensing at high temperatures using Ga₂O₃ films. *Thin Solid Films* **2005**, *484* (1-2), 369-373.
33. Bartic, M.; Baban, C. I.; Suzuki, H.; Ogita, M.; Isai, M., β-Gallium Oxide as Oxygen Gas Sensors at a High Temperature. *Journal of the American Ceramic Society* **2007**, *90* (9), 2879-2884.
34. Orita, M.; Ohta, H.; Hirano, M.; Hosono, H., Deep-ultraviolet transparent conductive β-Ga₂O₃ thin films. *Applied Physics Letters* **2000**, *77* (25), 4166-4168.
35. Zhang, W.; Ou, J. Z.; Tang, S. Y.; Sivan, V.; Yao, D. D.; Latham, K.; Khoshmanesh, K.; Mitchell, A.; O'Mullane, A. P.; Kalantar-zadeh, K., Liquid metal/metal oxide frameworks. *Advanced Functional Materials* **2014**, *24* (24), 3799-3807.
36. Hayashi, H.; Huang, R.; Ikeno, H.; Oba, F.; Yoshioka, S.; Tanaka, I.; Sonoda, S., Room temperature ferromagnetism in Mn-doped γ-Ga₂O₃ with spinel structure. *Applied physics letters* **2006**, *89* (18), 181903.
37. Guo, D.; Wu, Z.; An, Y.; Li, X.; Guo, X.; Chu, X.; Sun, C.; Lei, M.; Li, L.; Cao, L., Room temperature ferromagnetism in (Ga_{1-x}Mn_x)₂O₃ epitaxial thin films. *Journal of Materials Chemistry C* **2015**, *3* (8), 1830-1834.
38. Wu, X.; Song, W.; Huang, W.; Pu, M.; Zhao, B.; Sun, Y.; Du, J., Crystalline gallium oxide nanowires: intensive blue light emitters. *Chemical Physics Letters* **2000**, *328* (1-2), 5-9.

39. Ho, H.; Lo, K.; Fu, K.; Chu, P.; Li, K.; Cheah, K., Synthesis of beta gallium oxide nano-ribbons from gallium arsenide by plasma immersion ion implantation and rapid thermal annealing. *Chemical physics letters* **2003**, 382 (5-6), 573-577.
40. Zhang, Y.; Yan, J.; Li, Q.; Qu, C.; Zhang, L.; Xie, W., Optical and structural properties of Cu-doped β -Ga₂O₃ films. *Materials Science and Engineering: B* **2011**, 176 (11), 846-849.
41. Xu, W.; Cao, H.; Liang, L.; Xu, J.-B., Aqueous solution-deposited gallium oxide dielectric for low-temperature, low-operating-voltage indium oxide thin-film transistors: a facile route to green oxide electronics. *ACS applied materials & interfaces* **2015**, 7 (27), 14720-14725.
42. López, I. a.; Nogales, E.; Méndez, B.; Piqueras, J.; Peche, A.; Ramírez-Castellanos, J.; González-Calbet, J. M., Influence of Sn and Cr doping on morphology and luminescence of thermally grown Ga₂O₃ nanowires. *The Journal of Physical Chemistry C* **2013**, 117 (6), 3036-3045.
43. Rubio, E.; Ramana, C., Tungsten-incorporation induced red-shift in the bandgap of gallium oxide thin films. *Applied Physics Letters* **2013**, 102 (19), 191913.
44. Hwang, W. S.; Verma, A.; Peelaers, H.; Protasenko, V.; Rouvimov, S.; Xing, H.; Seabaugh, A.; Haensch, W.; de Walle, C. V.; Galazka, Z., High-voltage field effect transistors with wide-bandgap β -Ga₂O₃ nanomembranes. *Applied Physics Letters* **2014**, 104 (20), 203111.
45. Oshima, T.; Wakabayashi, R.; Hattori, M.; Hashiguchi, A.; Kawano, N.; Sasaki, K.; Masui, T.; Kuramata, A.; Yamakoshi, S.; Yoshimatsu, K., Formation of indium–tin oxide ohmic contacts for β -Ga₂O₃. *Japanese Journal of Applied Physics* **2016**, 55 (12), 1202B7.
46. Atuchin, V. V.; Gavrilova, T. A.; Gromilov, S. A.; Kostrovsky, V. G.; Pokrovsky, L. D.; Troitskaia, I. B.; Vemuri, R.; Carbajal-Franco, G.; Ramana, C., Low-temperature chemical synthesis and microstructure analysis of GeO₂ crystals with α -quartz structure. *Crystal Growth and Design* **2009**, 9 (4), 1829-1832.
47. Shvets, V.; Aliev, V. S.; Gritsenko, D.; Shaimeev, S.; Fedosenko, E.; Rykhlytski, S.; Atuchin, V.; Gritsenko, V.; Tapilin, V.; Wong, H., Electronic structure and charge transport properties of amorphous Ta₂O₅ films. *Journal of non-crystalline solids* **2008**, 354 (26), 3025-3033.
48. Ramana, C.; Vemuri, R.; Kaichev, V.; Kochubey, V.; Saraev, A.; Atuchin, V., X-ray photoelectron spectroscopy depth profiling of La₂O₃/Si thin films deposited by reactive magnetron sputtering. *ACS applied materials & interfaces* **2011**, 3 (11), 4370-4373.
49. Mudavakkat, V.; Atuchin, V.; Kruchinin, V.; Kayani, A.; Ramana, C., Structure, morphology and optical properties of nanocrystalline yttrium oxide (Y₂O₃) thin films. *Optical Materials* **2012**, 34 (5), 893-900.
50. Kumar, S. S.; Rubio, E.; Noor-A-Alam, M.; Martinez, G.; Manandhar, S.; Shutthanandan, V.; Thevuthasan, S.; Ramana, C., Structure, morphology, and optical properties of amorphous and nanocrystalline gallium oxide thin films. *The Journal of Physical Chemistry C* **2013**, 117 (8), 4194-4200.
51. Muhammed, M.; Roldan, M.; Yamashita, Y.; Sahonta, S.-L.; Ajia, I. A.; Iizuka, K.; Kuramata, A.; Humphreys, C.; Roqan, I., High-quality III-nitride films on conductive, transparent ($\bar{2}01$)-oriented β -Ga₂O₃ using a GaN buffer layer. *Scientific reports* **2016**, 6, 29747.
52. Zavabeti, A.; Ou, J. Z.; Carey, B. J.; Syed, N.; Orrell-Trigg, R.; Mayes, E. L.; Xu, C.; Kavehei, O.; O'Mullane, A. P.; Kaner, R. B., A liquid metal reaction environment for the room-temperature synthesis of atomically thin metal oxides. *Science* **2017**, 358 (6361), 332-335.

53. Kim, J.; Sekiya, T.; Miyokawa, N.; Watanabe, N.; Kimoto, K.; Ide, K.; Toda, Y.; Ueda, S.; Ohashi, N.; Hiramatsu, H., Conversion of an ultra-wide bandgap amorphous oxide insulator to a semiconductor. *NPG Asia Materials* **2017**, *9* (3), e359-e359.
54. Hu, J.; Li, Q.; Zhan, J.; Jiao, Y.; Liu, Z.; Ringer, S. P.; Bando, Y.; Golberg, D., Unconventional ribbon-shaped β -Ga₂O₃ tubes with mobile Sn nanowire fillings. *ACS nano* **2008**, *2* (1), 107-112.
55. Pearnton, S.; Yang, J.; Cary IV, P. H.; Ren, F.; Kim, J.; Tadjer, M. J.; Mastro, M. A., A review of Ga₂O₃ materials, processing, and devices. *Applied Physics Reviews* **2018**, *5* (1), 011301.
56. Levin, I.; Brandon, D., Metastable alumina polymorphs: crystal structures and transition sequences. *Journal of the American Ceramic Society* **1998**, *81* (8), 1995-2012.
57. Marezio, M.; Remeika, J., Bond Lengths in the α -Ga₂O₃ Structure and the High-Pressure Phase of Ga_{2-x}Fe_xO₃. *The Journal of Chemical Physics* **1967**, *46* (5), 1862-1865.
58. Tomm, Y.; Ko, J.; Yoshikawa, A.; Fukuda, T., Floating zone growth of β -Ga₂O₃: a new window material for optoelectronic device applications. *Solar energy materials and solar cells* **2001**, *66* (1-4), 369-374.
59. Nikolaev, V.; Maslov, V.; Stepanov, S.; Pechnikov, A.; Krymov, V.; Nikitina, I.; Guzilova, L.; Bougrov, V.; Romanov, A., Growth and characterization of β -Ga₂O₃ crystals. *Journal of Crystal Growth* **2017**, *457*, 132-136.
60. Ju, M.-G.; Wang, X.; Liang, W.; Zhao, Y.; Li, C., Tuning the energy band-gap of crystalline gallium oxide to enhance photocatalytic water splitting: mixed-phase junctions. *Journal of Materials Chemistry A* **2014**, *2* (40), 17005-17014.
61. He, H.; Orlando, R.; Blanco, M. A.; Pandey, R.; Amzallag, E.; Baraille, I.; Rérat, M., First-principles study of the structural, electronic, and optical properties of Ga₂O₃ in its monoclinic and hexagonal phases. *Physical Review B* **2006**, *74* (19), 195123.
62. Krishnamoorthy, S.; Xia, Z.; Bajaj, S.; Brenner, M.; Rajan, S., Delta-doped β -gallium oxide field-effect transistor. *Applied Physics Express* **2017**, *10* (5), 051102.
63. Åhman, J.; Svensson, G.; Albertsson, J., A reinvestigation of β -gallium oxide. *Acta Crystallographica Section C: Crystal Structure Communications* **1996**, *52* (6), 1336-1338.
64. Yan-Mei, M.; Hai-Yong, C.; Kai-Feng, Y.; Min, L.; Qi-Liang, C.; Jing, L.; Guang-Tian, Z., High-pressure and high-temperature behaviour of gallium oxide. *Chinese Physics Letters* **2008**, *25* (5), 1603.
65. Fleischer, M.; Hanrieder, W.; Meixner, H., Stability of semiconducting gallium oxide thin films. *Thin Solid Films* **1990**, *190* (1), 93-102.
66. Areán, C. O.; Bellan, A. L.; Mentrut, M. P.; Delgado, M. R.; Palomino, G. T., Preparation and characterization of mesoporous γ -Ga₂O₃. *Microporous and mesoporous materials* **2000**, *40* (1-3), 35-42.
67. Zinkevich, M.; Morales, F. M.; Nitsche, H.; Ahrens, M.; Rühle, M.; Aldinger, F., Microstructural and thermodynamic study of γ -Ga₂O₃. *Zeitschrift für Metallkunde* **2004**, *95* (9), 756-762.
68. Roy, R.; Hill, V.; Osborn, E., Polymorphism of Ga₂O₃ and the system Ga₂O₃—H₂O. *Journal of the American Chemical Society* **1952**, *74* (3), 719-722.
69. Playford, H. Y.; Hannon, A. C.; Barney, E. R.; Walton, R. I., Structures of uncharacterised polymorphs of gallium oxide from total neutron diffraction. *Chemistry—A European Journal* **2013**, *19* (8), 2803-2813.

70. Yoshioka, S.; Hayashi, H.; Kuwabara, A.; Oba, F.; Matsunaga, K.; Tanaka, I., Structures and energetics of Ga₂O₃ polymorphs. *Journal of Physics: Condensed Matter* **2007**, *19* (34), 346211.
71. Cótica, L. F.; Santos, G. M.; Freitas, V. F.; Coelho, A. A.; Pal, M.; Santos, I. A.; Garcia, D.; Eiras, J. A.; Guo, R.; Bhalla, A. S., Room temperature nonlinear magnetoelectric effect in lead-free and Nb-doped AlFeO₃ compositions. *Journal of Applied Physics* **2015**, *117* (6), 064104.
72. Liu, H.; Chi, D., Magnetron-sputter deposition of Fe₃S₄ thin films and their conversion into pyrite (FeS₂) by thermal sulfurization for photovoltaic applications. *Journal of Vacuum Science & Technology A: Vacuum, Surfaces, and Films* **2012**, *30* (4), 04D102.
73. Rubio, E.; Atuchin, V.; Kruchinin, V.; Pokrovsky, L.; Prosvirin, I.; Ramana, C., Electronic structure and optical quality of nanocrystalline Y₂O₃ film surfaces and interfaces on silicon. *The Journal of Physical Chemistry C* **2014**, *118* (25), 13644-13651.
74. Kruchinin, V. N.; Perevalov, T.; Atuchin, V. V.; Gritsenko, V.; Komonov, A.; Korolkov, I.; Pokrovsky, L. D.; Shih, C. W.; Chin, A., Optical properties of TiO₂ films deposited by reactive electron beam sputtering. *Journal of Electronic Materials* **2017**, *46* (10), 6089-6095.
75. Kawaharamura, T.; Dang, G. T.; Furuta, M., Successful growth of conductive highly crystalline Sn-doped α-Ga₂O₃ thin films by fine-channel mist chemical vapor deposition. *Japanese Journal of Applied Physics* **2012**, *51* (4R), 040207.
76. Wang, X.; Shen, S.; Jin, S.; Yang, J.; Li, M.; Wang, X.; Han, H.; Li, C., Effects of Zn²⁺ and Pb²⁺ dopants on the activity of Ga₂O₃-based photocatalysts for water splitting. *Physical Chemistry Chemical Physics* **2013**, *15* (44), 19380-19386.
77. Castillo, J.; Garcia-Perez, R.; Huq, H., Optimized Growth of Gallium Oxide Thin Films Using Different Synthesis Processes. *Journal of Electronic Materials* **2019**, *48* (1), 536-541.
78. Isai, M.; Kayano, S.; Horiuchi, T., Preparation of Ga₂O₃ films and evaluation of oxygen sensing properties. *Transactions of the Materials Research Society of Japan* **2010**, *35* (4), 897-900.
79. Kudou, J.; Funasaki, S.; Takahara, M.; Tsunoda, I.; Takakura, K.; Ohyama, H.; Nakashima, T.; Shibuya, M.; Murakami, K.; Simoen, E. In *XRD Investigation of the Crystalline Quality of Sn Doped β-Ga₂O₃ Films Deposited by the RF Magnetron Sputtering Method*, Materials Science Forum, Trans Tech Publ: 2012; pp 269-272.
80. Harwig, T.; Kellendonk, F., Some observations on the photoluminescence of doped β-galliumsesequioxide. *Journal of Solid State Chemistry* **1978**, *24* (3-4), 255-263.
81. Villora, E. G.; Yamaga, M.; Inoue, T.; Yabasi, S.; Masui, Y.; Sugawara, T.; Fukuda, T., Optical spectroscopy study on β-Ga₂O₃. *Japanese journal of applied physics* **2002**, *41* (6A), L622.
82. Sun, R.; Wang, G.-G.; Zhang, H.-Y.; Han, J.-C.; Wang, X.-Z.; Cui, L.; Kuang, X.-P.; Zhu, C.; Jin, L., Microstructure, surface morphology and optical properties of N-incorporated Ga₂O₃ thin films on sapphire substrates. *Journal of alloys and compounds* **2013**, *580*, 517-521.
83. Marie, P.; Portier, X.; Cardin, J., Growth and characterization of gallium oxide thin films by radiofrequency magnetron sputtering. *physica status solidi (a)* **2008**, *205* (8), 1943-1946.
84. Dong, L.; Jia, R.; Xin, B.; Zhang, Y., Effects of post-annealing temperature and oxygen concentration during sputtering on the structural and optical properties of β-Ga₂O₃ films. *Journal of Vacuum Science & Technology A: Vacuum, Surfaces, and Films* **2016**, *34* (6), 060602.
85. Ramana, C.; Rubio, E.; Barraza, C.; Miranda Gallardo, A.; McPeak, S.; Kotru, S.; Grant, J., Chemical bonding, optical constants, and electrical resistivity of sputter-deposited gallium oxide thin films. *Journal of Applied Physics* **2014**, *115* (4), 043508.

86. Fortunato, E.; Raniero, L.; Silva, L.; Goncalves, A.; Pimentel, A.; Barquinha, P.; Aguas, H.; Pereira, L.; Goncalves, G.; Ferreira, I., Highly stable transparent and conducting gallium-doped zinc oxide thin films for photovoltaic applications. *Solar Energy Materials and Solar Cells* **2008**, *92* (12), 1605-1610.
87. Sun, R.; Zhang, H.-Y.; Wang, G.-G.; Han, J.-C.; Wang, X.-Z.; Cui, L.; Kuang, X.-P.; Zhu, C.; Jin, L., Effect of thickness on the microstructure, surface morphology and optical properties of N-incorporated β -Ga₂O₃ films. *Superlattices and Microstructures* **2014**, *65*, 146-151.
88. Battu, A.; Manandhar, S.; Ramana, C., Nanomechanical characterization of titanium incorporated gallium oxide nanocrystalline thin films. *Materials Today Nano* **2018**, *2*, 7-14.
89. Guo, D.; Wu, Z.; An, Y.; Guo, X.; Chu, X.; Sun, C.; Li, L.; Li, P.; Tang, W., Oxygen vacancy tuned Ohmic-Schottky conversion for enhanced performance in β -Ga₂O₃ solar-blind ultraviolet photodetectors. *Applied Physics Letters* **2014**, *105* (2), 023507.
90. Ogita, M.; Saika, N.; Nakanishi, Y.; Hatanaka, Y., Ga₂O₃ thin films for high-temperature gas sensors. *Applied surface science* **1999**, *142* (1-4), 188-191.
91. Battiston, G.; Gerbasi, R.; Porchia, M.; Bertinello, R.; Caccavale, F., Chemical vapour deposition and characterization of gallium oxide thin films. *Thin Solid Films* **1996**, *279* (1-2), 115-118.
92. Shan, F.; Liu, G.; Lee, W.; Lee, G.; Kim, I.; Shin, B., Structural, electrical, and optical properties of transparent gallium oxide thin films grown by plasma-enhanced atomic layer deposition. *Journal of applied physics* **2005**, *98* (2), 023504.
93. Fleischer, M.; Meixner, H., Sensing reducing gases at high temperatures using long-term stable Ga₂O₃ thin films. *Sensors and Actuators B: Chemical* **1992**, *6* (1-3), 257-261.
94. Afzal, A., β -Ga₂O₃ nanowires and thin films for metal oxide semiconductor gas sensors: Sensing mechanisms and performance enhancement strategies. *Journal of Materiomics* **2019**.
95. Frank, J.; Fleischer, M.; Meixner, H., Electrical doping of gas-sensitive, semiconducting Ga₂O₃ thin films. *Sensors and Actuators B: Chemical* **1996**, *34* (1-3), 373-377.
96. Bandi, M.; Zade, V.; Roy, S.; Nair, A. N.; Seacat, S.; Sreenivasan, S.; Shutthanandan, V.; Van de Walle, C. G.; Peelaers, H.; Ramana, C., Effect of Ti Induced Chemical Inhomogeneity on Crystal Structure, Electronic Structure and Optical Properties of Wide Band Gap Ga₂O₃. *Crystal Growth & Design* **2020**.
97. Sigaev, V.; Golubev, N.; Ignat'eva, E.; Savinkov, V.; Campione, M.; Lorenzi, R.; Meinardi, F.; Paleari, A., Nickel-assisted growth and selective doping of spinel-like gallium oxide nanocrystals in germano-silicate glasses for infrared broadband light emission. *Nanotechnology* **2011**, *23* (1), 015708.
98. Li, W.; Peng, Y.; Wang, C.; Zhao, X.; Zhi, Y.; Yan, H.; Li, L.; Li, P.; Yang, H.; Wu, Z., Structural, optical and photoluminescence properties of Pr-doped β -Ga₂O₃ thin films. *Journal of Alloys and Compounds* **2017**, *697*, 388-391.
99. Koenig, H.; Maissel, L., Application of RF discharges to sputtering. *IBM Journal of research and development* **1970**, *14* (2), 168-171.
100. Tsui, T.; Oliver, W.; Pharr, G., Influences of stress on the measurement of mechanical properties using nanoindentation: Part I. Experimental studies in an aluminum alloy. *Journal of Materials Research* **1996**, *11* (3), 752-759.
101. Oliver, W. C.; Pharr, G. M., Measurement of hardness and elastic modulus by instrumented indentation: Advances in understanding and refinements to methodology. *Journal of materials research* **2004**, *19* (1), 3-20.

102. Xu, Z.; Dai, J.; Niu, J.; Li, N.; Huang, G.; He, L., Thermal shock behavior of platinum aluminide bond coat/electron beam-physical vapor deposited thermal barrier coatings. *Journal of alloys and compounds* **2014**, *617*, 185-191.
103. Li, W.; Ming-hui, D.; Hong-sen, Z.; Bin, Z., Study on HfC_xN_{1-x} coatings deposited on biomedical AISI 316L by radio-frequency magnetron sputtering. *Journal of Alloys and Compounds* **2018**, *730*, 219-227.
104. Leyland, A.; Matthews, A., On the significance of the H/E ratio in wear control: a nanocomposite coating approach to optimised tribological behaviour. *Wear* **2000**, *246* (1-2), 1-11.
105. Huang, L.-y.; Lu, J.; Troyon, M., Nanomechanical properties of nanostructured titanium prepared by SMAT. *Surface and Coatings Technology* **2006**, *201* (1-2), 208-213.
106. Tjong, S.; Chen, H., Nanocrystalline materials and coatings. *Materials Science and Engineering: R: Reports* **2004**, *45* (1-2), 1-88.
107. Makeswaran, N.; Battu, A. K.; Deemer, E.; Ramana, C., Crystal Growth and Structure-Property Optimization of Thermally Annealed Nanocrystalline Ga₂O₃ Films. *Crystal Growth & Design* **2020**.
108. Beake, B.; Vishnyakov, V.; Valizadeh, R.; Colligon, J., Influence of mechanical properties on the nanoscratch behaviour of hard nanocomposite TiN/Si₃N₄ coatings on Si. *Journal of Physics D: Applied Physics* **2006**, *39* (7), 1392.
109. Kolsky, H., An investigation of the mechanical properties of materials at very high rates of loading. *Proceedings of the physical society. Section B* **1949**, *62* (11), 676.
110. Nix, W. D., Mechanical properties of thin films. *Metallurgical transactions A* **1989**, *20* (11), 2217.
111. Lim, Y. Y.; Chaudhri, M. M., The effect of the indenter load on the nanohardness of ductile metals: an experimental study on polycrystalline work-hardened and annealed oxygen-free copper. *Philosophical Magazine A* **1999**, *79* (12), 2979-3000.
112. Krell, A., A new look at the influences of load, grain size and grain boundaries on the room temperature hardness of ceramics. *International Journal of refractory Metals and Hard materials* **1998**, *16* (4-6), 331-335.
113. Carey, B. J.; Ou, J. Z.; Clark, R. M.; Berean, K. J.; Zavabeti, A.; Chesman, A. S.; Russo, S. P.; Lau, D. W.; Xu, Z.-Q.; Bao, Q., Wafer-scale two-dimensional semiconductors from printed oxide skin of liquid metals. *Nature communications* **2017**, *8* (1), 1-10.
114. Battu, A. K.; Ramana, C. V., Mechanical Properties of Nanocrystalline and Amorphous Gallium Oxide Thin Films. *Advanced Engineering Materials* **2018**, *20* (11), 1701033.
115. Ramana, C.; Atuchin, V.; Pokrovsky, L.; Becker, U.; Julien, C., Structure and chemical properties of molybdenum oxide thin films. *Journal of Vacuum Science & Technology A: Vacuum, Surfaces, and Films* **2007**, *25* (4), 1166-1171.
116. Ramana, C.; Mudavakkat, V.; Bharathi, K. K.; Atuchin, V.; Pokrovsky, L.; Kruchinin, V., Enhanced optical constants of nanocrystalline yttrium oxide thin films. *Applied Physics Letters* **2011**, *98* (3), 031905.
117. Kalygina, V.; Egorova, I.; Prudaev, I.; Tolbanov, O.; Atuchin, V., Conduction mechanism of metal-TiO₂-Si structures. *Chinese Journal of Physics* **2017**, *55* (1), 59-63.
118. Atuchin, V.; Kruchinin, V.; Wong, Y. H.; Cheong, K. Y., Microstructural and optical properties of ZrON/Si thin films. *Materials Letters* **2013**, *105*, 72-75.
119. Gong, J.; Lipomi, D. J.; Deng, J.; Nie, Z.; Chen, X.; Randall, N. X.; Nair, R.; Whitesides, G. M., Micro- and nanopatterning of inorganic and polymeric substrates by indentation lithography. *Nano letters* **2010**, *10* (7), 2702-2708.

120. Battu, A. K.; Manandhar, S.; Ramana, C. V., Molybdenum incorporation induced enhancement in the mechanical properties of gallium oxide films. *Advanced Materials Interfaces* **2017**, *4* (19), 1700378.
121. Somekawa, H.; Nieh, T.; Higashi, K., Instrumented indentation properties of electrodeposited Ni–W alloys with different microstructures. *Scripta materialia* **2004**, *50* (11), 1361-1365.
122. Ivasishin, O.; Markovsky, P.; Matviychuk, Y. V.; Semiatin, S.; Ward, C.; Fox, S., A comparative study of the mechanical properties of high-strength β -titanium alloys. *Journal of alloys and compounds* **2008**, *457* (1-2), 296-309.
123. Kuzumaki, T.; Ujiie, O.; Ichinose, H.; Ito, K., Mechanical characteristics and preparation of carbon nanotube fiber-reinforced Ti composite. *Advanced Engineering Materials* **2000**, *2* (7), 416-418.
124. Rosenkranz, A.; Reinert, L.; Gachot, C.; Aboufadi, H.; Grandthyll, S.; Jacobs, K.; Müller, F.; Mücklich, F., Oxide formation, morphology, and nanohardness of laser-patterned steel surfaces. *Advanced Engineering Materials* **2015**, *17* (8), 1234-1242.
125. Ramana, C.; Battu, A. K.; Dubey, P.; Lopez, G. A., Phase-Control-Enabled Enhancement in Hydrophilicity and Mechanical Toughness in Nanocrystalline Tungsten Oxide Films for Energy-Related Applications. *ACS Applied Nano Materials* **2020**, *3* (4), 3264-3274.
126. Johnson, P. M.; Stafford, C. M., Effect of interfacial adhesion on viscoelastic relaxation processes in thin polymer film indentation. *ACS Applied Materials & Interfaces* **2010**, *2* (7), 2108-2115.
127. Lee, D.; Rahman, M. M.; Zhou, Y.; Ryu, S., Three-dimensional confocal microscopy indentation method for hydrogel elasticity measurement. *Langmuir* **2015**, *31* (35), 9684-9693.
128. Zhao, J.; Lemoine, P.; Liu, Z.; Quinn, J.; Maguire, P.; McLaughlin, J., A study of microstructure and nanomechanical properties of silicon incorporated DLC films deposited on silicon substrates. *Diamond and related materials* **2001**, *10* (3-7), 1070-1075.
129. Pellicer, E.; Varea, A.; Pané, S.; Nelson, B. J.; Menéndez, E.; Estrader, M.; Surinach, S.; Baró, M. D.; Nogués, J.; Sort, J., Nanocrystalline electroplated Cu–Ni: metallic thin films with enhanced mechanical properties and tunable magnetic behavior. *Advanced Functional Materials* **2010**, *20* (6), 983-991.
130. Musil, J.; Kunc, F.; Zeman, H.; Polakova, H., Relationships between hardness, Young's modulus and elastic recovery in hard nanocomposite coatings. *Surface and Coatings Technology* **2002**, *154* (2-3), 304-313.
131. Lasalmonie, A.; Strudel, J., Influence of grain size on the mechanical behaviour of some high strength materials. *Journal of Materials Science* **1986**, *21* (6), 1837-1852.
132. Leyland, A.; Matthews, A., Design criteria for wear-resistant nanostructured and glassy-metal coatings. *Surface and Coatings Technology* **2004**, *177*, 317-324.
133. Sherman, D.; Brandon, D., Mechanical properties of hard materials and their relation to microstructure. *Advanced Engineering Materials* **1999**, *1* (3-4), 161-181.
134. Korsunsky, A.; McGurk, M.; Bull, S.; Page, T., On the hardness of coated systems. *Surface and Coatings Technology* **1998**, *99* (1), 171-182.
135. Mayo, M.; Nix, W., A micro-indentation study of superplasticity in Pb, Sn, and Sn-38 wt% Pb. *Acta Metallurgica* **1988**, *36* (8), 2183-2192.
136. Peykov, D.; Martin, E.; Chromik, R. R.; Gauvin, R.; Trudeau, M., Evaluation of strain rate sensitivity by constant load nanoindentation. *Journal of Materials Science* **2012**, *47* (20), 7189-7200.

137. Chen, J.; Lu, L.; Lu, K., Hardness and strain rate sensitivity of nanocrystalline Cu. *Scripta Materialia* **2006**, *54* (11), 1913-1918.
138. Maier, V.; Durst, K.; Mueller, J.; Backes, B.; Höppel, H. W.; Göken, M., Nanoindentation strain-rate jump tests for determining the local strain-rate sensitivity in nanocrystalline Ni and ultrafine-grained Al. *Journal of materials research* **2011**, *26* (11), 1421-1430.
139. Alkorta, J.; Martínez-Esnaola, J. M.; Sevillano, J. G., Critical examination of strain-rate sensitivity measurement by nanoindentation methods: Application to severely deformed niobium. *Acta Materialia* **2008**, *56* (4), 884-893.
140. Oh, U.; Je, J. H., Effects of strain energy on the preferred orientation of TiN thin films. *Journal of Applied Physics* **1993**, *74* (3), 1692-1696.
141. Desai, J. A.; Kumar, A., Effect of iron alloying in evolution of nanostructure and microstructural stability in nickel. *Metals and Materials International* **2016**, *22* (3), 451-458.
142. Vehoff, H.; Lemaire, D.; Schüller, K.; Waschkies, T.; Yang, B., The effect of grain size on strain rate sensitivity and activation volume—from nano to ufg nickel. *International journal of materials research* **2007**, *98* (4), 259-268.
143. Bull, S., Failure mode maps in the thin film scratch adhesion test. *Tribology international* **1997**, *30* (7), 491-498.
144. Sojoudi, H.; Walsh, M. R.; Gleason, K. K.; McKinley, G. H., Designing Durable Vapor-Deposited Surfaces for Reduced Hydrate Adhesion. *Advanced Materials Interfaces* **2015**, *2* (6), 1500003.
145. Wirasate, S.; Boerio, F., Effect of adhesion, film thickness, and substrate hardness on the scratch behavior of poly (carbonate) films. *Journal of Adhesion* **2005**, *81* (5), 509-528.
146. Geller, S., Crystal structure of β -Ga₂O₃. *The Journal of Chemical Physics* **1960**, *33* (3), 676-684.
147. Dubey, P.; Lopez, G.; Martinez, G.; Ramana, C., Enhanced mechanical properties of W_{1-y}MoyO₃ nanocomposite thin films. *Journal of Applied Physics* **2016**, *120* (24), 245103.
148. Choi, J.-G.; Thompson, L., XPS study of as-prepared and reduced molybdenum oxides. *Applied Surface Science* **1996**, *93* (2), 143-149.
149. Ramana, C. V.; Atuchin, V. V.; Kesler, V.; Kochubey, V.; Pokrovsky, L.; Shutthanandan, V.; Becker, U.; Ewing, R. C., Growth and surface characterization of sputter-deposited molybdenum oxide thin films. *Applied surface science* **2007**, *253* (12), 5368-5374.
150. Bhachu, D. S.; Scanlon, D. O.; Sankar, G.; Veal, T.; Egdell, R. G.; Cibin, G.; Dent, A. J.; Knapp, C. E.; Carmalt, C. J.; Parkin, I. P., Origin of high mobility in molybdenum-doped indium oxide. *Chemistry of Materials* **2015**, *27* (8), 2788-2796.
151. Silipigni, L.; Barreca, F.; Fazio, E.; Neri, F.; Spano, T.; Piazza, S.; Sunseri, C.; Inguanta, R., Template electrochemical growth and properties of Mo oxide nanostructures. *The Journal of Physical Chemistry C* **2014**, *118* (38), 22299-22308.
152. Kan, Q.; Yan, W.; Kang, G.; Sun, Q., Oliver–Pharr indentation method in determining elastic moduli of shape memory alloys—a phase transformable material. *Journal of the Mechanics and Physics of Solids* **2013**, *61* (10), 2015-2033.
153. Alexopoulos, P.; O'sullivan, T., Mechanical properties of thin films. *Annual review of materials science* **1990**, *20* (1), 391-420.
154. Jamison, R. D.; Shen, Y.-L., Indentation and overall compression behavior of multilayered thin-film composites: Effect of undulating layer geometry. *Journal of Composite Materials* **2016**, *50* (4), 507-521.

155. Wang, X.; Shen, X.; Sun, F.; Shen, B., Influence of boron doping level on the basic mechanical properties and erosion behavior of boron-doped micro-crystalline diamond (BDMCD) film. *Diamond and Related Materials* **2017**, *73*, 218-231.
156. Coddet, P.; Sanchette, F.; Rousset, J.; Rapaud, O.; Coddet, C., On the elastic modulus and hardness of co-sputtered Zr–Cu–(N) thin metal glass films. *Surface and Coatings Technology* **2012**, *206* (17), 3567-3571.
157. Chou, T.; Nieh, T., Pest disintegration of thin MoSi₂ films by oxidation at 500° C. *Journal of materials science* **1994**, *29* (11), 2963-2967.
158. Xing, L.; Eckert, J.; Schultz, L., Deformation mechanism of amorphous and partially crystallized alloys. *NanoStructured materials* **1999**, *12* (1-4), 503-506.
159. Tietz, T. E.; Wilson, J. W., Behavior and properties of refractory metals. **1965**.
160. Bao, Y.; Wang, W.; Zhou, Y., Investigation of the relationship between elastic modulus and hardness based on depth-sensing indentation measurements. *Acta Materialia* **2004**, *52* (18), 5397-5404.
161. Bucaille, J.; Felder, E.; Hochstetter, G., Mechanical analysis of the scratch test on elastic and perfectly plastic materials with the three-dimensional finite element modeling. *Wear* **2001**, *249* (5-6), 422-432.
162. Ichimura, H.; Rodrigo, A., The correlation of scratch adhesion with composite hardness for TiN coatings. *Surface and Coatings Technology* **2000**, *126* (2-3), 152-158.
163. Dubey, P.; Battu, A. K.; Shutthanandan, V.; Ramana, C., Effect of Interface Structure on the Hydrophobicity, Mechanical and Optical Properties of HfO₂/Mo/HfO₂ Multilayer Films. *JOM* **2019**, *71* (10), 3711-3719.
164. Manandhar, S.; Battu, A. K.; Tan, S.; Panat, R.; Shutthanandan, V.; Ramana, C., Effect of Ti doping on the crystallography, phase, surface/interface structure and optical band gap of Ga₂O₃ thin films. *Journal of Materials Science* **2019**, *54* (17), 11526-11537.
165. Manandhar, S.; Battu, A. K.; Orozco, C.; Ramana, C., Optical constants of titanium-doped gallium oxide thin films. *Optical Materials* **2019**, *96*, 109223.
166. Rebien, M.; Henrion, W.; Hong, M.; Mannaerts, J.; Fleischer, M., Optical properties of gallium oxide thin films. *Applied physics letters* **2002**, *81* (2), 250-252.
167. Yamaga, M.; Villora, E. G.; Shimamura, K.; Ichinose, N.; Honda, M., Donor structure and electric transport mechanism in β–Ga₂O₃. *Physical Review B* **2003**, *68* (15), 155207.
168. Atuchin, V.; Gavrilova, T.; Grigorieva, T.; Kuratieva, N.; Okotrub, K.; Pervukhina, N.; Surovtsev, N., Sublimation growth and vibrational microspectrometry of α-MoO₃ single crystals. *Journal of crystal growth* **2011**, *318* (1), 987-990.
169. Parise, J.; McCarron III, E.; Von Dreele, R.; Goldstone, J., β-MoO₃ produced from a novel freeze drying route. *Journal of Solid State Chemistry* **1991**, *93* (1), 193-201.
170. Makeswaran, N.; Battu, A. K.; Swadipta, R.; Manciu, F. S.; Ramana, C., Spectroscopic Characterization of the Electronic Structure, Chemical Bonding, and Band Gap in Thermally Annealed Polycrystalline Ga₂O₃ Thin Films. *ECS Journal of Solid State Science and Technology* **2019**, *8* (7), Q3249-Q3253.
171. Shannon, R. D., Revised effective ionic radii and systematic studies of interatomic distances in halides and chalcogenides. *Acta crystallographica section A: crystal physics, diffraction, theoretical and general crystallography* **1976**, *32* (5), 751-767.
172. Battu, A. K.; Manandhar, S.; Shutthanandan, V.; Ramana, C., Controlled optical properties via chemical composition tuning in molybdenum-incorporated β-Ga₂O₃ nanocrystalline films. *Chemical Physics Letters* **2017**, *684*, 363-367.

173. Illyaskutty, N.; Kohler, H.; Trautmann, T.; Schwotzer, M.; Pillai, V. M., Enhanced ethanol sensing response from nanostructured MoO₃: ZnO thin films and their mechanism of sensing. *Journal of Materials Chemistry C* **2013**, *1* (25), 3976-3984.
174. Berry, T.; Fu, C.; Auffermann, G.; Fecher, G. H.; Schnelle, W.; Serrano-Sanchez, F.; Yue, Y.; Liang, H.; Felser, C., Enhancing thermoelectric performance of TiNiSn half-Heusler compounds via modulation doping. *Chemistry of Materials* **2017**, *29* (16), 7042-7048.
175. Rafique, S.; Han, L.; Neal, A. T.; Mou, S.; Boeckl, J.; Zhao, H., Towards High-Mobility Heteroepitaxial β -Ga₂O₃ on Sapphire— Dependence on The Substrate Off-Axis Angle. *physica status solidi (a)* **2018**, *215* (2), 1700467.
176. Serrao, F.; Dharmaprakash, S., Structural, optical and electrical properties of sol-gel prepared Ga: ZnO thin film. *Materials Research Innovations* **2016**, *20* (6), 470-474.
177. Feng, Z.; Anhar Uddin Bhuiyan, A.; Karim, M. R.; Zhao, H., MOCVD homoepitaxy of Si-doped (010) β -Ga₂O₃ thin films with superior transport properties. *Applied Physics Letters* **2019**, *114* (25), 250601.
178. Battu, A. K.; Makeswaran, N.; Ramana, C., Fabrication, characterization and optimization of high conductivity and high quality nanocrystalline molybdenum thin films. *Journal of Materials Science & Technology* **2019**, *35* (11), 2734-2741.
179. Chikoidze, E.; Sartel, C.; Mohamed, H.; Madaci, I.; Tchelidze, T.; Modreanu, M.; Vales-Castro, P.; Rubio, C.; Arnold, C.; Sallet, V., Enhancing the intrinsic p-type conductivity of the ultra-wide bandgap Ga₂O₃ semiconductor. *Journal of Materials Chemistry C* **2019**, *7* (33), 10231-10239.
180. Lee, H. Y.; Yang, I. J.; Yoon, J.-H.; Jin, S.-H.; Kim, S.; Song, P. K., Thermoelectric Properties of Zinc-Doped Indium Tin Oxide Thin Films Prepared Using the Magnetron Co-Sputtering Method. *Coatings* **2019**, *9* (12), 788.
181. Kalidindi, N.; Manciu, F.; Ramana, C., Crystal structure, phase, and electrical conductivity of nanocrystalline W_{0.95}Ti_{0.05}O₃ thin films. *ACS applied materials & interfaces* **2011**, *3* (3), 863-868.
182. Fleischer, M.; Meixner, H., Oxygen sensing with long-term stable Ga₂O₃ thin films. *Sensors and Actuators B: Chemical* **1991**, *5* (1-4), 115-119.
183. Moseley, P., Materials selection for semiconductor gas sensors. *Sensors and Actuators B: Chemical* **1992**, *6* (1-3), 149-156.

Vita

Anil Krishna Battu was born in 1990, in India. In April 2008 Mr. Anil Krishna Battu received a Diploma in Mechanical Engineering from Polytechnic college, immediately after that, he enrolled in the undergraduate program, Bachelor of Technology in Mechanical Engineering from Vijay Rural Engineering College (VREC) affiliated by JNTU-Kukatpally. Mr. Battu then worked as a Graduate Apprentice in Indian Space Research Organization (ISRO). To pursue higher education, Mr. Battu enrolled in the Master of Technology at P.V.P. Siddhartha Institute of Technology (autonomous) affiliated by JNTU-Kakinada in December 2015. He did work as a Graduate Student Intern at the International Advanced Research Centre for Powder Metallurgy and New Materials (ARCI). Mr. Battu started his Ph.D. in the University of Texas at El Paso in Fall 2016 in the Department of Mechanical Engineering. He did as Ph.D. Research Intern at Pacific Northwest National Laboratory from Fall 2018 to Spring 2020. He has several first-author publications in various innovative scientific journals.

Contact Information (optional) : anilkrishna.battu@gmail.com

This thesis/dissertation was typed by Anil Krishna Battu